

FLORIDA STATE UNIVERSITY
COLLEGE OF ARTS & SCIENCES

LARGE EDDY SIMULATIONS TO INVESTIGATE THE FUNDAMENTAL FLOW PHYSICS
OF SUPERCRITICAL CARBON DIOXIDE TURBULENT JETS

By

JULIA REAM

A Dissertation submitted to the
Department of Mathematics
in partial fulfillment of the
requirements for the degree of
Doctor of Philosophy

2023

Julia Ream defended this dissertation on July 11, 2023.

The members of the supervisory committee were:

Mark Sussman
Professor Co-Directing Dissertation

Marc Henry de Frahan
Professor Co-Directing Dissertation

Bryan Quaife
University Representative

Aseel Farhat
Committee Member

Sanghyun Lee
Committee Member

The Graduate School has verified and approved the above-named committee members, and certifies that the dissertation has been approved in accordance with university requirements.

*All hail, Macbeth! hail to thee, thane of Glamis!
All hail, Macbeth, hail to thee, thane of Cawdor!
All hail, Macbeth, thou shalt be king hereafter!*

Macbeth, *Act I, Scene III*

ACKNOWLEDGMENTS

I would like to first extend a hearty thanks my wonderful co-advisers, Dr. Mark Sussman and Dr. Marc Henry de Frahan. Dr. Sussman has given me an abundance of knowledge and memorable anecdotes in my eight years of learning from him, which I will cherish forever. He was the first person to suggest I apply to PhD programs when I initially started thinking about going to graduate school, so I really would not be here without his encouragement and support. I will also be forever grateful to Marc for all of the time, energy, guidance, knowledge, and advice that he has given me over these past four years. One day, I hope to be as good of a mentor to someone as he has been to me. I would also like to extend my deepest appreciation to my committee members: Dr. Aseel Farhat, Dr. Sanghyun Lee, and Dr. Bryan Quaife. Their feedback throughout this process has been invaluable.

There are many people that have had a significant impact on my life who I met from the internships and graduate assistantships that I've held during my time at FSU. Many thanks to Michael Martin, Shashank Yellapantula, Anne Felden, and Marc Day for their mentorship and the collaborations they have fostered well beyond the end of our summers together. Special thanks are due to Dr. Penelope Kirby for being an exemplary leader and for trusting me with so many extraordinary teaching opportunities.

This work would not have been possible without the support of my incredible friends. I am forever indebted to the besties I've made along the way: Virginia for bringing her personal brand of chaos and humor to our day-to-day antics since day one, Angie for always gassing me up and validating my Virgo tendencies, Matt for always giving me custody of our shared brain cell whenever I needed it most, Kyle for keeping my stomach and soul well-fed with our many nights of dinner and a movie, Colton for being the best dad a friend group could ever ask for, Sathya for his wisdom and insights into both math and life in general, and Austin for his trivia contributions and passionate opinions. I also extend my thanks to the plethora of other graduate students who greatly boosted morale over these past six years: Dan, Lydia, Devon, Celine, David, and the extensive members of Waldemar. Of course, many thanks are due to my non-graduate school people as well: Hannah, Lauren, Christina, Cam, and Goose.

Finally, I owe everything to my family. My mom and dad, Maria and Jeff, have motivated me to do my best in school, always, whether it be in studying music, English, math or theatre. I would not be where I am today without their hard work and sacrifice. My brother, Jacob, and my cousins,

Jessica and Bill, have also been in my corner since forever, and I am grateful to have always had them by my side. I was also lucky enough to have gained in-laws during my time in grad school whose love and support is also much appreciated. Though it may be odd, I feel compelled to also extend my gratitude to Tuna; she will never read this because she is a cat, but her contributions toward my mental health during this process cannot go unnoticed. Last, but certainly not least, I extend my deepest gratitude to my husband, Alex. Even at my lowest lows, he believed in me so much that I had no choice but to believe in myself. Words cannot adequately express how grateful I am to have found him within all of this.

This research was supported in part by an appointment with the National Science Foundation (NSF) Mathematical Sciences Graduate Internship (MSGI) Program sponsored by the NSF Division of Mathematical Sciences. This program is administered by the Oak Ridge Institute for Science and Education (ORISE) through an interagency agreement between the U.S. Department of Energy (DOE) and NSF. ORISE is managed for DOE by ORAU. All opinions expressed in this paper are the author's and do not necessarily reflect the policies and views of NSF, ORAU/ORISE, or DOE. The research was performed using computational resources sponsored by the Department of Energy's Office of Energy Efficiency and Renewable Energy and located at the National Renewable Energy Laboratory. This work was supported by the Department of Energy's Office of Science through the Exascale Computing Project (ECP), managed through Oak Ridge National Laboratory.

TABLE OF CONTENTS

List of Tables	ix
List of Figures	x
List of Abbreviations	xiii
Abstract	xiv
1 Introduction	1
1.1 What is a Fluid?	2
1.1.1 Supercritical Fluids	3
1.1.2 Applications of Interest	3
1.2 Mathematics of Fluid Flow	5
1.2.1 Continuum Description of Fluids	6
1.2.2 Equation of State	8
1.3 Turbulence	10
1.3.1 Mathematics of Turbulence	11
1.3.2 Numerical Approaches to Turbulence Modeling	12
1.4 Current Research Landscape	15
1.4.1 Experimental Contributions	15
1.4.2 Numerical Contributions	15
2 Model Overview	18
2.1 Introduction	18
2.2 Governing Equations	18
2.2.1 Filtered Navier-Stokes Equations	19
2.2.2 Subgrid-Scale Modeling for Large Eddy Simulation	21
2.3 Transport Models	23
2.4 Thermodynamics and Related Quantities	24
2.5 Model Validation	25
3 Numerical Methods	28
3.1 Introduction	28
3.2 Finite Volume Formulation	28

3.3	Temporal Discretization: Spectral Deferred Correction Methods	30
3.4	Spatial Discretization: Flux Calculations	31
3.4.1	Piecewise Parabolic Method	32
3.4.2	Approximate Riemann Solver	33
4	Simulations	34
4.1	Computational Domain	34
4.1.1	AMR and Discretization	34
4.1.2	Initial and Boundary Conditions	35
4.2	Case Descriptions	36
4.3	Compute Time and Hardware Specifications	38
4.4	Post-Processing Procedures	38
4.5	Challenges and Lessons Learned	39
4.6	Contributions Made to <i>PelePhysics</i>	42
5	Results	43
5.1	Isothermal Jet	43
5.1.1	Flow Field Features	44
5.1.2	Mean Flow Properties	46
5.1.3	Turbulence Dynamics	50
5.1.4	Discussion	51
5.2	Non-Isothermal Jets	51
5.2.1	Flow Field Features	52
5.2.2	Mean Flow Properties	59
5.2.3	Turbulence Dynamics	65
5.2.4	Discussion	67
6	Conclusion	69
Appendices		
A	Transport Coefficients	71
B	Additional Thermodynamic Quantities	73

C PeleC Input Parameters for Simulations	75
Bibliography	78
Biographical Sketch	90

LIST OF TABLES

2.1	Maximum percent error between NIST WebBook Data and simulation models for constant-pressure specific heat, density, viscosity, and thermal conductivity.	27
4.1	Summary of jet parameters for each case.	37
A.1	Coefficients for EGLib Polynomials [28] used to model transport quantities as described in Equation (2.19)	71
A.2	Quantities used in part for Chung's High Pressure Corrections. Values gathered from EGLib approximations [28]	71
A.3	Linear Coefficients Used in Calculating High Pressure Viscosity Corrections as found by Chung et al. [18]	72
A.4	Linear Coefficients Used in Calculating High Pressure Thermal Conductivity Corrections as found by Chung et al. [18]	72
B.1	Coefficients for NASA polynomials [61] used in modeling ideal thermodynamic quantities as described in Equation (2.31)	73

LIST OF FIGURES

1.1	Phase diagram for Carbon Dioxide (CO ₂). Critical pressure, p_c , and temperature, T_c , are 73.773 bar and 304.128 K, respectively.	4
1.2	Size comparison for steam vs. supercritical Carbon Dioxide (sCO ₂) turbine via Echogen Power Systems LLC [71].	5
1.3	Characteristic length scale of problem, L , compared to mean free path of particles, ℓ , for a flow with large Knudsen number (left) vs. small Knudsen number (right)	6
1.4	A fluid of arbitrary volume V bounded by surface S with velocity $\mathbf{v}(\mathbf{x}, t)$. A differential volume and surface area is given by dv and ds , respectively. \mathbf{n} is the outward-pointing unit normal vector to the surface S	7
1.5	Example of streamlines in laminar (left) vs. turbulent (right) flow.	10
1.6	Depiction of the energy cascade present in turbulence along associated scales. Resolved vs. Modeled scales are mapped for direct numerical simulation (DNS), large eddy simulation (LES), and Reynolds-averaged Navier-Stokes (RANS) [8].	12
1.7	LES resolves large-scale eddies (black) and models the effects of fine-scale eddies (red) that are unresolved due to mesh size.	14
2.1	Here we compare NIST WebBook values [49] with output values from the thermodynamic and transport models described here as implemented in <i>PelePhysics</i> . Challenges of capturing the fluid properties near the critical point can be seen in the increased error near the pseudo-boiling point near 318K.	26
3.1	2D slice of 3D data demonstrating mesh refinement using <i>AMReX</i> . The refinement ratio is 2 and there are 3 levels of mesh refinement.	30
4.1	Two dimensional slice schematic of jet setup. Four levels of refinement are enforced within the green box based on proximity to jet inlet. Refinement based on vorticity criterion then occurs within the blue region. Outside the blue region, adaptive mesh refinement (AMR) is explicitly turned off to allow flow structures to be dissipated numerically and allowed to leave the domain without incurring spurious reflections.	35
4.2	Extreme thermodynamic variation seen near critical point with ambient temperatures plotted for reference to see regime coverage of each case. Red is the jet temperature for all cases and isothermal temperature for the ambient case. Blue is the 350K ambient case. Green is the 314K ambient case.	38
4.3	An example of the yt slicing issue caused by a floating point precision error. The image contains a slice normal to the flow axis depicting the axial velocity component with patches of data missing.	41
5.1	Axial velocity features of the isothermal jet.	45

5.2	Pressure features of the isothermal jet.	45
5.3	Vorticity magnitude features of the isothermal jet.	46
5.4	Average (both in time and radially) axial velocity scaled by inlet value plotted along radial distance from centerline. Profile decay follows similar trajectory to what is expected in incompressible round jet theory [76].	47
5.5	Normal slices of scaled axial velocity, averaged in both time and the radial direction, plotted in the radial direction scaled by $r_{1/2}$. Both near- and far-field regions demonstrate the self-similarity within the round turbulent jet.	48
5.6	Axial inlet velocity scaled by centerline values along the axial direction. When the distance downstream is scaled by the jet diameter, linear decay of the centerline axial velocity is observed.	49
5.7	half-mean half-width (HMHW) of axial velocity along the axial direction. When the distance downstream is scaled by the jet diameter, linear growth of the axial velocity HMHW is observed.	49
5.8	Time and radially averaged Reynolds stresses for the isothermal jet at two locations downstream. Both slices follow similar Reynolds stress relations seen in incompressible round jet [76].	50
5.9	Average resolved turbulent kinetic energy components along centerline. Note: averaging as described in Chapter 4 occurs prior to square rooting in the given quantity description.	51
5.10	Axial velocity field comparison between 314K ambient case (left), 330K ambient case (middle), and 350K ambient case (right).	53
5.11	Pressure fluctuation field comparison between 314K ambient case (left), 330K ambient case (middle), and 350K ambient case (right).	54
5.12	Vorticity magnitude field comparison between 314K ambient case (left), 330K ambient case (middle), and 350K ambient case (right).	56
5.13	Direct comparison between 314K ambient case (left) and 350K ambient case (right) for various fluid quantities of interest.	58
5.14	Average (both in time and radially) axial velocity scaled by inlet value plotted along radial distance from centerline.	59
5.15	Normal slices of scaled near-field and far-field axial velocity profiles, averaged in both time and the radial direction. Plotted against radial direction scaled by $r_{1/2}$	60
5.16	Normal slices of scaled far-field density, averaged in both time and the radial direction, plotted in the radial direction scaled by $r_{1/2}$	61

5.17	Axial inlet velocity scaled by centerline values along the axial direction. When distance downstream is scaled by jet diameter, linear decay of the centerline axial velocity is observed.	62
5.18	HMHW values scaled by jet diameter along the axial direction. When distance downstream is scaled by jet diameter, linear growth of the half-widths is observed.	62
5.19	Comparison of centerline decay for various fluid quantities.	64
5.20	Time and radially averaged Reynolds stresses for the non-isothermal jets at two locations downstream.	65
5.21	Comparison of average turbulent kinetic energy components along centerline for each non-isothermal case.	66
5.22	Cross-case comparisons of average turbulent kinetic energy components and total resolved TKE along centerline.	67
C.1	Input parameters for available physics options in PeleC	76
C.2	AMR tagging criteria selected within in PeleC	77

LIST OF ABBREVIATIONS

The following short list of abbreviations are used throughout this document.

AMR	Adaptive Mesh Refinement
CFD	Computational Fluid Dynamics
CFL	Courant-Friedrichs-Lowy
CO ₂	Carbon Dioxide
DNS	Direct Numerical Simulation
DOE	Department of Energy
ECP	Exascale Computing Project
EoS	equation of state
HMHW	half-mean half-width
HPC	high-performance computing
LES	Large Eddy Simulation
MISDC	Multi-Implicit Spectral Deferred Correction
MOL	Method of Lines
NIST	National Institute of Standards and Technology
NREL	National Renewable Energy Laboratory
ODE	Ordinary Differential Equation
PDE	Partial Differential Equation
PPM	piecewise parabolic method
PR EoS	Peng-Robinson equation of state
QSSA	quasi-steady state assumptions
RANS	Reynolds-Averaged Navier-Stokes
rms	root mean square
SDC	Spectral Deferred Correction
sCO ₂	Supercritical Carbon Dioxide
SGS	Subgrid Scale
SMD	dynamic Smagorinsky
SRK EoS	Soave-Redlich-Kwong equation of state
TKE	Turbulent Kinetic Energy

ABSTRACT

Supercritical Carbon Dioxide is of interest in a wide range of engineering problems, including carbon capture, utilization, and storage as well as advanced cycles for power generation. Non-ideal variations in physical properties of supercritical Carbon Dioxide impact the physics of these systems. It is important to understand how drastic changes in thermodynamic properties influence these flow physics in order to aid in and optimize the design of future technologies related to carbon capture and sequestration. In this study, we simulate turbulent supercritical Carbon Dioxide jets to gain a better understanding of these physics. Of particular interest is the impact of pseudo-boiling on supercritical flow dynamics. We use a second order finite volume method with adaptive mesh refinement as implemented in the reacting flow solver, *PeleC*, to perform a Large Eddy Simulation of three turbulent jets of supercritical Carbon Dioxide. Additionally, we use the Soave-Redlich-Kwong equation of state to close the system and more accurately incorporate the departure from ideal gas behavior into the turbulent flow physics. We look at a variety of quantities of interest, including but not limited to axial velocity decay and spread, resolved Reynolds stress profiles at different downstream locations, and resolved turbulent kinetic energy along the axial direction of the flow. Across the three cases, the only parameters that vary are the temperature and density of the ambient fluid. One case is isothermal, where the jet and ambient fluid temperature are the same, while the other two cases are non-isothermal, with one involving injection crossing over the pseudo-boiling point and one with injection moving away from the pseudo-boiling point. Results are contrasted with established theory for ideal gas jets and similar numerical studies involving transcritical injection in order to capture the effects of widely varying thermal properties in the pseudo-critical region. We found that the isothermal supercritical jet exhibits many similar flow characteristics compared to ideal gas round turbulent jets, with minor differences seen in the decay and spreading rate of the jet and in a noticeable anisotropy between resolved turbulent kinetic energy components. The non-isothermal jet excluding the pseudo-boiling point exhibits only small difference compared to the isothermal case. The non-isothermal case involving the pseudo-boiling point displays markedly different behavior, with evidence indicative of increased Kelvin-Helmholtz-like instabilities and much faster jet decay and disintegration. These factors impact the degree of mixing in the transition region of the jet, leading to finer-scale vortices and faster transition to ambient properties.

CHAPTER 1

INTRODUCTION

Carbon Dioxide (CO₂) is the primary greenhouse gas emitted through human activity [68]. Higher levels of CO₂ in the atmosphere can lead to further heat retention, causing global temperature levels to rise at a record-breaking rate [56]. In an effort to reduce man-made contributions toward issues related to climate change, carbon capture and sequestration has become a prominent area of research [104, 23, 7]. A natural extension of this line of research might then be to ask: what does one do with all of this collected CO₂? Are there industrial or technological applications that can benefit from this available reserve? Luckily, the answer to that question is a resounding “yes”.

The applications used to motivate this research are all concerned with supercritical Carbon Dioxide (sCO₂), in particular. sCO₂ has many beneficial features that are important to a wide variety of industrial applications, as we will detail further later on in this chapter. Many of these applications of interest include injection technologies that involve a round turbulent jet configuration within the system. Much research has gone into supercritical jet turbulence, however, due to extreme thermodynamic variation around the supercritical point (a region known as the pseudo-critical zone), slight changes in parameter regime result in significant changes in flow dynamics [51, 81]. Thus there is much research needed still in order to fully understand the fundamental flow physics within this area of interest.

The goal of this work is to further explore the pseudo-boiling region of the pseudo-critical zone and analyze the influence of extreme thermodynamic fluctuations on turbulence statistics and flow dynamics within the flow field. To that end, the rest of this chapter continues as follows: first, we cover important definitions relating to fluids in order to establish what a supercritical fluid even is. Then, the mathematical framework for modeling compressible Newtonian fluids is provided to form the basis of the modeling done in this dissertation. Further consideration is then given to turbulence modeling and the numerical methods developed for studying turbulence to provide insight into the quantities of interest analyzed within this dissertation and the choices of numerical methods used herein. Important applications of supercritical carbon dioxide in particular are provided to motivate the problem presented in this dissertation. Existing numerical studies on supercritical fluids are reviewed to demonstrate how this dissertation fits into the current landscape of research and to

emphasize the contributions this work make to the field. This chapter concludes with an outline of the dissertation, the goals of the dissertation, and the main contributions made through this work.

1.1 What is a Fluid?

In order to discuss supercritical fluids further, we must first go into more detail about general fluids. Here we go over the general definitions and distinctions given to fluids as outlined by Batchelor [10]. One of the defining characteristics that can be used to distinguish fluids from solids is the ease with which they deform. Generally, a solid material has a definite shape and internal structure, which only changes when acted upon by external forces. Fluids on the other hand do not have a preferred shape. More specifically, elements within a parcel of fluid can experience rearrangement through chaotic motion without affecting the macroscopic nature of the parcel. This continuous and relatively large deformation given a potentially small but suitable external force is one way to distinguish a fluid from a solid, where instead small external force only results in small internal change.

The two categories of fluids that most people are familiar with are gases and liquids. These two states are mainly distinguished by differences in intermolecular scales and forces. Molecules within a gas are, on average, much farther apart than they are in liquids. This separation is so vast in gases, that molecules only experience very weak cohesive forces, except for when the rare collision occurs [10]. Molecules within liquids, on the other hand, are close enough to affect one another through near-field attractive forces at any given time. A simplified distinction between the two is that both gases and liquids will conform to the shape of whatever container they are in, but gases will further spread to fill all available space present.

The state of a fluid can be uniquely determined by two quantities: pressure and density. Pressure is the force per unit area exerted by the fluid on its boundaries [69]. Density is the mass per unit volume of the fluid [69]. These two quantities can be related to other important information, like temperature, which indicates the level of thermal energy in the fluid [69]. In gases, the main contribution to pressure is the force normal to the surface of each individual molecule on the fluid boundary. Reducing the volume of a fixed mass of gas while maintaining a constant temperature will increase the density, thus reducing the average distance between molecules. If, however, this distance remains relatively large compared to the size of the molecule, then intermolecular forces are still negligible and do not significantly contribute to pressure. Fluids that allow for this reduction

are said to be compressible. By contrast, molecules within liquids experience strong cohesive forces due to their close proximity to one another [10]. If density is increased even slightly at constant temperature, the pressure contribution experienced toward one molecule by its neighbors greatly increases, resulting in a large pressure change. Fluids that show a resistance to this volume reduction process are then said to be incompressible. In either case, the relationship between pressure, temperature, and density can be measured and modeled through mathematics, as we will see later on in this chapter.

1.1.1 Supercritical Fluids

A supercritical fluid is a fluid that is held above a critical temperature and pressure, at which point the distinction between a gas and liquid phase no longer exists [29, 92]. Supercritical fluids have qualities associated with both gases and liquids yet simultaneously have features that exclude them from fully being categorized as one or the other. For example, while they have viscosities akin to gases, they have a solvent power associated with liquids [1]. Similarly, while they have densities in line with liquids, they lack surface tension [101]. One benefit of this duality is that supercritical fluids can be fine tuned to be more gas-like or more liquid-like depending on the application at hand. This also results in ambiguity on how to actually classify them, with some sources considering them highly compressed gases [36], expanded liquids [1], or even as their own distinctly separate phase [9]. The distinction usually lies on the specifics of the regime and the application at hand.

We focus on one particular fluid of interest: CO₂. As seen in the phase diagram of Figure 1.1, the critical temperature, T_c , and critical pressure, p_c , of CO₂ are 304.128 K and 73.773 bar. The critical temperature and pressure of CO₂ is fairly easy to attain, making it a strong candidate for systems with high thermal outputs. Additionally, sCO₂ has a relatively low toxicity and environmental impact, and is chemically stable, non-flammable, and readily available [1]. For these reasons, sCO₂ is a highly coveted alternative working fluid in many different applications, and is one of the most widely used supercritical fluids along with water [29].

In the next part of this section, we will explore some applications of sCO₂ where the turbulent round jet configuration is used in order to further motivate the investigation outlined in this work.

1.1.2 Applications of Interest

One of the key applications of interest that motivates this work is the use of sCO₂ as the working fluid in advanced cycles for power generation. sCO₂ has shown promise as a working fluid for both

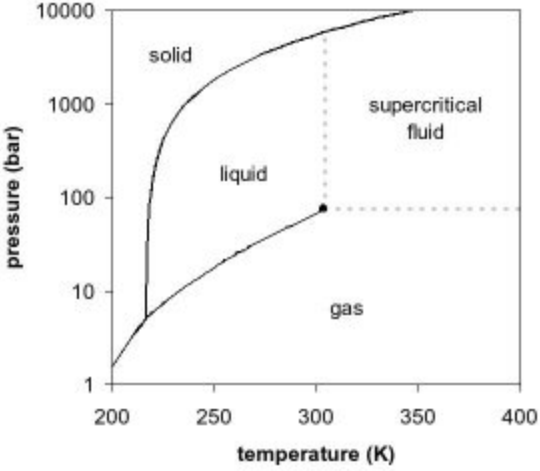


Figure 1.1: Phase diagram for Carbon Dioxide (CO₂). Critical pressure, p_c , and temperature, T_c , are 73.773 bar and 304.128 K, respectively.

indirect cycle and direct-firing cycles [102, 103]. One example of indirect cycle improvement uses sCO₂ in place of water for the conventional steam-Rankine cycle. An example of where these types of configurations may prove useful is in managing thermal runoff from existing coal and natural gas combustion processes [102]. Compared to steam, sCO₂ is less corrosive, more thermally stable, and has increased power density. The critical point of CO₂ is easily accessible, and once achieved, allows for the use of a single phase fluid design, leading to a simplified and more compact turbine (see Figure 1.2). Ultimately, this also allows for lower operation and maintenance costs [24]. The benefits of using sCO₂ turbines over the traditional steam design has been highly researched and has only seen an increase in momentum for implementation [22, 26, 24, 71].

An example of direct-firing cycles that use sCO₂ include the Allam cycle [3]. When compared to the conventional Brayton cycle, studies show that the Allam cycle has much higher efficiency [25, 4]. Additionally, the carbon footprint for the Allam cycle is virtually zero, allowing for CO₂ produced from the system to be stored underground or used elsewhere, aiding in carbon sequestration efforts [32]. This two-for-one benefit of using sCO₂-based cycles such as the Allam cycle has spurred much research [98, 16] and development [83] into related technologies.

Of particular importance to these applications is the round turbulent jet, as this is a major component of many injection technologies. The high densities associated with the liquid-like aspect of supercritical fluids coupled with the relatively low gas-like viscosity associated with them typically

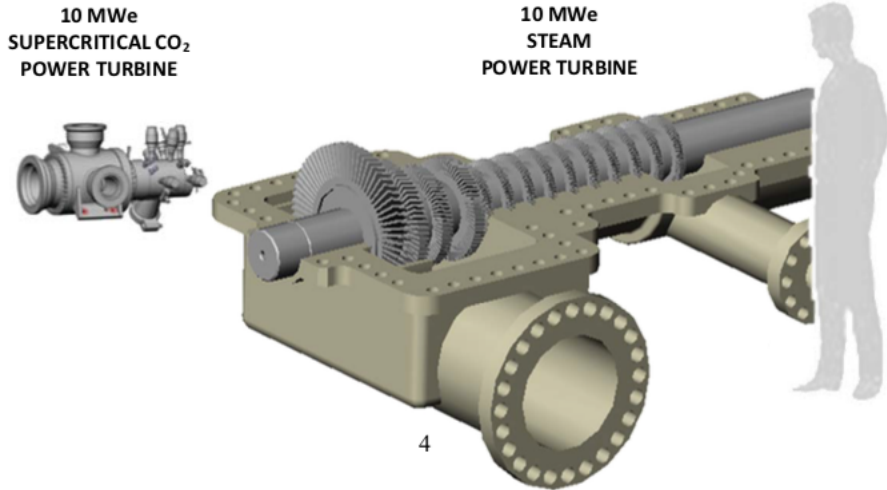


Figure 1.2: Size comparison for steam vs. sCO₂ turbine via Echogen Power Systems LLC [71].

results in a high Reynolds flow, often resulting in a turbulent system. The turbulence physics of these jets is crucial in developing machinery for these systems.

1.2 Mathematics of Fluid Flow

Scale is one of the key factors to consider when developing a mathematical description of a fluid system. For example, consider modeling flow past a satellite in the exosphere vs. the flow past a turtle in the ocean; these two mediums have vastly different characteristics and would thus require different modeling techniques. Scale is also an important concept when it comes to turbulence in particular so we will begin that discussion here with our choice in perspective for the mathematical framework of our system of interest.

From a kinetics perspective, particle motion within a fluid can be broken up into two phases: particle interaction and free flight. Average time spent in free flight, $\langle t_f \rangle$, is typically much greater than collision time for a given interaction, t_c . The average length traveled between collisions is known as the mean free path, ℓ . Since free flight time dominates particle interaction time, this phase determines the length scale of the kinetic description of motion. In addition to this inherent physical scale, there is also a scale associated with the resolution of the problem itself, L . These two scales are important, as the mathematical description of your model depends on how these two scales compare to one another. This comparison is related through the non-dimensional Knudsen

number:

$$Kn = \frac{\ell}{L}. \quad (1.1)$$

Flows with large Knudsen number ($Kn \gg 10$) require modeling from the kinetic or microscopic perspective as particle interactions become sparse enough compared to the scope of the problem to require a statistical mechanics framework. On the other hand, small Knudsen number flows ($Kn \ll 0.01$) have a problem scale that far exceeds the particle-level interactions present, giving way to an average overall motion within the fluid. This scale dichotomy is demonstrated in Figure 1.1. For small Knudsen flows, a continuum description of the fluid is appropriate for capturing this macroscopic behavior.

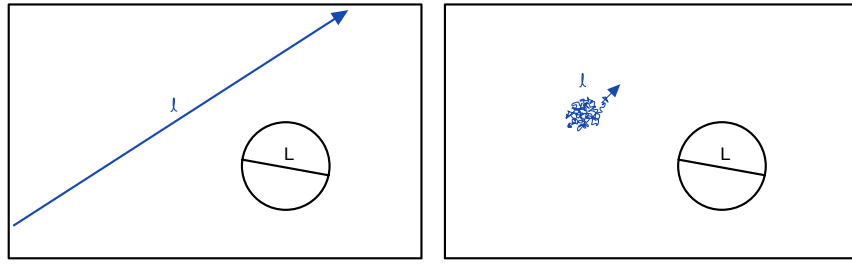


Figure 1.3: Characteristic length scale of problem, L , compared to mean free path of particles, ℓ , for a flow with large Knudsen number (left) vs. small Knudsen number (right)

This work falls within the small Knudsen regime, so we will be working with the continuum description of fluids. In this section we will discuss the Navier-Stokes Equations that arise from this modeling technique and how we account for the supercritical nature of the flow through our choice of equation of state.

1.2.1 Continuum Description of Fluids

The continuum hypothesis assumes that the fluid has no fine structures and that it is perfectly continuous, i.e., the properties of a small subdivision are the same as other subdivisions. This allows for the approximation of physical quantities at the infinitesimal limit [40].

For example, consider a fluid with arbitrary volume V as depicted in Figure 1.4.

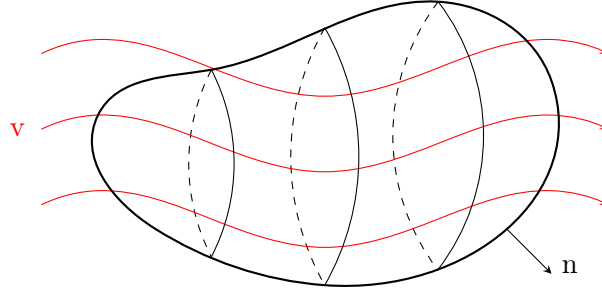


Figure 1.4: A fluid of arbitrary volume V bounded by surface S with velocity $\mathbf{v}(\mathbf{x}, t)$. A differential volume and surface area is given by dv and ds , respectively. \mathbf{n} is the outward-pointing unit normal vector to the surface S .

For a fluid with density $\rho(\mathbf{x}, t)$, mass within a small representative volume can be described with

$$\rho dv.$$

Total mass in the arbitrary volume is then given by

$$\iiint_V \rho dv.$$

The rate of change of mass through the volume is now

$$\begin{aligned} & \frac{d}{dt} \iiint_V \rho dv \\ &= \iiint_V \frac{\partial \rho}{\partial t} dv. \end{aligned} \tag{1.2}$$

Simultaneously, overall change in mass throughout the volume can be described by the net mass flux through the surface S . Volumetric flow through a small portion of the bounding surface is given by

$$\mathbf{v} \cdot \mathbf{n} ds.$$

Total mass flux through the entire surface is then

$$\iint_S \rho \mathbf{v} \cdot \mathbf{n} ds. \tag{1.3}$$

Applying the divergence theorem to Equation (1.3) yields the following volume integral

$$\iiint_V \nabla \cdot (\rho \mathbf{v}) dv. \tag{1.4}$$

Assuming there is no additional source generating or leaking mass within the control volume, we can relate Equations (1.2) to (1.4) :

$$\begin{aligned} \iiint_V \frac{\partial \rho}{\partial t} dv &= - \iiint_V \nabla \cdot (\rho \mathbf{v}) dv \\ \iiint_V \frac{\partial \rho}{\partial t} dv + \iiint_V \nabla \cdot (\rho \mathbf{v}) dv &= 0 \\ \iiint_V \left(\frac{\partial \rho}{\partial t} + \nabla \cdot (\rho \mathbf{v}) \right) dv &= 0. \end{aligned} \quad (1.5)$$

Note the inclusion of the negative sign for the right side of the initial equality; in the surface integral formulation, the outward facing normal describes flux out of the volume, thus yielding a decrease in mass within the volume. Since Equation (1.5) holds for any arbitrary volume V , the integrand must be identically equal to zero:

$$\frac{\partial \rho}{\partial t} + \nabla \cdot (\rho \mathbf{v}) = 0. \quad (1.6)$$

Through the continuum hypothesis and conservation of mass, we have now arrived at the continuity equation in Equation (1.6). This specific process demonstrates an even more fundamental relationship known as a *conservation law*. More generally, for some integrated property ϕ , the rate of change of ϕ within a control volume must equal the amount of ϕ lost or gained through the boundaries of the control volume plus what is created or consumed by any sinks or sources, s , within the volume (sinks having positive orientation to match the positive orientation of the outward-facing normal \mathbf{n}) [10]:

$$\frac{\partial \phi}{\partial t} + \nabla \cdot (\phi \mathbf{v}) + s = 0. \quad (1.7)$$

In addition to this concept applying to conservation of mass, as was seen in this section, the idea outlined by Equation (1.7) applies to conservation of momentum and energy within the fluid. Together, these expressions combine to form the basis of the Navier-Stokes Equations, as will be seen in more detail in Chapter 2. The important takeaway from this section is that with the continuum hypothesis and fundamental laws of physics, one can adequately capture macroscopic flow behavior for the types of flows we are interested in within this work.

1.2.2 Equation of State

Conservation of mass, momentum, and energy gives us five equations to describe our fluid system. For compressible flows, this is not enough information to solve for all the unknowns within the system of coupled partial differential equations. A sixth equation, known as the Equation

of State (EoS), must be chosen in order to close the system. The EoS relates three of the six unknowns: pressure, temperature, and density. Here we briefly discuss some EoS options and their distinguishing characteristics in order to motivate the choice made for this work.

The simplest option available is the ideal gas EoS, which comes from the ideal gas law. This EoS relates density, pressure, and temperature in the following manner:

$$p = \frac{RT}{V_m}, \quad (1.8)$$

where p is pressure, R is the universal gas constant, T is temperature, and $V_m = \frac{V}{n}$ is the molar volume of the fluid (it is common to express density in terms of molar volume for sake of simplicity in writing the EoS with V being volume and n being the number of moles). The ideal gas EoS is fairly accurate for liquids and gases at moderate temperatures and low pressures. It fails at low temperatures and high pressures, especially near the transition region from gas to liquid. The inaccuracy noted in this region means this EoS would not be suitable for the area of interest within this study.

Cubic EoS generally provide more accuracy than the ideal gas EoS. The first cubic EoS was developed by van der Waal in 1873 [95], modifying the ideal gas EoS to take into consideration the finite size of molecules and interactions between molecules (the ideal gas EoS only accounts for interactions with the container and treats molecules as point particles). Other cubic EoS can be thought of as modifications from this base form:

$$p = \frac{RT}{V_m - b} - \frac{a}{V_m^2}, \quad (1.9)$$

where a and b are constants related to the pressure and temperature at the critical point, p_c and T_c respectively:

$$a = \frac{27(RT_c)^2}{64p_c}, \quad b = \frac{RT_c}{8p_c}.$$

One of the main benefits of using a cubic EoS is that they can have comparable and sometimes even better accuracy compared to their higher-order counterparts, thus reducing computational costs. However, it is important to take into consideration the regime of interest in addition to the fluid of interest when choosing an EoS, as each one has its own pros and cons. For example, molecule polarity and density are two factors that can have a high impact in selection between the Soave-Redlich-Kwong Equation of State (SRK EoS) and Peng-Robinson Equation of State (PR EoS) alone [34].

This work uses the SRK EoS as will be more thoroughly introduced in Chapter 3. A detailed investigation into the accuracy of various EoS near the critical point of sCO₂ can be found in [80]. Accuracy for our cases specifically is detailed further in Chapter 3 through comparisons with data from National Institute of Standards and Technology (NIST). Overall, when adequately considered, the EoS is the key avenue to incorporating specific fluid properties into the mathematical model.

1.3 Turbulence

In addition to categorizing by fluid type, fluid flow can be categorized based on flow characteristics. The main two classifications of note are laminar flow and turbulent flow.

Laminar flow is denoted by fluid particles having well-defined parallel trajectories of motion, or streamlines. Streamlines do not cross, meaning adjacent layers within the fluid flow by one another with little to no mixing. From a more generalized perspective, the flow appears to be smooth. In contrast to this, turbulent flow is characterized by its unpredictable and chaotic trajectories. Streamlines do cross resulting in swirls and eddies of varying length scales which induce mixing. Turbulent flow can be qualitatively described as being rough due to this high degree of fluctuation within the velocity and pressure fields present. This generalized description is depicted in Figure 1.5.

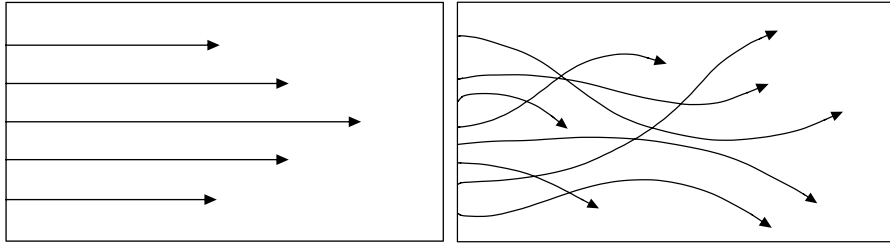


Figure 1.5: Example of streamlines in laminar (left) vs. turbulent (right) flow.

The Reynolds number is a dimensionless value that can be used to distinguish laminar flow from turbulent flow. It is defined as follows:

$$\text{Re} = \frac{\rho u L}{\mu}, \quad (1.10)$$

where ρ and μ are the density and dynamic viscosity of the fluid, respectively, u is the characteristic flow velocity, and L is a characteristic length scale associated with the given flow scenario (e.g., pipe diameter). As is demonstrated by the ratio in Equation (1.10), the Reynolds number measures

the relative effects of inertial forces compared to viscous forces within a given flow scenario. A small Reynolds number signifies the dominance of viscous forces; fluid parcels moving in tandem want to “stick together,” resulting in the sheared flow and parallel trajectories seen in laminar flow. Turbulence is then characterized by a large Reynolds number, where inertial forces take precedence. Here, deviations within the laminar flow field result in lateral mixing between shear layers. This creates eddies and random trajectories that result in the chaotic motion of turbulent flow.

This work focuses on the turbulent round jet and its associated dynamics in the context of supercritical fluids. The remainder of this section details a brief overview of important turbulence concepts and numerical methods developed for studying turbulence in order to motivate the modeling and numerical choices made within this work.

1.3.1 Mathematics of Turbulence

Turbulence has been recognized and investigated by scholars in some way, shape, or form for thousands of years; Lucretius being one of the earliest, describing eddy motion in his *De rerum natura* [11]. In that time, a comprehensive theory of turbulence has still not been reached. There are, however, many widely accepted hypotheses and models that at least in part explain certain aspects of turbulent flows.

Turbulent motion contains a wide range of scales. Richardson formalized this concept by describing turbulence as a compositions of eddies, each with their own characteristic size and velocity [12]. From this perspective, large eddies are said to be unstable and break up into smaller eddies, transferring energy down the line to smaller and smaller eddies. This energy cascade continues down to the molecular level where it is dissipated through molecular viscosity. Kolmogorov further developed this theory, noting that for sufficiently high Reynolds flow, the statistics of these smallest-scale motions are uniquely determined by the kinematic viscosity of the fluid, ν , and the dissipation rate, ε [46]. These smallest eddy length, velocity, and time scales at which dissipation occurs, known as the Kolmogorov scales, are defined as follows:

$$\begin{aligned}\eta &\equiv (\nu^3/\varepsilon)^{1/4}, \\ u_\eta &\equiv (\nu\varepsilon)^{1/4}, \\ \tau_\eta &\equiv (\nu/\varepsilon)^{1/2}.\end{aligned}\tag{1.11}$$

While the continuum description introduced in the previous section is still valid for turbulent flows, this vast scale separation and the random nature of fluctuations across these scales, including

a dependence on problem-specific flow configurations and boundary conditions, make universal solutions to these types of problems unattainable. To that end, numerical simulations are invaluable in studying turbulence phenomena.

1.3.2 Numerical Approaches to Turbulence Modeling

A vast array of numerical approaches have been developed to tackle the modeling challenges inherent to turbulence, with further development of these and new techniques remaining an active field of research today. We will briefly look at three families of numerical simulation methods in order to highlight the challenges associated with the large scale disparity included in turbulent flows. Methods of note include use of the Reynolds-Averaged Navier-Stokes (RANS) equations, direct numerical simulation (DNS), and large eddy simulation (LES), with scale coverage of each outlined in Figure 1.6.

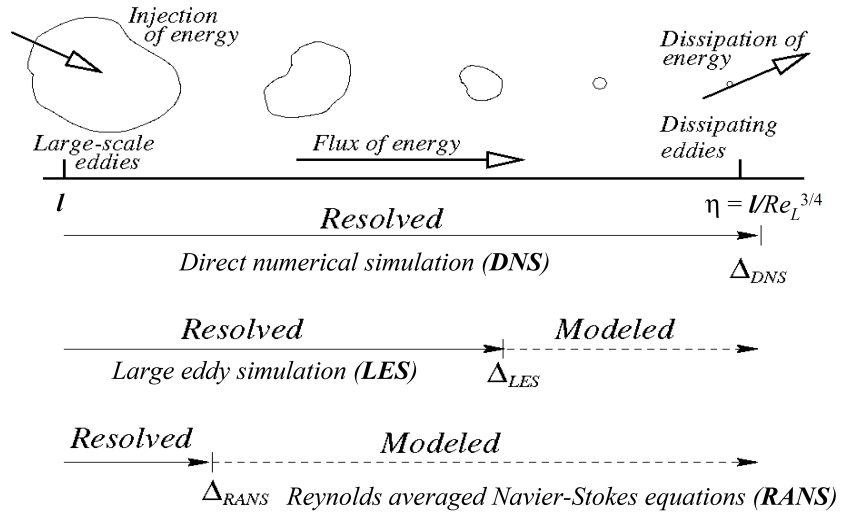


Figure 1.6: Depiction of the energy cascade present in turbulence along associated scales. Resolved vs. Modeled scales are mapped for DNS, LES, and RANS [8].

At one extreme, we have DNS. The aim of DNS to resolve all scales within the turbulent flow, from the largest eddies down to the Kolmogorov scale. To do this, all components of the Navier-Stokes equations are discretized and numerically advanced. Numerical methods may include high-order finite differencing or pseudo-spectral methods depending on the type of turbulence, flow configuration, and boundary conditions at hand. While DNS can capture physics across all scales of the flow with high accuracy, this comes at a steep computational cost. Grid spacing and time

stepping are highly dependent upon the Reynolds number (approximately as Re^3 [76]). Thus DNS very quickly becomes limited to lower Reynolds flows, even with high computing resources.

On the other end of the spectrum, we have RANS modeling. The RANS equations make use of the Reynolds decomposition of the flow, in which a random velocity field \mathbf{u} can be split into an ensemble average, $\langle \mathbf{u} \rangle$, and a fluctuating component, \mathbf{u}' , such that:

$$\begin{aligned}\mathbf{u}'(\mathbf{x}, t) &\equiv \mathbf{u}(\mathbf{x}, t) - \langle \mathbf{u}(\mathbf{x}, t) \rangle, \\ \langle \mathbf{u}(\mathbf{x}, t) \rangle &= \lim_{N \rightarrow \infty} \frac{1}{N} \sum_{i=1}^N \mathbf{u}_i(\mathbf{x}, t),\end{aligned}\tag{1.12}$$

where i is the i^{th} realization of a flow of identical conditions with the number of realizations N tending toward infinity. In practice, for numerical models with the RANS equations, this is implemented via time averaging:

$$\langle \mathbf{u}(\mathbf{x}, t) \rangle \approx \overline{\mathbf{u}(\mathbf{x})} \equiv \frac{1}{T} \int_{t_0}^{t_0+T} \mathbf{u}(\mathbf{x}, s) ds,$$

where T is taken to be much larger than the time scale of the fluctuating components. By substituting $\mathbf{u}(\mathbf{x}, t) = \overline{\mathbf{u}(\mathbf{x})} + \mathbf{u}'(\mathbf{x}, t)$ particular substitution into the Navier-Stokes equations, one can get a statistical description of the average flow field for the turbulent system. Note that the more general decomposition given in equation (1.12) can be used in the substitution as well to take into consideration a moving average within the flow field. For many of the applications in which RANS is used, it is enough to look at the steady state given by the time averaged system. Further equations are then needed to model the additional stresses that arise from the nonlinear interactions between components of the mean flow field. Overall, simulations of the RANS equations resolve the larger scale motions associated with the average motion of the field in a statistical description of the system while the influence of fluctuating fields are incorporated via modeling. While this reduces the computational cost of the numerics, more closure issues arise from the modeling requirements introduced, which present a whole new set of choices and assumptions that are highly problem specific.

Finally, we have LES, which falls between the two extremes of the methodology spectrum presented thus far. The strategy with LES is to only resolve the energy containing scales in the system and model the influence of the smaller scales, as demonstrated in Figure 1.7. This allows for some relaxation in computational cost compared to DNS without introducing the same degree of modeling assumptions required for RANS. While still fairly computationally expensive overall, LES can

resolve more of the instantaneous flow field and capture certain physics that inherently depend on the small scale dynamics; quantities of this nature are lost or become highly model dependent in RANS which introduces more error to the simulation.

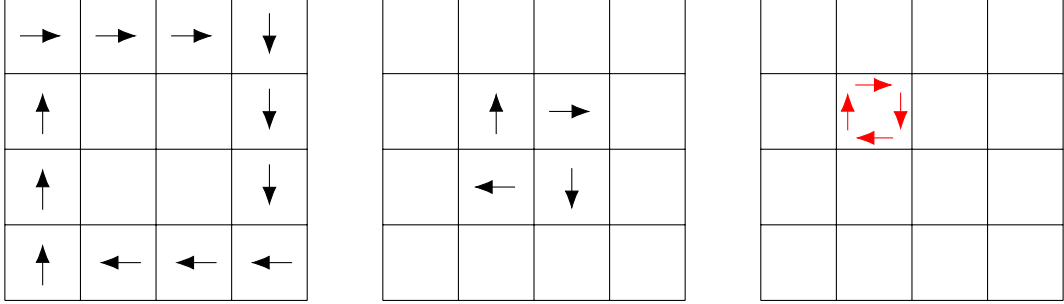


Figure 1.7: LES resolves large-scale eddies (black) and models the effects of fine-scale eddies (red) that are unresolved due to mesh size.

The procedure for LES involves decomposing random velocity field \mathbf{u} into filtered components, $\bar{\mathbf{u}}$, and residual components, \mathbf{u}'' , such that:

$$\begin{aligned}\mathbf{u}''(\mathbf{x}, t) &\equiv \mathbf{u}(\mathbf{x}, t) - \overline{\mathbf{u}(\mathbf{x}, t)}, \\ \overline{\mathbf{u}(\mathbf{x}, t)} &= \int_{-\infty}^{\infty} \int_{-\infty}^{\infty} \mathbf{u}(\mathbf{r}, s) G(\mathbf{x} - \mathbf{r}, t - s) d\mathbf{r} ds,\end{aligned}\tag{1.13}$$

where G is the convolution kernel of associated filter spatial and/or temporal cutoff Δ and τ_c , respectively, satisfying $\int_{-\infty}^{\infty} \int_{-\infty}^{\infty} G(\mathbf{r}, s) d\mathbf{r} ds = 1$. In practice, common kernels are only spatially dependent. Applying this filtering procedure to the Navier-Stokes equations yields an additional term known as the residual stress tensor that must be modeled. The filtered Navier-Stokes equations can then be discretized to numerically simulate the large eddy behavior of the system.

This general LES procedure may seem similar to what was described for the RANS model, especially in terms of the decomposition of the flow field, but there are key differences to note. Conceptually, the result of a numerical simulation using RANS describes an average behavior of turbulent flow over many instances or experiments. The output of these simulations is not a snapshot of one instance of the given flow field but rather an approximation to how the flow behaves in a statistical sense. LES does approximate a single realization of the flow field, just only including the low frequency modes of the system which contain the majority of the energy. Additionally, the components of the Reynolds decomposition obey the following rules:

$$\bar{\mathbf{u}} = \bar{\mathbf{u}}, \quad \overline{\mathbf{u}'} = 0.$$

These rules do not hold for $\bar{\mathbf{u}}$ and \mathbf{u}'' :

$$\bar{\mathbf{u}} \neq \bar{\mathbf{u}}, \quad \bar{\mathbf{u}''} \neq 0.$$

We use LES in this work to balance the computational cost of the simulation with the degree of resolution for physical phenomena within the flow. Many studies involving turbulent supercritical fluids utilize LES, as will be seen in the next section, with additional research having been conducted regarding appropriate choices in modeling for the residual stress tensor. Model selection and further details on filtering are discussed in Chapter 2.

1.4 Current Research Landscape

Here we provide a brief overview of some of the current trends in research regarding supercritical fluids. Both experimental and numerical works are discussed in order to highlight the challenges associated with studying supercritical fluids and what approaches are common practice in doing so. This is not an exhaustive review by any means, but provides insights into the general landscape for which this work fits in.

1.4.1 Experimental Contributions

Current experimental research is mainly application oriented. Research into the sCO₂ jet's rock breaking ability has been of primary importance to Enhanced Geothermal Systems (EGS) applications [77, 78, 54, 89, 52], with additional focus being given to pipeline leakage and flow dynamics upon wall impact [97, 96], which unfortunately does not explore the underlying turbulence statistics of the flow. Enhanced recovery of unconventional reservoirs for oil and gas development is an additional area where rock breaking research is often applied [39, 38]. Chemical engineering design aspects of sCO₂ injection are more focused on solubility dynamics as opposed to turbulence [43, 48]. Other experiments focus on similar application specific quantities of interest, such as heat transfer and mixing, which is related in part to the turbulence dynamics [106, 55], but they also note the difficulty in experimental design for investigating these aspects of the flow under the conditions needed to replicate those in real applications [43]. Thus, numerical simulations are necessary to further explore the turbulence statistics of these flows.

1.4.2 Numerical Contributions

Numerical simulations are a necessary tool for investigating many aspects of supercritical flow fields due to the often challenging nature of experiment design for the extreme conditions inherent to

these systems. Studies using DNS have been implemented to help establish benchmark test cases for other types of numerical schemes [67, 88]. Ruiz et al. use 2D DNS to simulate a mixing layer created by two streams of supercritical Oxygen and gaseous Nitrogen, using two different computational fluid dynamics (CFD) solvers to add confidence to their results [85]. A 3D DNS is used by Ries et al. to simulate a round Nitrogen jet for comparison with experimental data produced by Mayer et al. [82]. However, this study requires a reduction in Reynolds number from 1.62×10^5 , based on the injection diameter, to 5300 in order to feasibly execute the computations. Li also utilizes a low Reynolds number of 1750 to study a round turbulent sCO₂ jet with a preconditioning scheme [51]. The RANS approach has also been implemented utilizing theory from the ideal gas case [58], but with the goal of ascertaining a more general understanding of why specifically sCO₂'s rock-breaking ability is better than that of water.

Much research has gone into the development of appropriate numerical methods for investigations regarding turbulence in supercritical fluids. In order to maintain a high Reynolds flow and better capture the effects of the supercritical nature of the fluid on the turbulence dynamics, the use of LES has been explored. The impact of subgrid-scale (SGS) models in capturing transcritical and supercritical dynamics of cryogenic Nitrogen have been analyzed through comparison with the Mayer et al. experiment and highly accurate NIST data [72, 112, 113, 64, 100]. Schmitt et al. does a similar investigation using LES, then extending their investigation to include sCO₂ after validation with the Mayer et al. data [87]. However, this investigation uses low-pressure jets and does note the SGS models might need additional contributions to handle non-linearities and the pressure regime. While many of these investigations note that SGS models may need modification to deal with supercritical flows [87, 72, 64, 112], it is noted by Müller et al. that given a sufficiently fine grid, the influence of SGS modeling and numerical flux discretization is essentially limited to second-order moments [64]. Thus, we will be using the compressible version of the dynamic Smagorinsky SGS closures for our investigation, with further consideration of any influence of SGS model on our quantities of interest being noted later on.

Many of the numerical investigations cited thus far consider cryogenic nitrogen in order to compare with the Mayer et al. experiment on supercritical jet turbulence [60]. A wide variety of numerical investigations into jet turbulence using sCO₂ exist but typically explore other parameter regimes of interest or application-specific quantities of interest. Examples of turbulent adjacent quantities of interest include fluctuation characteristics based on inlet conditions [109], effects of nozzle and aperture differences on pressure and velocity decay [15] and wave features [57], mixing

between sCO₂ and other fluid phases [79], and energy dissipation [53]. These studies all involve high pressure jets and are commonly found in applications involving rock fracturing. Related configurations are also studied, such as the swirling-round sCO₂ jet [105], turbulent jet-in-crossflows [108], slot jet impingement [2], and channel flow [**ROGALEV2020**].

While much of the literature thus far has explored the impact of different numerical methods on modeling supercritical fluid flows and has aimed to strengthen the validity of these simulations in spite of the lack of experimental data available in the current landscape, a general consensus has still not been reached on how the supercritical nature of these fluids impacts the turbulence physics of these models. Thus, there remain open questions for understanding the fundamental flow behavior of turbulent jets in a supercritical environment, especially near the supercritical point, where both experimental and numerical investigations are still a challenge.

Our objective is to use LES to investigate the turbulence physics of sCO₂ near the critical point in order to capture the effects of widely varying thermal properties of supercritical fluids. Using the compressible Navier-Stokes equation solver, *PeleC* [37, 90], closed with the SRK EoS, we consider three cases in order to examine various quantities of interest associated with classical turbulence mechanics. These three cases are chosen to capture different areas around a peak in specific heat that is associated with the pseudo-critical region. The rest of this dissertation is outlined as follows. Chapter 2 details the model used for this study. Chapter 3 gives an overview of the numerical methods implemented through *PeleC*. Chapter 4 outlines the simulation setup with parameter choices and validation. Results for cross-case comparisons and comparisons with external work are then presented in Chapter 5, with a summary and future work detailed in Chapter 6.

CHAPTER 2

MODEL OVERVIEW

2.1 Introduction

This section details the governing equations used to simulate the sCO₂ jet. All models and equations described here are from *PeleC* [37, 90], a compressible hydrodynamics code for reacting flows that leverages *AMReX* [111, 110, 41] for AMR. It also leverages the *PelePhysics* library for complex physics, including chemical reactions, non-ideal EoS, and high fidelity transport models. As introduced previously, the compressible Navier-Stokes equations form the basis of the model along with the SRK EoS. Here we also detail the filtering used in the LES and the dynamic Smagorinsky (SMD) used to model the SGS dynamics [59]. We also describe the transport and thermodynamic models used for incorporating into the system real fluid dynamics involving supercritical conditions.

2.2 Governing Equations

We consider the three-dimensional compressible Navier-Stokes equations, presented here with Einstein notation:

$$\frac{\partial \rho}{\partial t} + \frac{\partial}{\partial x_j} (\rho u_j) = 0, \quad (2.1a)$$

$$\frac{\partial}{\partial t} (\rho u_i) + \frac{\partial}{\partial x_j} (\rho u_i u_j + p \delta_{ij} - \sigma_{ij}) = 0, \quad (2.1b)$$

$$\frac{\partial}{\partial t} (\rho E) + \frac{\partial}{\partial x_j} ((\rho E + p) u_j + q_j - \sigma_{ij} u_i) = 0, \quad (2.1c)$$

where ρ is the density, u_j is the velocity for the x_j direction, p is the pressure, $E = e + \frac{u_i u_i}{2}$ is the total energy, e is the internal energy, and T is the temperature. Following the assumptions made for Newtonian fluids [10], the diffusive fluxes are

$$\sigma_{ij} = 2\mu S_{ij} - \frac{2}{3}\mu\delta_{ij}S_{kk}, \quad q_j = -\lambda \frac{\partial T}{\partial x_j}, \quad (2.2)$$

where $S_{ij} = \frac{1}{2} \left(\frac{\partial u_i}{\partial x_j} + \frac{\partial u_j}{\partial x_i} \right)$ is the strain-rate tensor, μ is the dynamic viscosity, and λ is the thermal conductivity. Models regarding these two components are given in more detail in the next section.

δ_{ij} here is the Kronecker delta. External forces such as gravity are not included in this study. The system is closed using the SRK EoS [91] to relate pressure, density, and temperature as follows:

$$\begin{aligned} p &= \frac{RT}{V_m - b} - \frac{a\alpha}{V_m(V_m + b)}, \\ a &= \frac{0.42747R^2T_c^2}{P_c}, \\ b &= \frac{0.08664RT_c}{P_c}, \\ \alpha &= (1 + (0.48508 + 1.55171\omega - 0.15613\omega^2)(1 - T_r^{0.5}))^2, \end{aligned} \quad (2.3)$$

where R is the ideal gas constant, T_c and P_c are the critical temperature and pressure of the species, respectively, $T_r = T/T_c$ is the reduced temperature given by the ratio of the absolute temperature to the critical temperature, V_m is the molar volume of the species, and ω is the acentric factor of the species. All cases are run with a single species, that being CO₂.

2.2.1 Filtered Navier-Stokes Equations

To perform the LES, we consider the filtered compressible Navier-Stokes equations as implemented by Martín, Piomelli, and Candler [59]. Here we go through a brief derivation along with the main assumptions needed. First, applying the filtering operation from Equation (1.13) to Equations (2.1), we get:

$$\frac{\partial \bar{\rho}}{\partial t} + \frac{\partial}{\partial x_j} (\bar{\rho} \bar{u}_j) = 0, \quad (2.4a)$$

$$\frac{\partial}{\partial t} (\bar{\rho} \bar{u}_i) + \frac{\partial}{\partial x_j} (\bar{\rho} \bar{u}_i \bar{u}_j + \bar{p} \delta_{ij} - \bar{\sigma}_{ij}) = 0, \quad (2.4b)$$

$$\frac{\partial}{\partial t} (\bar{\rho} \bar{E}) + \frac{\partial}{\partial x_j} ((\bar{\rho} \bar{E} \bar{u}_j + \bar{p} \bar{u}_j) + \bar{q}_j - \bar{\sigma}_{ij} \bar{u}_i) = 0. \quad (2.4c)$$

In order to avoid having to model $\bar{\rho} \bar{u}_j$ in the conservation of mass equation in (2.4), Favre-filtering, $\tilde{\cdot} = \bar{\rho} \cdot / \bar{\rho}$, is also applied [31]. Additionally, the following two sets of assumptions are made regarding transport terms [73]:

$$\overline{\mu(T) S_{ij}} \simeq \mu(\tilde{T}) \widetilde{S_{ij}}, \quad \overline{\lambda(T) \frac{\partial T}{\partial x_j}} \simeq \lambda(\tilde{T}) \frac{\partial \tilde{T}}{\partial x_j}, \quad (2.5a)$$

$$\tilde{\mu} = \mu(\tilde{T}), \quad \tilde{\lambda} = \lambda(\tilde{T}). \quad (2.5b)$$

The assumptions in Equations (2.5) are common in the literature regarding LES, even though transport terms depend nonlinearly on temperature [73]. Justification for this type of assumption can be made where if performing LES with coarse enough grid, molecular transport coefficients

remain small compared to turbulent transport coefficients [84]. Applying Equations (2.5) along with the Favre filter to Equations (2.4) yields the following:

$$\begin{aligned}\frac{\partial \bar{\rho}}{\partial t} + \frac{\partial}{\partial x_j} (\bar{\rho} \tilde{u}_j) &= 0, \\ \frac{\partial}{\partial t} (\bar{\rho} \tilde{u}_i) + \frac{\partial}{\partial x_j} (\bar{\rho} \tilde{u}_i \tilde{u}_j + \bar{p} \delta_{ij} - \widetilde{\sigma_{ij}}) &= 0, \\ \frac{\partial}{\partial t} (\bar{\rho} \tilde{E}) + \frac{\partial}{\partial x_j} \left((\bar{\rho} \widetilde{E u_j} + \bar{p} \tilde{u}_j) + \widetilde{q_j} - \widetilde{\sigma_{ij} u_i} \right) &= 0,\end{aligned}\quad (2.6)$$

with filtered Equations (2.2) now given by:

$$\widetilde{\sigma_{ij}} = 2\tilde{\mu} \widetilde{S_{ij}} - \frac{2}{3} \tilde{\mu} \delta_{ij} \widetilde{S_{kk}}, \quad \widetilde{q_j} = -\tilde{\lambda} \frac{\partial \tilde{T}}{\partial x_j}. \quad (2.7)$$

Final simplifications to Equations (2.6) come from the SGS terms. The SGS stress τ_{ij} , SGS heat flux \mathcal{Q}_j , SGS turbulent diffusion $\partial \mathcal{J}_j / \partial x_j$, and SGS turbulent viscous diffusion $\partial \mathcal{D}_j / \partial x_j$ are set through the following definitions [59]:

$$\begin{aligned}\tau_{ij} &= \bar{\rho} (\widetilde{u_i u_j} - \widetilde{u_i} \widetilde{u_j}), \\ \mathcal{Q}_j &= \bar{\rho} (\widetilde{u_j T} - \widetilde{u_j} \widetilde{T}), \\ \mathcal{J}_j &= \bar{\rho} (\widetilde{u_j u_k u_k} - \widetilde{u_j} \widetilde{u_k} \widetilde{u_k}), \\ \mathcal{D}_j &= \bar{\rho} (\widetilde{\sigma_{ij} u_i} - \widetilde{\sigma_{ij}} \widetilde{u_i}).\end{aligned}\quad (2.8)$$

After substituting the appropriate pieces of Equations (2.8) into the momentum and energy components of (2.6) and applying a few further assumptions, we eventually get the following:

$$\frac{\partial \bar{\rho}}{\partial t} + \frac{\partial}{\partial x_j} (\bar{\rho} \tilde{u}_j) = 0, \quad (2.9a)$$

$$\frac{\partial}{\partial t} (\bar{\rho} \tilde{u}_i) + \frac{\partial}{\partial x_j} (\bar{\rho} \tilde{u}_i \tilde{u}_j + \bar{p} \delta_{ij} - \widetilde{\sigma_{ij}}) = -\frac{\partial \tau_{ij}}{\partial x_j}, \quad (2.9b)$$

$$\frac{\partial}{\partial t} (\bar{\rho} \tilde{E}) + \frac{\partial}{\partial x_j} \left((\bar{\rho} \widetilde{E} + \bar{p}) \widetilde{u}_j + \widetilde{q_j} - \widetilde{\sigma_{ij} u_i} \right) = -\frac{\partial}{\partial x_j} \left(\gamma c_v \mathcal{Q}_j + \frac{1}{2} \mathcal{J}_j - \mathcal{D}_j \right), \quad (2.9c)$$

with $\gamma = c_p/c_v$. The simplification above hinges upon relating enthalpy to internal energy and pressure as in the ideal gas case with $h = e + p/\rho = c_p T$ with c_p assumed to be constant. Neither of these assumptions is consistent with supercritical fluids but is chosen here for ease of splitting Equations (2.9) into simulated vs. modeled quantities. This is also standard practice in many supercritical LES studies [100, 2, 72], though these assumptions leave room for future work on incorporating higher order EoS into the LES derivation.

Finally, it is also noted that the divergence of the SGS heat flux and the SGS turbulent diffusion are of comparable order of magnitude while the SGS viscous diffusion is an order of magnitude

smaller [59]. Therefore, the SGS turbulent viscous diffusion is omitted from the system. The final set of equations to be discretized and advanced is:

$$\frac{\partial \bar{\rho}}{\partial t} + \frac{\partial}{\partial x_j} (\bar{\rho} \tilde{u}_j) = 0, \quad (2.10a)$$

$$\frac{\partial}{\partial t} (\bar{\rho} \tilde{u}_i) + \frac{\partial}{\partial x_j} (\bar{\rho} \tilde{u}_i \tilde{u}_j + \bar{p} \delta_{ij} - \tilde{\sigma}_{ij}) = -\frac{\partial \tau_{ij}}{\partial x_j}, \quad (2.10b)$$

$$\frac{\partial}{\partial t} (\bar{\rho} \tilde{E}) + \frac{\partial}{\partial x_j} \left((\bar{\rho} \tilde{E} + \bar{p}) \tilde{u}_j + \tilde{q}_j - \tilde{\sigma}_{ij} \tilde{u}_i \right) = -\frac{\partial}{\partial x_j} \left(\gamma c_v \mathcal{Q}_j + \frac{1}{2} \mathcal{J}_j \right), \quad (2.10c)$$

with Equations (2.7) describing the filtered transport coefficients. The SGS stress τ_{ij} , SGS heat flux \mathcal{Q}_j , and SGS turbulent diffusion \mathcal{J}_j need to be modeled in order to close the system.

While Equations (2.10) are the equations discretized within *PeleC*, in practice, we evolve these filtered quantities without explicitly filtering the solution. Here, the grid serves as the main filter for the LES while the specific box filter described in the next section is used to determine model coefficients.

2.2.2 Subgrid-Scale Modeling for Large Eddy Simulation

We use the SMD LES model for compressible flow as described by Martín, Piomelli, and Candler [59]. In this work, the grid provides the implicit filtering of the equations. The SGS stress tensor, τ_{ij} , is included in the diffusive fluxes and is calculated as follows:

$$\begin{aligned} \tau_{ij} - \frac{\delta_{ij}}{3} \tau_{kk} &= -C_s^2 2 \bar{\Delta}^2 \bar{\rho} |\tilde{S}| \left(\tilde{S}_{ij} - \frac{\delta_{ij}}{3} \tilde{S}_{kk} \right) = C_s^2 \alpha_{ij}, \\ \tau_{kk} &= C_I 2 \bar{\rho} \bar{\Delta}^2 |\tilde{S}|^2 = C_I \alpha, \end{aligned} \quad (2.11)$$

with $\bar{\Delta}$ being the filter width associated with the smallest scale retained by the filtering operation ($\bar{\Delta}$ is the grid spacing for our cases). Additionally, $|\tilde{S}| = (2 \tilde{S}_{ij} \tilde{S}_{ij})^{1/2}$. The two model coefficients are calculated as follows:

$$C = C_s^2 = \frac{\langle \mathcal{L}_{ij} M_{ij} \rangle}{\langle M_{kl} M_{kl} \rangle}, \quad C_I = \frac{\langle \mathcal{L}_{kk} \rangle}{\langle \beta - \hat{\alpha} \rangle}, \quad (2.12)$$

where the Germano identity, $\mathcal{L}_{ij} = T_{ij} - \hat{\tau}_{ij}$, is used to relate the SGS stress tensor to the “resolved turbulent stresses”, $\mathcal{L}_{ij} = \left(\overline{\rho u_i \hat{\rho} u_j / \bar{\rho}} \right) - \widehat{\rho u_i \hat{\rho} u_j / \bar{\rho}}$, and the subtest stresses, $T_{ij} = \widehat{\rho u_i \check{u}_j} - \widehat{\rho \check{u}_i \check{u}_j}$ [33]. In this relationship, a hat denotes quantities associated with a test filter \hat{G} which has a characteristic length of $\hat{\Delta}$. The breve denotes Favre-filtered quantities using \hat{G} (i.e., $\check{f} = \widehat{\rho f / \bar{\rho}}$). Additionally, $M_{ij} = \beta_{ij} - \widehat{\alpha_{ij}}$ with $\beta_{ij} = -2 \hat{\Delta}^2 \widehat{\rho} |\tilde{S}| \left(\check{S}_{ij} - \delta_{ij} \tilde{S}_{kk} / 3 \right)$ and $\beta = 2 \hat{\Delta}^2 \widehat{\rho} |\tilde{S}|^2$.

The SGS heat flux \mathcal{Q}_j is also modeled dynamically as in [59]:

$$\mathcal{Q}_j = -\frac{\bar{\rho}\nu_T}{Pr_T} \frac{\partial \tilde{T}}{\partial x_j} = -C \frac{\bar{\Delta}^2 \bar{\rho} |\tilde{S}|}{Pr_T} \frac{\partial \tilde{T}}{\partial x_j}, \quad (2.13)$$

where C is modeled as in Equation (2.12) and the turbulent Prandtl number, Pr_T , is calculated dynamically as:

$$Pr_T = \frac{C \langle T_k T_k \rangle}{\langle \mathcal{K}_j T_j \rangle}, \quad (2.14)$$

where

$$T_j = -\bar{\Delta}^2 \widehat{\bar{\rho}} |\tilde{S}| \frac{\partial \tilde{T}}{\partial x_j} + \bar{\Delta}^2 \bar{\rho} |\tilde{S}| \widehat{\frac{\partial \tilde{T}}{\partial x_j}}, \quad \mathcal{K}_j = \left(\frac{\widehat{\bar{\rho} u_j \bar{\rho} T}}{\widehat{\bar{\rho}}} \right) - \frac{\widehat{\bar{\rho} u_j \bar{\rho} T}}{\widehat{\bar{\rho}}}. \quad (2.15)$$

Finally, the SGS turbulent diffusion \mathcal{J}_j is modeled following the strategy proposed by Knight et al. [44]:

$$\mathcal{J}_j = \tilde{u}_k \tau_{jk} \quad (2.16)$$

For our simulations, we implement the three point box filter as described in [86] with a filter-grid ratio of 2, i.e. $\widehat{\Delta} = 2\bar{\Delta}$. With this filter, the convolution kernel from Equation (1.13) is defined as follows:

$$G(\mathbf{x} - \mathbf{r}) = \begin{cases} \frac{1}{\widehat{\Delta}} & |\mathbf{x} - \mathbf{r}| \leq \frac{\widehat{\Delta}}{2}, \\ 0 & \text{otherwise.} \end{cases} \quad (2.17)$$

A discretized form of Equation (2.17) is needed for the test filter in calculating the SMD model coefficients. *PeleC* contains a variety of filtering options. In one dimension, this discretization results in the following implementation:

$$\bar{\phi}_i = \frac{1}{24} \epsilon^2 (\phi_{i+1} + \phi_{i-1}) + \frac{1}{12} (12 - \epsilon^2) \phi_i \quad i = 1, 2, \dots, N, \quad (2.18)$$

where ϵ is the grid filter ratio, which in our case is equal to two. Additionally, the subscript i represents a given grid cell for N discretized cells. This filter is used for any of the quantities containing a hat or breve as defined above in Equations (2.12), (2.15), and (2.16).

As noted previously, the choice of SGS modeling is important to accurately capture the turbulence statistics of the system. Müller et al. found that while the choice in thermodynamic modeling is crucial in capturing first-order moments, the effects SGS modeling is limited to second-order moments [64]. Therefore, our conclusions relating to the turbulence dynamics will be unaffected. That being said, [64] also notes that the choice in SGS model and numerical flux discretization had a larger than expected effect on resolved Reynolds stress profiles. Specifically, the constant

Smagorinsky model yielded decaying fluctuation magnitudes during early evolution, resulting in the transition to a fully turbulent mixing zone to start from lower turbulence levels. However, this did agree with the jet break-up location inferred from mean density profiles, which were shifted slightly downstream by comparison to other SGS models. These relationships will be taken into consideration for this study as well and noted in the discussion of Reynolds stress profiles.

2.3 Transport Models

Modeling of transport coefficients is done through *PelePhysics* [6]. There are three modeling options available in *PelePhysics*; we use the *Simple* model. The *Simple* model approximates ideal gas transport coefficients using EGLib functions [28], which have the following form:

$$\ln(q_0) = \sum_{n=1}^4 a_{q,n} (\ln(T))^{n-1}, \quad (2.19)$$

where q_0 is the transport quantity of interest (either thermal conductivity λ or viscosity μ) and a is the appropriate pre-calculated polynomial fit coefficient (see Table A.1). Chung's high pressure correction for viscosity and thermal conductivity are included to account for real gas dynamics [18]:

$$q = q_k + q_p, \quad (2.20)$$

where q_k is the low-pressure gas transport quantity related to the ideal gas quantity q_0 and q_p is the high-pressure deviation.

For viscosity, these quantities are:

$$\begin{aligned} \mu_k &= \mu_0 \left(\frac{1}{G_2} + A_6 Y \right), \\ \mu_p &= \left(\frac{36.344 \times 10^{-6} (MT_c)^{1/2}}{V_c^{2/3}} \right) A_7 Y^2 G_2 \exp \left(A_8 + \frac{A_9}{T^*} + \frac{A_{10}}{T^{*2}} \right), \end{aligned} \quad (2.21)$$

where M is the molecular weight, V_c is the critical molar volume, $T^* = T/\epsilon_k$ is a dimensionless temperature scaling using the Lennard-Jones potential well depth [50], $Y = (\rho V_c)/6$, and $G_1 = (1 - 0.5Y)/(1 - Y)^3$, and $G_2 = \{A_1 [1 - \exp(-A_4 Y)] / Y + A_2 G_1 \exp(A_5 Y) + A_3 G_1\} / (A_1 A_4 + A_2 + A_3)$.

The constants A_{1-10} are linear functions calculated as follows:

$$A_i = a_{i0} + a_{i1}\omega + a_{i2}\mu_r^4 + a_{i3}\kappa \quad i = 1, \dots, 10, \quad (2.22)$$

where μ_r is the reduced dipole moment of the species, κ is the association factor of the species, and a_{ij} are constants (see Table A.3).

Similarly, thermal conductivity components are given by:

$$\begin{aligned}\lambda_k &= \lambda_0 \left(\frac{1}{H_2} + B_6 Y \right), \\ \lambda_p &= \left(\frac{3.039 \times 10^{-4} (T_c/M)^{1/2}}{V_c^{2/3}} \right) B_7 Y^2 H_2 T_r^{1/2},\end{aligned}\quad (2.23)$$

where $H_2 = \{B_1 [1 - \exp(-B_4 Y)] / Y + B_2 G_1 \exp(B_5 Y) + B_3 G_1\} / (B_1 B_4 + B_2 + B_3)$ and B_{1-7} are defined as:

$$B_i = b_{i0} + b_{i1}\omega + b_{i2}\mu_r^4 + b_{i3}\kappa \quad i = 1, \dots, 7, \quad (2.24)$$

where b_{ij} are constants (see Table A.4). All species-related constants mentioned in this section can also be found in Table A.2.

These high pressure corrections as derived and analyzed by Chung et al. show improved accuracy for approximating transport properties over a wide range of temperatures and pressures when compared to experimental data for a variety of species [18].

2.4 Thermodynamics and Related Quantities

Modeling of thermodynamic quantities is also done through *PelePhysics* [6]. In a similar fashion to Equation (2.20), thermodynamic properties can be broken up into an ideal gas component and a departure from ideal gas behavior:

$$q(\phi) = q_I(\phi) + q_D(\phi), \quad (2.25)$$

where ϕ is the appropriate combination of state variables involving temperature, specific volume, and pressure, q_I is the ideal state component and q_D is the departure component. These decompositions can be derived from fundamental thermodynamic relations [10]. For example, change in internal energy can be written as follows:

$$de = \left(\frac{\partial e}{\partial T} \right)_{V_m} dT + \left[T \left(\frac{\partial p}{\partial T} \right)_{V_m} - p \right] dV_m. \quad (2.26)$$

Substituting in the appropriate partial derivative using the SRK EoS and integrating from an ideal state reference point (v_m, t) to general point far from ideal conditions (V_m, T) yields:

$$e(V_m, T) - e(v_m, t) = e(v_m, T) - e(v_m, t) + a \left[\alpha - T \frac{\partial \alpha}{\partial T} \right] \int_{v_m}^{V_m} \frac{1}{V(V+b)} dV. \quad (2.27)$$

Simplifying the left- and right-hand side of Equation (2.27) and utilizing the choice of $v_m \rightarrow \infty$ for the ideal state volume [75], we get:

$$e(V_m, T) = e(\infty, T) + a \left[\alpha - T \frac{\partial \alpha}{\partial T} \right] \int_{\infty}^{V_m} \frac{1}{V(V+b)} dV. \quad (2.28)$$

Evaluating the integral in Equation (2.28), we arrive at the final expression for the internal energy of the species described by the SRK EoS:

$$e(V_m, T) = e_I(T) + a \left[T \frac{\partial \alpha}{\partial T} - \alpha \right] \frac{1}{b} \ln \left(1 + \frac{b}{V_m} \right), \quad (2.29)$$

where $e_I(T) = c_v T$ is the ideal internal energy which only depends on temperature and $e_D(V_m, T) = a \left[T \frac{\partial \alpha}{\partial T} - \alpha \right] \frac{1}{b} \ln \left(1 + \frac{b}{V_m} \right)$ is the departure function for the internal energy. A similar procedure can be done to arrive at the decomposed enthalpy equation involving SRK EoS-specific quantities:

$$h(V_m, T) = h_I(T) + a \left[T \frac{\partial \alpha}{\partial T} - \alpha \right] \frac{1}{b} \ln \left(1 + \frac{b}{V_m} \right) + \frac{RTb}{V_m - b} - \frac{a\alpha}{V_m + b}. \quad (2.30)$$

The departure function can be directly evaluated while the ideal gas portion must be approximated.

Ideal specific heat at constant volume scaled by the ideal gas constant c_{vI}/R is approximated with NASA polynomial fits [61]. These polynomial fits have the following form:

$$\psi(T) = c_{\psi,0} + c_{\psi,1}T + c_{\psi,2}T^2 + c_{\psi,3}T^3 + c_{\psi,4}T^4 + c_{\psi,5}\frac{1}{T}, \quad (2.31)$$

where $c_{\psi,0-5}$ are species-specific constants for each quantity's polynomial fit (see Table B.1). Other ideal gas quantities of interest can also be calculated in this form via integration, so that ψ here can be either ideal internal energy e_I/RT , specific heat at constant volume c_{vI}/R , or enthalpy h_I/RT . The equations for additional thermodynamic quantities, such as constant volume and constant pressure specific heat, and useful derivatives involving the SRK EoS can be found in Appendix B.

2.5 Model Validation

Here we compare some thermodynamic and transport quantities with highly accurate data from the NIST WebBook [49] in order to quantify the error present in our model within the regime of interest. Figure 2.1 depicts constant-pressure specific heat, density, shear viscosity, and thermal conductivity across the parameter regime explored by the three cases noted in this work. Overall, quantities of interest depicted here follow the same general trends as the NIST data, but with larger discrepancies between the two noted near the pseudo-boiling region denoted by the peak in specific

heat. Most of the largest error values can be found in the $314 - 330K$ range, which means modeling errors will have the largest impact on the pseudo-boiling case presented here. Table 2.1 contains the largest percent errors for each quantity along with the temperature value of that peak error location. Future studies will explore methods of achieving higher accuracy in thermodynamic and transport modeling in this challenging parameter regime. Since general trends are still followed by the models, results from this study should still provide insight into this region.

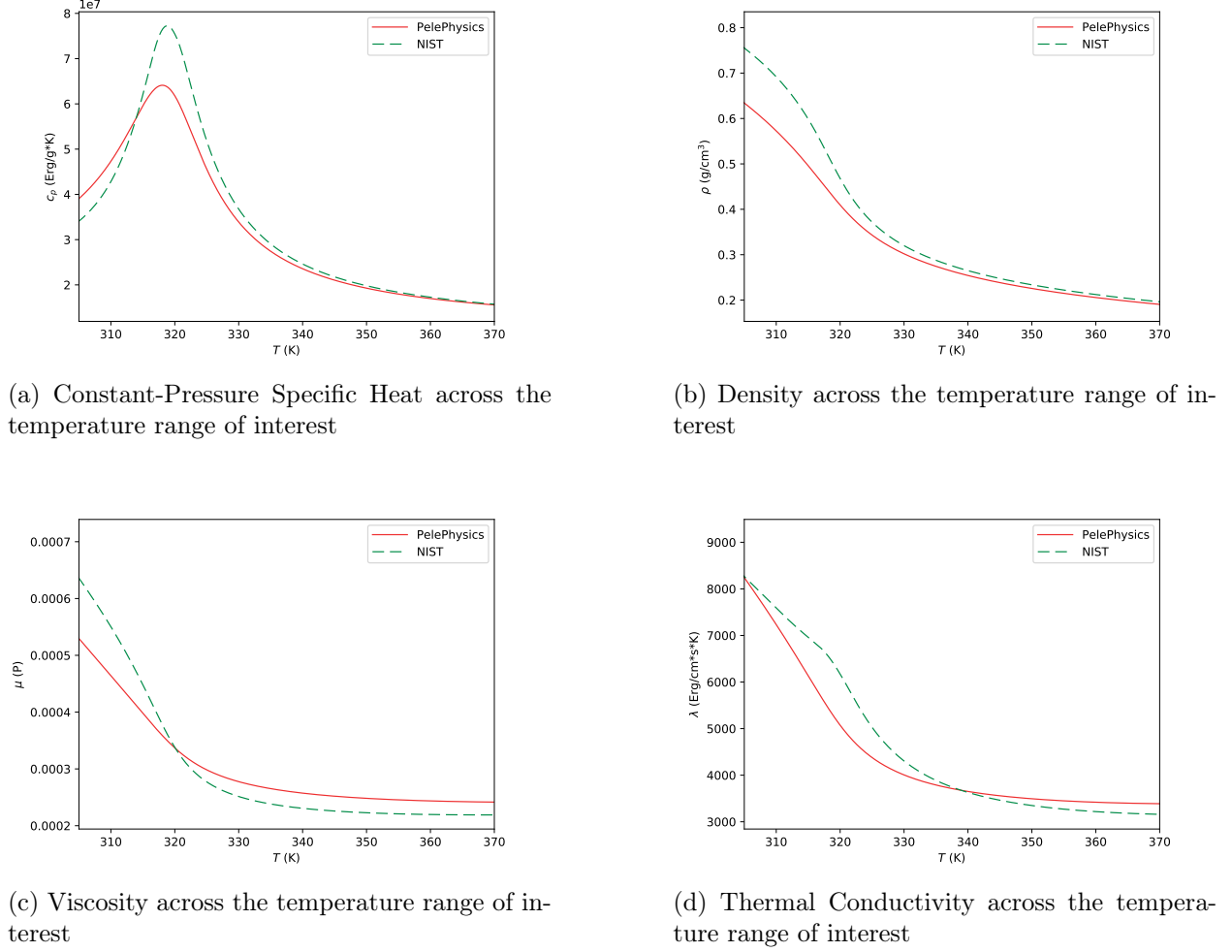


Figure 2.1: Here we compare NIST WebBook values [49] with output values from the thermodynamic and transport models described here as implemented in *PelePhysics*. Challenges of capturing the fluid properties near the critical point can be seen in the increased error near the pseudo-boiling point near $318K$.

Table 2.1: Maximum percent error between NIST WebBook Data and simulation models for constant-pressure specific heat, density, viscosity, and thermal conductivity.

Parameter	Percent Error	Temperature (K)
c_p	18.11	320.25
ρ	17.41	314
μ	12.62	314
λ	17.81	319.88

CHAPTER 3

NUMERICAL METHODS

3.1 Introduction

To discretize and evolve the system of partial differential equations, including the LES SGS terms, we use *PeleC* [37, 90]. *PeleC* is a highly scalable code for heterogeneous architectures that is being developed as part of the Exascale Computing Project (ECP) through the Department of Energy (DOE).

For spatial discretization, *PeleC* contains a few variations of the general piecewise parabolic method (PPM) originally derived by Colella and Woodward [19]. We utilize a variation that allows for extrema preservation in the presence of steep gradients [62, 21]. *PeleC* also has two available time-stepping options: an explicit second-order Method of Lines (MOL) formulation and an iterative scheme base on a Spectral Deferred Correction (SDC) approach [65]. For this work, we use the SDC method.

The rest of this chapter is outlined as follows: first we introduce the general finite volume formulation for conservative systems as this forms the basis of *PeleC*, with an additional note on the foundations in *AMReX*. The remaining sections cover the numerical methods chosen from those available in *PeleC*, with motivation provided as to why they were selected for this work and a basic overview of the method. For additional details as to the specific implementations of said methods within *PeleC*, please see the sources referenced throughout, in addition to the general *PeleC* documentation page [70] and Github repository [5]; the full code is available for download and use. See Appendix C for input parameters used in this work.

3.2 Finite Volume Formulation

PeleC utilizes a finite volume formulation [30] to discretize the system given in Equation (2.10). First, we re-write a slightly modified version of this system in a condensed tensor notation, where the diffusive fluxes have been moved to the right-hand side of the original expression:

$$\frac{\partial \mathbf{U}}{\partial t} + \nabla \cdot \mathbf{F} = \nabla \cdot \mathbf{D}, \quad (3.1)$$

where \mathbf{U} is the vector of conserved quantities $(\rho, \rho\mathbf{u}, \rho E)$, \mathbf{F} contains the advective fluxes, and \mathbf{D} contains the diffusive terms. Note we have dropped the filter notation from the previous section for ease and simplicity of writing but again we are working with the filtered interpretation of the compressible Navier-Stokes Equations as derived in Equation (2.10).

In the finite volume formulation, the domain is sub-divided into N cells, each with volume V_i for cell i . In *PeleC*, these cells are given by boxes in Cartesian coordinates. We then integrate the system in Equation (3.1) over each finite volume to get the following:

$$\int_{V_i} \frac{\partial \mathbf{U}}{\partial t} dV + \int_{V_i} \nabla \cdot \mathbf{F} dV = \int_{V_i} \nabla \cdot \mathbf{D} dV. \quad (3.2)$$

In this formulation, a volume average of the state variables are considered through the following definition:

$$\mathbf{U}_i = \frac{1}{V_i} \int_{V_i} \mathbf{U} dV. \quad (3.3)$$

Applying the definition given by Equation (3.3) to Equation (3.2) along with the divergence theorem yields the following:

$$\frac{d\mathbf{U}_i}{dt} + \frac{1}{V_i} \int_{S_i} \mathbf{F} \cdot \mathbf{n} dS = \frac{1}{V_i} \int_{S_i} \mathbf{D} \cdot \mathbf{n} dS, \quad (3.4)$$

where S_i is the surface of cell V_i . To discretize further, the convective and diffusive fluxes must be approximated at the faces of each surface S_i in order to get the total flux contributions to the system:

$$\frac{d\mathbf{U}_i}{dt} + \frac{1}{V_i} \sum_j S_{i,j} \bar{\mathbf{F}}_{i,j} = \frac{1}{V_i} \sum_j S_{i,j} \bar{\mathbf{D}}_{i,j}, \quad (3.5)$$

where $S_{i,j}$ is the j -th edge of cell i , and corresponding subscripts on fluxes imply flux through that equivalent edge. Further methods may then be applied to perform the flux approximations needed and to discretize in time the system established in Equation (3.5).

PeleC leverages *AMReX* [111, 110, 41], a block-structured hierarchical adaptive mesh refinement library for meshing infrastructure, including grid refinement, distributed parallelism, geometry representation, and output [37]. Data management within *AMReX* is generally structured as follows: grids are represented by Boxes. Each Box is associated with a data container known as a FAB. A MultiFAB manages a collection of FABs, which store data at each AMR level [37]. Refinement ratios must be even and equally implemented in each direction. Figure 3.1 shows an example of this type of refinement hierarchy using a refinement ratio of two for three levels of mesh refinement.

Grid refinement is based on user-specified error criteria, those of which for this work are described in Chapter 4. For further details on *AMReX*, see [111].

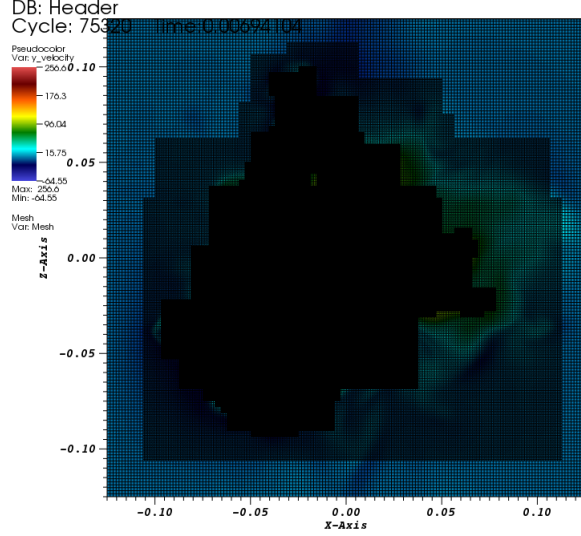


Figure 3.1: 2D slice of 3D data demonstrating mesh refinement using *AMReX*. The refinement ratio is 2 and there are 3 levels of mesh refinement.

3.3 Temporal Discretization: Spectral Deferred Correction Methods

Here we present the general idea behind SDC methods as is detailed in [66]. Consider an ordinary differential equation (ODE) of the following form:

$$\begin{aligned} \phi_t &= F(\phi(t), t), \quad t \in [t^n, t^{n+1}], \\ \phi(t^n) &= \phi^n, \end{aligned} \tag{3.6}$$

whose solution is given by the following integral expression:

$$\phi(t) = \phi^n + \int_{t^n}^t F(\phi)d\tau. \tag{3.7}$$

Then, given an approximation $\phi^{(k)}(t)$ to $\phi(t)$, one can define a residual as follows:

$$E(t, \phi^{(k)}) = \phi^n + \int_{t^n}^t F(\phi^{(k)})d\tau - \phi^{(k)}(t). \tag{3.8}$$

Defining the error to be $\delta^{(k)}(t) = \phi(t) - \phi^{(k)}(t)$, one can then get the error as follows:

$$\delta^{(k)}(t) = \int_{t^n}^t [F(\phi^{(k)} + \delta^{(k)}) - F(\phi^{(k)})] d\tau + E(t, \phi^{(k)}) \quad (3.9)$$

Now, one can use a higher-order quadrature rule to approximate the integral in Equation (3.8). Along with using a lower-order discretization for the integral in Equation (3.9), an iterative scheme can be constructed through which the order of accuracy can be improved over subsequent iterative steps, up to the order of accuracy set by the quadrature. This iteration is defined as $\phi^{(k+1)} = \phi^{(k)} + \delta^{(k)}$, and using Equations (3.8) and (3.9), we can write an update as follows:

$$\phi^{(k+1)}(t) = \phi^n + \int_{t^n}^t [F(\phi^{(k+1)}) - F(\phi^{(k)})] d\tau + \int_{t^n}^t F(\phi^{(k)}) d\tau \quad (3.10)$$

where again the first integral in Equation (3.10) is approximated with a low-order discretization and the second integral is approximated using higher-order quadrature.

In the multi-implicit spectral deferred correction (MISDC) formulation [66], F in Equation (3.6) can be broken up into individual processes:

$$F \equiv A(\phi) + D(\phi) \quad (3.11)$$

where $A(\phi)$ and $D(\phi)$ are advection and diffusion processes, respectively. We initialize both the diffusive and advective flux Courant-Friedrichs-Lowy (CFL) conditions with a value of 0.9 and then adapt as needed with the AMR. Note this decomposition now recovers the system formed through the finite volume formulation of Equation (3.5). This decomposition in general also includes a reaction term, but since our system is a single species with no reactions it is omitted here. These individual processes can now be treated separately. Discussion of flux treatment is given in the next section. For further details on discretizing Equation (3.10) with (3.11) and applying this to a system of ODEs as in (3.5), please see [65]. For the sake of this work, it is important to note that fluxes can be treated separately in a sort of operator splitting fashion and that accuracy can be set through the quadrature choice, which for the methods used here is second-order.

3.4 Spatial Discretization: Flux Calculations

Flux approximations are needed at cell faces, as outlined in Section 3.2. Following the methodology outlined in for the MISDC formulation, both advective and diffusive fluxes are centered in

time for part of the iterative process [66]. To get the advective fluxes, the PPM [19] is employed to approximate state values near cell faces where they are then extrapolated to $n + 1/2$. These values are then used in an approximate Riemann solver [20] to calculate the advective fluxes at cell faces at $n + 1/2$. The diffusive fluxes are discretized in space using center difference formulation, with time-centering for the iterator given by the midpoint rule [21, 62]. Here we detail the PPM a little further and highlight its advantages for this work.

3.4.1 Piecewise Parabolic Method

PeleC houses a few variations of the PPM, including the original formulation by Colella and Woodward [19]. The one used in this work is the “extrema preserving” variation of the PPM [21, 62] in order to aid in the handling of steep density gradients. Here we present the brief outline of the method in one dimension as is done in [63] in order to illustrate the general procedure.

First, the system in Equation (3.1) is recast in primitive form. In one dimension, this is:

$$\frac{\partial \mathbf{Q}}{\partial t} + \mathbf{A} \frac{\partial \mathbf{Q}}{\partial x} = \mathbf{S}_{\mathbf{Q}}. \quad (3.12)$$

where the vector \mathbf{Q} houses the primitive variables $(\rho, u, p, \rho e)$, A is the matrix given by $\partial \mathbf{F} / \partial \mathbf{Q}$, and $\mathbf{S}_{\mathbf{Q}}$ is the diffusive terms recast in primitive form. Internal energy is now carried in \mathbf{Q} to save on the number of calls made to the EoS during the Riemann solver.

The first step in interpolating primitive values to cell edges is to take the average cross-cell difference as follows:

$$\delta q_i = \frac{1}{2} (q_{i+1} - q_{i-1}). \quad (3.13)$$

Monotonicity is enforced with van Leer limiting [94], with limited values denoted δq_i^* . Using these limited values, primitive variables can then be interpolated to cell edges:

$$q_{i+1/2} = q_i + \frac{1}{2} (q_{i+1} - q_i) - \frac{1}{6} (\delta q_{i+1}^* - \delta q_i^*). \quad (3.14)$$

An additional constraint is imposed to ensure $q_{i+1/2}$ falls between adjacent cell averages.

Next, edge state values $q_{L,i+1/2}$ and $q_{R,i-1/2}$ can be set from $q_{i+1/2}$ and $q_{i-1/2}$, respectively. An additional flattening limiter that utilizes local pressure in its construction is applied here as well. Monotonicity is also enforced again, this time across $q_{L,i+1/2}$, q_i , and $q_{R,i-1/2}$ within a single cell.

Now, limited piecewise parabolic reconstruction can be achieved by computing average values swept out by parabolic profiles across each face, with the assumption that it moves at the speed of

a characteristic wave λ_k . These averages have the following form:

$$\begin{aligned}\mathcal{I}_+^{(k)}(q_i) &= \frac{1}{\sigma_k \Delta x} \int_{((i+1/2)-\sigma_k)\Delta x}^{(i+1/2)\Delta x} q_i^I(x) dx, \\ \mathcal{I}_-^{(k)}(q_i) &= \frac{1}{\sigma_k \Delta x} \int_{(i-1/2)\Delta x}^{((i-1/2)+\sigma_k)\Delta x} q_i^I(x) dx,\end{aligned}\quad (3.15)$$

with $\sigma_k = |\lambda_k| \Delta t / \Delta x$, where $\lambda_k = \{u - c, u, u, u + c\}$ and Δt and Δx are the discretization step size in time and space, respectively. With the parabolic profile $q_i^I(x)$ given by:

$$\begin{aligned}q_i^I(x) &= q_{R,i-1/2} + \xi(x) [q_{L,i+1/2} - q_{R,i-1/2} + q_{i,6} (1 - \xi(x))], \\ q_{i,6} &= 6q_i - 3 (q_{R,i-1/2} + q_{L,i+1/2}), \\ \xi(x) &= \frac{x - x_{i-1/2}}{\Delta x}, \quad x_{i-1/2} \leq x \leq x_{i+1/2},\end{aligned}\quad (3.16)$$

the integrals in Equation (3.15) can be explicitly written as follows:

$$\begin{aligned}\mathcal{I}_+^{(k)}(q_i) &= q_{L,i+1/2} - \frac{\sigma_k}{2} \left[q_{L,i+1/2} - q_{R,i-1/2} - \left(1 - \frac{2}{3}\sigma_k\right) q_{i,6} \right], \\ \mathcal{I}_-^{(k)}(q_i) &= q_{R,i-1/2} + \frac{\sigma_k}{2} \left[q_{L,i+1/2} - q_{R,i-1/2} + \left(1 - \frac{2}{3}\sigma_k\right) q_{i,6} \right].\end{aligned}\quad (3.17)$$

Finally, these averages can be used to perform a characteristic tracing to get the time-centered left and right edge states, $q_{L,i+1/2}^{n+1/2}$ and $q_{R,i-1/2}^{n+1/2}$. Full expressions for these edge states can be found in [63], along with the appropriate eigenvalue and eigenvectors needed for this procedure. With the edge states approximated, the advective fluxes can then be calculated via an approximate Riemann solver.

3.4.2 Approximate Riemann Solver

PeleC uses the approximate Riemann solver developed by Colella and Glaz [20]. This Riemann solver features two iterative scheme options for calculating the classical post-discontinuity state values \mathbf{u}^* and p^* : a Secant method and a Newton iteration. Full details for these implementations can be found in [20]. The key feature of this solver that is beneficial to this problem is the treatment of the EoS terms. Special consideration is given in formulation of this method to reduce the number of calls to the EoS within these iterative loops in order to make the method computationally tractable. This is of particular importance for cubic or higher-order EoS.

CHAPTER 4

SIMULATIONS

4.1 Computational Domain

4.1.1 AMR and Discretization

Our target simulation is a 3D LES with a grid size that is 100 times larger than the smallest scale of the turbulent flow. The smallest scale of these turbulent flows, known as the Kolmogorov scale [45], can be approximated as:

$$\eta = \left(\frac{\nu^3}{\varepsilon} \right)^{1/4}, \quad (4.1)$$

where $\nu = \mu/\rho$ is the kinematic viscosity and $\varepsilon = v_{in}^3/d$ approximates the average rate of dissipation of turbulent kinetic energy per unit mass, where v_{in} is the reference inflow velocity in the axial direction y and $d = 0.01$ cm is the jet diameter. For these turbulent jets, $\eta = 5.37 \times 10^{-6}$ cm. In our setup, the domain length in each direction is $x = 25d$, $y = 62.5d$, and $z = 25d$. To keep the calculation tractable and achieve an adequate LES grid size, we implement four levels of refinement, with a refinement ratio of 2, leading to 80, 200, and 80 cells on the coarsest level in the x , y , and z directions, respectively. This results in an initial mesh size of $\Delta x_0 = \Delta y_0 = \Delta z_0 = 0.3125$, leading to $\Delta x_3 = \Delta y_3 = \Delta z_3 = 3.9062 \times 10^{-4}$, where the subscript denotes the AMR level. The full four levels of refinement are implemented in a box around the inlet of lengths $x = z = 4d$ and $y = 2d$ to ensure high refinement at the inflow. These four levels are then adaptively refined based on the given refinement criterion in the region outward from the jet inlet up to a distance of $20d$ in the x and z direction and $60d$ in the y direction, as can be seen in Figure 4.1. The refinement criterion is given by the vorticity, specifically with $\omega \geq 5000^{2l}$, where ω is the magnitude of the vorticity and l is the AMR level. For the first ten flow throughs of the simulation, mesh refinement only occurs up to one level within the refinement region to establish the flow pattern. Thereafter, the simulation proceeds with the four levels of mesh refinement for ten more flow-throughs. After that, statistics are collected over the next two flow-throughs for analysis, where a steady state is assumed to have been reached.

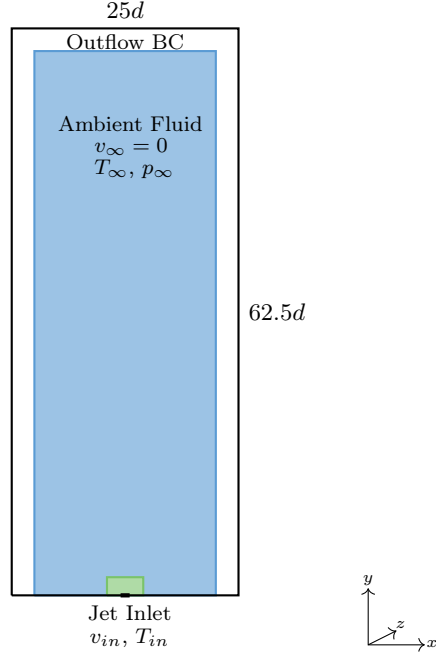


Figure 4.1: Two dimensional slice schematic of jet setup. Four levels of refinement are enforced within the green box based on proximity to jet inlet. Refinement based on vorticity criterion then occurs within the blue region. Outside the blue region, AMR is explicitly turned off to allow flow structures to be dissipated numerically and allowed to leave the domain without incurring spurious reflections.

4.1.2 Initial and Boundary Conditions

Our inlet consists of an opening centered in the xz -plane with diameter $d = 0.01\text{ cm}$ through which the sCO₂ jet is initialized. The pressure in the jet at the inlet is the same as that of the quiescent background fluid and it is given by $p_{in} = p_{\infty} = 1.01325 \times 10^8 \text{ Bayre}$. The ambient fluid remains at rest while the jet is initialized with an inflow velocity of $v_{ref} = 1800 \text{ cm s}^{-1}$, leading to a Reynolds number of the initialized jet of $Re_{ref} = 22910$, with v_{ref} and d being the reference velocity and length scale respectively. For the jet temperature and pressure conditions given, the inflow density is $\rho_{in} = 3.019 \times 10^{-1} \text{ g cm}^{-3}$, as calculated via the SRK EoS in *PeleC*. To implement a turbulent inflow, we formulate our mean velocity and root mean square (rms) values by scaling, interpolating, and adding noise to a predetermined velocity profile calculated via DNS [27], with jet diameter D , axial velocity v_{DNS} , and rms values given by $v'_{DNS} = \langle v_{DNS}^2 \rangle^{1/2}$. For DNS quantities, (u, v, w) values are in the (r, v, θ) direction. Finalized values are converted to Cartesian values for the simulation. We begin by scaling the DNS values with our reference jet velocity and length

values:

$$r_{\text{DNS, scaled}} = d \cdot \left(\frac{r}{D} \right)_{\text{DNS}}, \quad (4.2a)$$

$$v_{\text{DNS, scaled}} = v_{\text{ref}} \cdot v_{\text{DNS}}, \quad (4.2b)$$

$$v'_{\text{DNS, scaled}} = v_{\text{ref}} \cdot v'_{\text{DNS}}, \quad (4.2c)$$

$$u'_{\text{DNS, scaled}} = v_{\text{ref}} \cdot u'_{\text{DNS}}, \quad (4.2d)$$

$$w'_{\text{DNS, scaled}} = v_{\text{ref}} \cdot w'_{\text{DNS}}. \quad (4.2e)$$

These values are then linearly interpolated onto our grid values $r(i)$ with $f_1 = \frac{r(i) - r_{\text{DNS, scaled}}(i)}{r_{\text{DNS, scaled}}(i+1) - r_{\text{DNS, scaled}}(i)}$, $f_2 = \frac{r(i) - r_{\text{DNS, scaled}}(i+1)}{r_{\text{DNS, scaled}}(i) - r_{\text{DNS, scaled}}(i+1)}$, and $\phi_{\text{DNS, inter}} = f_1 \phi(i) + f_2 \phi(i+1)$, where ϕ is each of the velocity components mentioned in Equations (4.2). Finally, noise is added to each cylindrical component of the velocity as follows before conversion back to Cartesian coordinates for use in the boundary inflow:

$$v_{in, cyl} = \langle v_{\text{DNS, inter}} \rangle + (v'_{\text{DNS, inter}} + \beta v'_{\text{DNS, inter}} \psi_1 \sin \theta_1) \cdot \psi_2 \sin \theta_2, \quad (4.3a)$$

$$u_{in, cyl} = u'_{\text{DNS, inter}} + \beta u'_{\text{DNS, inter}} \psi_3 \sin \theta_3, \quad (4.3b)$$

$$w_{in, cyl} = w'_{\text{DNS, inter}} + \beta w'_{\text{DNS, inter}} \psi_4 \sin \theta_4, \quad (4.3c)$$

where $\beta = 0.1$ and each ψ_i and θ_k value is randomly generated as follows:

$$r_i = \sqrt{-2.0 \log(X_i)}, \quad (4.4a)$$

$$\theta_k = 2\pi X_k, \quad (4.4b)$$

where X_n are random uniformly distributed numbers between 0 and 1. The inflow parameters are finalized as ϕ_{in} after being converted to Cartesian coordinates $(r, y, \theta) \rightarrow (x, y, z)$.

We implement zero gradient boundary conditions for all boundaries not involving the jet inflow with first order extrapolations. Additionally, AMR is halted at a distance of $2.5d$ from the boundary in the x and z directions, and that of $5d$ in the axial direction. This low refinement perimeter is implemented to act in a similar fashion to a sponge with the goal of dissipating waves and thus reducing the chance of spurious reflections from the boundaries.

4.2 Case Descriptions

Three cases are investigated in this study. The first case pertains to an isothermal jet, in which the jet conditions match that of the ambient fluid for all quantities aside from velocity. The other

two cases consider non-isothermal jets, in which the ambient fluid is adjusted to no longer match the temperature of the jet inflow. All three cases consider the same inflow conditions, while ambient fluid conditions are what varies between them. Temperatures for the ambient fluid in the non-isothermal cases are chosen such that the ambient fluid is supercritical but the temperature for each case falls on either side of the peak in specific heat seen near the critical point. This peak is associated with the pseudo-boiling phenomenon seen in supercritical fluids, where upon crossing the Widom line, the supercritical fluid experiences a shift from being more gas-like to more liquid-like in nature, although distinct phase separation between the two is not present. A summary of the conditions for each case can be seen in Table 4.1.

Table 4.1: Summary of jet parameters for each case.

Parameter	Case 1	Case 2	Case 3
T_∞ (K)	330	350	314
T_{in} (K)	330	330	330
p_∞ (Bayre)	1.01325×10^8	1.01325×10^8	1.01325×10^8
p_{in} (Bayre)	1.01325×10^8	1.01325×10^8	1.01325×10^8
ρ_∞ (g/cm ³)	3.0192×10^{-1}	2.2567×10^{-1}	5.1274×10^{-1}
ρ_{in} (g/cm ³)	3.0192×10^{-1}	3.0192×10^{-1}	3.0192×10^{-1}
$c_{p\infty}$ (Erg/g*K)	3.389×10^7	1.927×10^7	5.703×10^7
c_{pin} (Erg/g*K)	3.389×10^7	3.389×10^7	3.389×10^7
$C_{s\infty}$ (cm/s)	2.593×10^4	2.661×10^4	3.131×10^4
C_{sin} (cm/s)	2.593×10^4	2.593×10^4	2.593×10^4
μ_∞ (P)	2.748×10^{-4}	2.445×10^{-4}	4.110×10^{-4}
μ_{in} (P)	2.748×10^{-4}	2.748×10^{-4}	2.748×10^{-4}
λ_∞ (Erg/(cm*s*K))	3.966×10^3	3.443×10^3	6.361×10^3
λ_{in} (Erg/(cm*s*K))	3.966×10^3	3.966×10^3	3.966×10^3
Z_∞	5.329×10^{-1}	6.691×10^{-1}	3.331×10^{-1}
Z_{in}	5.329×10^{-1}	5.329×10^{-1}	5.329×10^{-1}
v_{ref} (cm/s)	1800	1800	1800
R_{ref}	22911	22911	22911
M_{ref}	0.08	0.08	0.08

The goal in choosing the ambient temperature in this way is to investigate the impact of large thermodynamic changes on the flow field of the supercritical jet. An example of this can be seen with the sharp peak in constant pressure specific heat in Figure 4.2. This choice differs from similar studies, which typically involve transcritical injection.

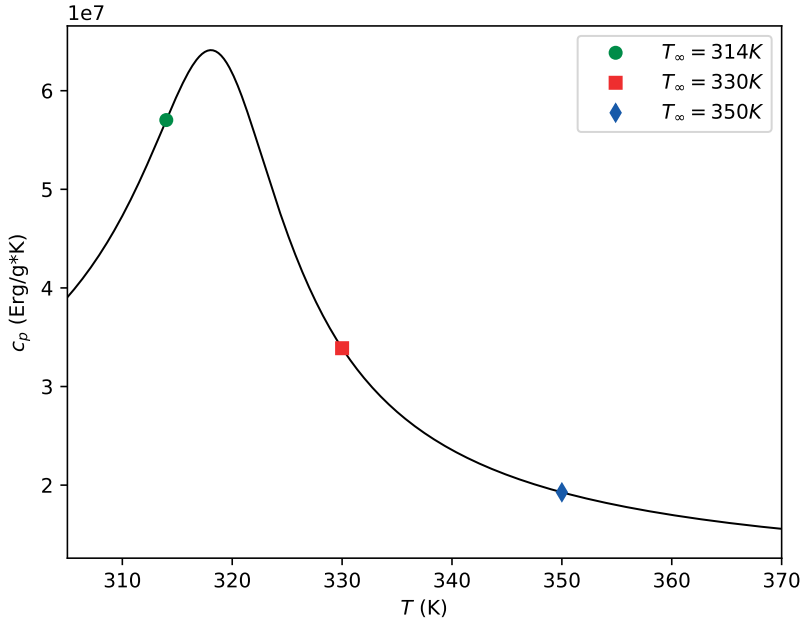


Figure 4.2: Extreme thermodynamic variation seen near critical point with ambient temperatures plotted for reference to see regime coverage of each case. Red is the jet temperature for all cases and isothermal temperature for the ambient case. Blue is the 350K ambient case. Green is the 314K ambient case.

4.3 Compute Time and Hardware Specifications

Simulations were run on the National Renewable Energy Laboratory (NREL) Eagle supercomputer using the Intel suite of compilers. Simulations utilized 576 MPI ranks in total, with 36 ranks spread across 16 nodes. Roughly 17,000 cells were handled per MPI rank. Dynamic load balancing of AMR levels allowed for maximum utilization of the system. In total, over 100 TB of data were stored from the original 3D simulations run over the course of the 10 flow-throughs of the domain needed for averaging procedures. To help manage data storage issues, slicing procedures were implemented to reduce full 3D simulation data down to 2D slice data, where averaging procedures were then performed as outlined in the next section.

4.4 Post-Processing Procedures

Post-processing procedures were written in Python and primarily leveraged the following libraries: yt, pandas, numpy, and, matplotlib. Original 3D data at each plotfile was sliced in three

different ways using yt: along the centerline to create 1D data, normal to the jet axis at various points down stream to create 2D data, and along the axial direction at $z = 0$ to create 2D data.

For time averaging, a basic discrete averaging procedure was implemented over i saved plot files from the final 2 flow-throughs of the simulation, with 100 plots saved per flow-through:

$$\phi_{avg, slice} = \frac{1}{200} \sum_{i=1}^{200} \phi_{i, slice}. \quad (4.5)$$

For each slice normal to the jet axis, radial averages are approximated with $r = 0$ lying in the center of the xz -plane with $r = \sqrt{x^2 + z^2}$. The N points nearest to each fixed r distance away from the center were then averaged together:

$$\phi_{avg, r} = \frac{1}{N} \sum_{k=1}^N \phi_{k, r}. \quad (4.6)$$

For quantities that were averaged both temporally and radially, temporal averaging was performed first, with the radial average then taken of the time averaged slice data. Fluctuating quantities are calculated on 2D slices via the formulation in Equation (1.12), with Equation (4.6) serving as the approximation for the Reynolds average:

$$\phi'_{i, slice} = \phi_{avg, slice} - \phi_{i, slice}. \quad (4.7)$$

These perturbations can then be used to calculate average resolved Reynolds stresses for each u_i component of velocity, $\langle u'_i u'_j \rangle$, and turbulent kinetic energy (TKE) components [14] as follows:

$$\langle TKE \rangle = \frac{1}{2} (\langle u' u' \rangle + \langle v' v' \rangle + \langle w' w' \rangle). \quad (4.8)$$

In Chapter 5, when these quantities are introduced, they are presented without angle brackets for the sake of streamlining bulky notation, but note that all of the results presented from here on are averaged either temporally or temporally and radially as was presented in this section, unless explicitly stated otherwise.

4.5 Challenges and Lessons Learned

Early challenges in this project were related to the inflow and outflow boundary conditions. We initially compared a few different jet inflow strategies, namely one involving parabolic pipe flow, a DNS interpolation scheme with added synthetic perturbation [13], and a hyperbolic tangent profile with the same added synthetic perturbation. The interpolation scheme was ultimately selected as

it was based on a realistic, pre-developed turbulent pipe flow [27] as opposed to being modeled as in the other two cases. This inflow also achieved a fully developed turbulent flow faster than the other two again due to the fact that it was initialized from a pre-developed turbulent flow. Outflow boundary conditions were more complicated. Initially, no AMR cutoff was implemented at the boundary. After many test runs of varying length (some taking as long as 3 days) where Navier-Stokes Characteristic Boundary Conditions (NSCBC) were implemented [74] with various mesh sizes, we were still getting non-negligible back flow at the outlet of the domain due to remaining high vorticity levels. Comparisons of mesh size effect on the outflow back flow then led to the buffer zone implementation idea. Various buffer sizes were tested to ensure adequate damping of any spurious outflow feedback. This process alone was a considerable portion of the ten week internship that started this project, before any LES were even performed. To summarize, during this time, I directly contributed to and tested a variety of Fortran-based inflow and outflow boundary conditions. This process is what led to the boundary condition choices outlined in the above section.

It then took an additional semester's worth of time to troubleshoot LES-related issues involving SGS models, remote access to NREL's Eagle supercomputer, and memory issues. Tests were run to see how distribution of cores per node affected memory, with runs done using 16 cores distributed evenly across 1, 2, and 4 nodes. More nodes also meant longer queue times in the Slurm workload manager, so number of nodes selected ultimately had to strike a balance between best memory distribution for job wait time and execution. It is hard to say exactly how long in total the three simulations took. An error in the root finding routine for the EoS initially slowed things down for a few months (note: simulations were not continually running during this three month period). After that was corrected, but before switching to the Intel suite of compilers, as of March 29, 2020, the three cases were at the following status: the $330K$ ambient case still needed 176 hours to reach the final target time for 10 flow throughs, while the $350K$ and $314K$ ambient cases needed approximately 696 hours and 3,896 hours, respectively. Though introduced very late into the runs, the Intel suite of compilers did greatly reduce the amount of time left to complete the simulations.

Post-processing issues relating to slicing posed a major challenge. Upon initial slicing of the 3D data for visualization and averaging, we observed vast portions of data missing, as can be seen in Figure 4.3. These missing data chunks affected slices randomly and did not always correspond to the same AMR level, making the issue difficult to diagnose. Slicing using *VisIt* revealed the data to be intact, leading to the conclusion that the issue was in our in-house Python slicing script. After including this issue in my SIAM CSE 2021 presentation, we were able to collaborate with

members of the Center for Computational Sciences and Engineering (CCSE) group at Lawrence Berkeley National Laboratory. Through this interaction, Andrew Myers of CCSE found a floating point precision bug in yt that was causing the slicing issue. Through this collaboration, yt was improved and we were able to continue with our slicing and data acquisition.

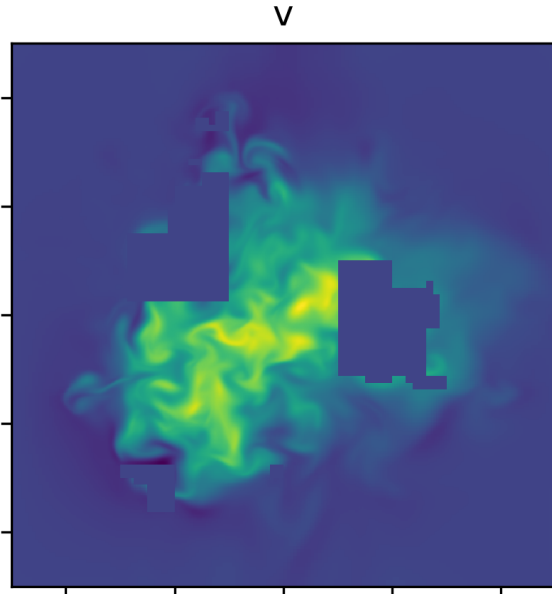


Figure 4.3: An example of the yt slicing issue caused by a floating point precision error. The image contains a slice normal to the flow axis depicting the axial velocity component with patches of data missing.

Data storage and transfer issues also created a few hurdles that required strategic thinking to overcome. As mentioned earlier, the three cases in total ended up using over 100 terabytes (TB) of storage on NREL’s Eagle. Before data analysis could be completed, the project folder housing the data expired, resulting in the need to either move the full 100 TB of data elsewhere or downscale and move what was feasible within the two week window remaining before deletion. We ultimately decided on deleting all but one of the full plot files from each of the flow-throughs. A checkpoint file was also saved for each flow-through. Slices were then made for the last 200 plot files before being moved to a local hard drive via the Globus file transfer system. These slices only contained vital state data, such as density, temperature, pressure, velocity, etc., to optimize space, leaving secondary data that could be re-calculated from the saved quantities using the system models (like viscosity or internal energy, for example). Slice files were saved in compressed numpy format (.npz)

to further optimize storage. This process reduced the data down to under 4 TB, which was much easier to manage.

An unexpected issue then arose when trying to re-compute derived quantities for further analysis. Transport and thermodynamic models are written in C++ within *PelePhysics*, while the state data of the slices was saved with Python formatting. In order to try to reuse the functions in *PelePhysics*, we explored strategies to convert Python to C++ arrays. This tactic proved unsuccessful. Instead, I wrote a Python script that combined the necessary *PelePhysics* functions and CO₂ transport and thermodynamic properties to recalculate the additional quantities of interest needed for flow analysis. This script can be easily modified for other fluids of interest and provides an avenue for data management in the future.

4.6 Contributions Made to *PelePhysics*

For direct use in this simulation, I helped create the pure CO₂ model folder containing all of the appropriate thermodynamic, transport, and chemical information in the CHEMKIN file format [42]. Tangentially related to this project, I also heavily contributed to the the implementation of quasi-steady state assumptions (QSSA) within *PelePhysics*. The Python library I helped create takes user specified QSS species for a given compound model and determines the reactions and related species that are needed to formulate the simplified algebraic expressions needed to update these species within the simulation. This process utilizes Tarjan's Strongly Connected Component algorithm [93] to formulate a species-species and species-reaction network for determining reaction dependencies. Although the simulations in this project specifically don't contain reacting terms, this QSSA implementation can be used for future work involving sCO₂ applications in direct-firing power systems. Since chemistry is typically the stiffest, and consequently most expensive, component of reacting flow simulations, implementing QSSA into *PelePhysics* has the potential to greatly reduce system run time and computational cost. A paper is currently in preparation regarding this QSSA implementation within *PelePhysics*.

CHAPTER 5

RESULTS

Here, we present the results of the three cases outlined in Chapter 4. In addition to visualizing qualitative visuals of jet slices along the axial direction, a variety of quantities of interest are analyzed. Quantities of interest we consider include axial velocity decay (in both the radial and axial directions), centerline velocity decay, resolved Reynolds stresses, and resolved TKE, among others. These quantities are commonly explored in turbulent jet investigations and have been chosen to highlight the differences in flow field structure between our three cases. In the graphs presented throughout this chapter, all quantities are averaged over time unless specifically denoted otherwise. Additionally, for graphs plotted in the radial direction away from the centerline, quantities are radially-averaged.

These results are organized as follows: first, the isothermal jet case is presented and quantities of interest are related to those of comparable subcritical turbulent jets studies from relevant literature [107, 35, 14]. This establishes a baseline for comparison with the non-isothermal jet cases and is used to validate that the numerical jet setup is behaving in a reasonable manner. The two non-isothermal cases are then presented together, with the $350K$ ambient case compared against the isothermal case. Variations between these two cases are related to similar non-isothermal turbulent jets from the subcritical regime. Our main case of interest is the $314K$ ambient case as it contains the transition over the pseudo-boiling point. We then compare this case with the $350K$ ambient case, which is additionally related to similar supercritical investigations regarding the work of Mayer et al., where transcritical injection involves a phase change [60]. Through the comparisons of our $314K$ cases, we specifically investigate the impact of the transition through the pseudo-boiling point on the supercritical flow field.

5.1 Isothermal Jet

Our first case involves the isothermal jet where both jet and ambient fluid are at $330K$. Quantities of interest for this case are compared against an incompressible round turbulent jet [76] and

apt compressible jet cases from literature [107, 35, 14]. This case serves as a baseline for comparison with the other two cases involving non-isothermal jets.

5.1.1 Flow Field Features

All images here depict a 2D slice of the 3D flow field at $z = 0$. Each figure contains an instantaneous snapshot and a time-averaged snapshot of the entire slice domain, plus an additional zoomed-in image of the time-averaged quantity of interest near the inlet. All instantaneous images are taken from the final data point of the simulation.

Figure 5.1 shows the axial velocity component of the flow field. The general spreading rate and decay of the velocity field can be seen from the instantaneous snapshot in Figure 5.1a. From these images, the flow field can be distinguished into three main regions, as noted in [35]: the potential core region, the transition region, and the fully developed region. The flow is laminar up until about $y/d = 2$ before perturbations begin. The stream mostly stays together through these initial perturbations up until $y/d = 7$ where spreading then begins, marking the end of the potential core. The averaged axial velocity fields in Figures 5.1b and 5.1c shed more light on the development of the jet. The transition region occurs approximately from $7 \leq y/d \leq 15$, where the laminar state evolves into the turbulent state as flow structures begin to interact with one another. Thereafter the jet appears fully developed and nonlinear interactions give way to eddies across a range of large and small scales. Centerline analysis of the turbulent kinetic energy later on will provide more information for these boundaries.

Figure 5.2 shows minor pressure fluctuations in the flow, scaled against the maximum pressure achieved above the ambient pressure. Figure 5.2a shows minor pressure oscillations mirrored on each side of the jet edge in the same zone as the initial velocity fluctuations see in Figure 5.1a. Thereafter, the oscillations become asymmetric, correlating to the beginning of the jet disintegration as seen in the velocity field. Pressure fluctuations are concentrated near the inlet and decrease in amplitude past the transition zone. This can be seen more clearly in Figure 5.2b. On average, pressure fluctuations yield a minor increase within the potential core and decrease on the jet perimeter, as can be seen in Figure 5.2c. Fluctuations also lead to a minor pressure drop on average in the transition region.

Figure 5.3 shows the magnitude of the vorticity scaled between the maximal and minimal values. Figure 5.3a shows the strongest vorticity occurring at the jet interface with the ambient fluid near the inlet. Past this initial stage, a Kelvin-Helmholtz instability causes a rollup at the outer edge

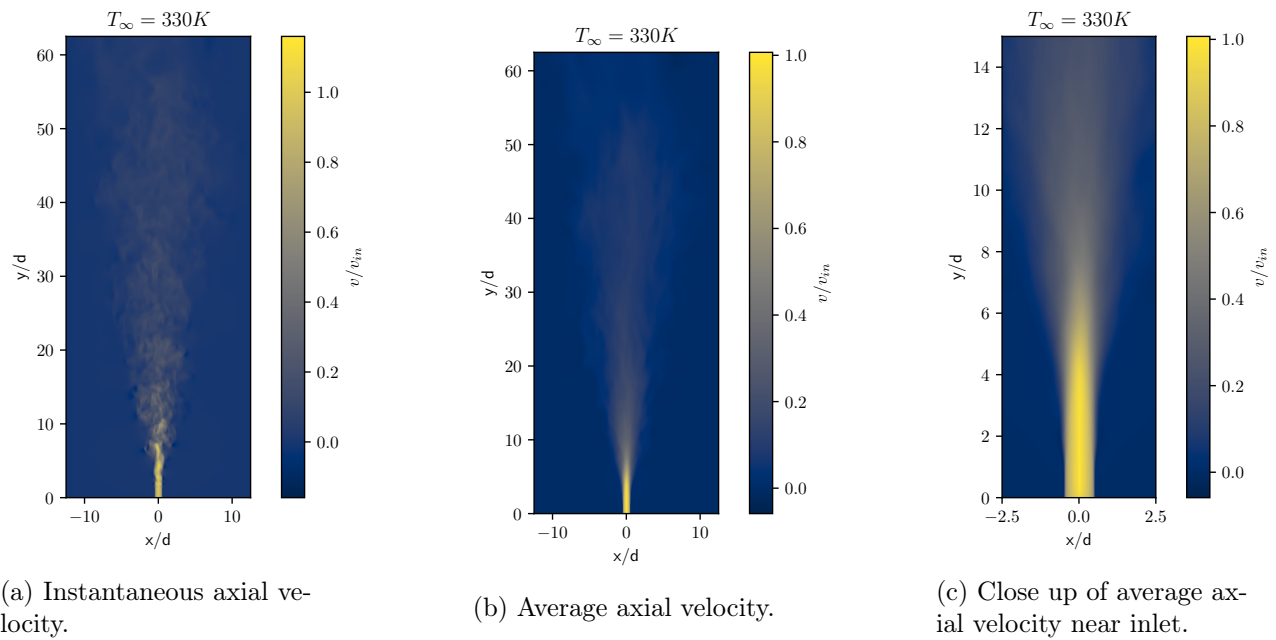


Figure 5.1: Axial velocity features of the isothermal jet.

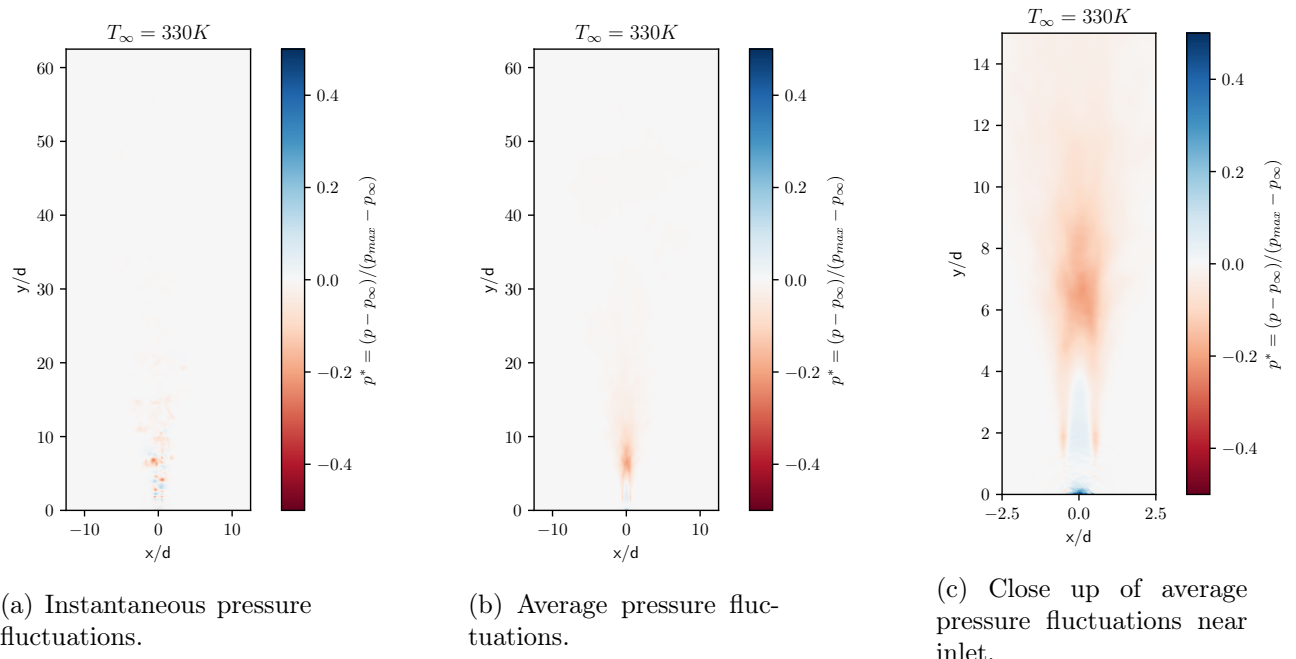


Figure 5.2: Pressure features of the isothermal jet.

of the jet around $y/d = 2$, forming small but coherent vortical structures. These structures then become unstable and lead to more complex vortices beginning around $y/d = 5$. The averages in Figures 5.3b and 5.3c both show again that the most intense vorticity occurs at the inlet along the outer edge of the jet. This high intensity remains constant until about $y/d = 1$ before more mixing with the ambient fluid occurs as the jet spreads and the vorticity lessens in intensity. Vortices are still restricted to the jet edge until around $y/d = 5$ where the transition to fully developed turbulence enables vortical motions to extend across the fully spread of the jet. Generally, vorticity then dissipates as the jet spreads farther downstream.

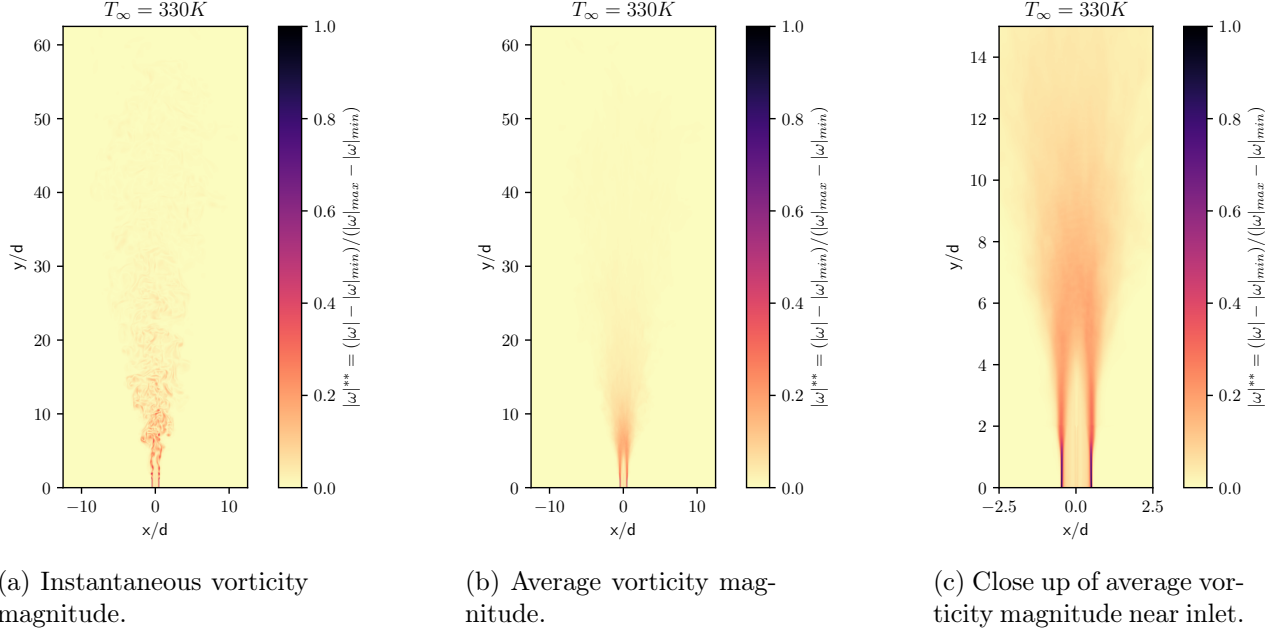


Figure 5.3: Vorticity magnitude features of the isothermal jet.

5.1.2 Mean Flow Properties

Figure 5.4 depicts the time and radially averaged scaled axial velocity component plotted against radial distance from the centerline at multiple normal slices downstream from the inlet. The velocity is scaled by the average axially velocity value at the inflow while the radial direction is scaled by the jet diameter. These plots demonstrate the axial velocity decay as the flow progresses farther downstream. As the velocity value along the centerline decreases, the half-mean half-width (HMHW) increases, both flattening and widening the velocity profile. Typically, for the round turbulent jet, this expansion would occur in such a way that upon specially selected scaling, these profiles would

collapse into one profile after a certain point. This potential is explored farther in the next figure. This decay is a common feature of how the axial velocity of the jet develops as it leaves the inlet [76].

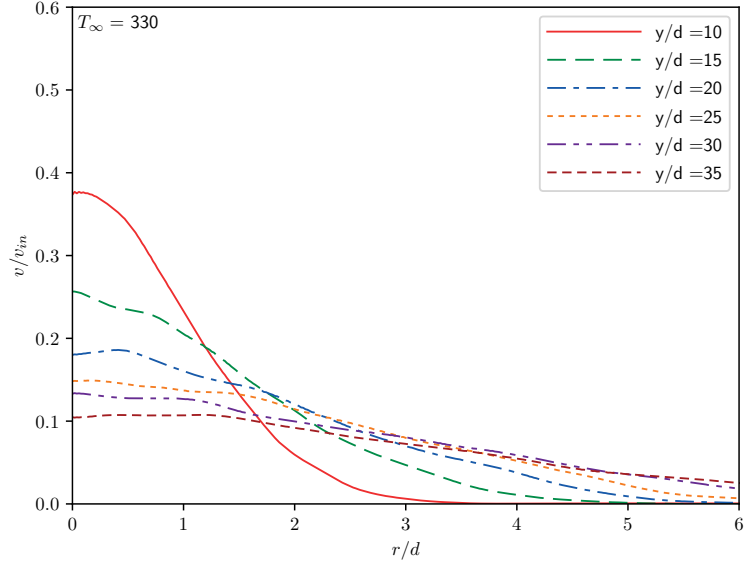


Figure 5.4: Average (both in time and radially) axial velocity scaled by inlet value plotted along radial distance from centerline. Profile decay follows similar trajectory to what is expected in incompressible round jet theory [76].

Figure 5.5 depicts time and radially averaged scaled axial velocity components plotted against the radial distance from the centerline. Each curve is made at a slice normal to the axial flow direction at different points downstream. Figure 5.5a depicts velocity curves every $3d$ downstream from the inlet near where the transition region begins while Figure 5.5b contains plots taken every $5d$. The axial velocity is scaled by the centerline value v_c while the radial distance is scaled by the HMW, where the velocity component is equal to half the value on the centerline $v(r_{1/2}) = v_c/2$.

Figure 5.5a shows axial velocity profiles in the transition region of the jet. They exhibit self-similarity collapse into one profile which, is a common feature of round turbulent jets [76, 107, 14]. farther downstream as depicted in Figure 5.5b, self-similarity is fairly well maintained with minor fluctuations in the center and edge of the jet. These fluctuations are most likely the result of low resolution in the time averaging of available data. Overall though, this general collapse is

in agreement to that which is seen in comparable low Mach isothermal round jet simulations and experiments, as are summarized in [107].

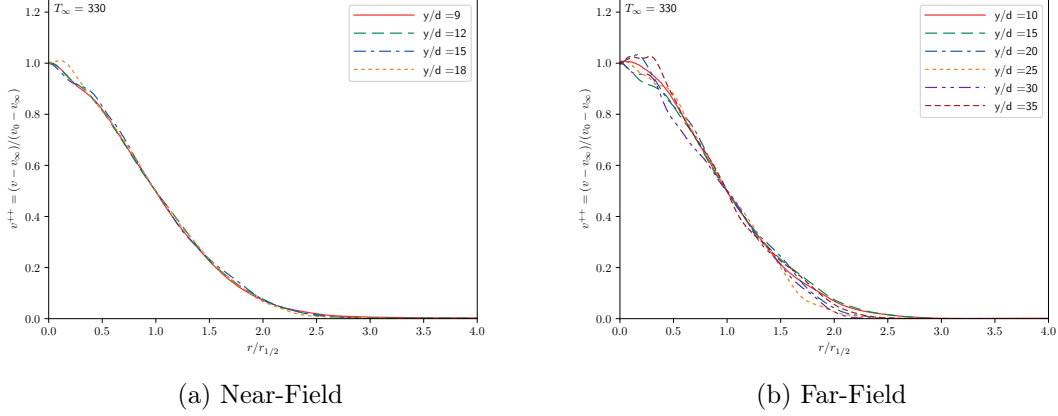


Figure 5.5: Normal slices of scaled axial velocity, averaged in both time and the radial direction, plotted in the radial direction scaled by $r_{1/2}$. Both near- and far-field regions demonstrate the self-similarity within the round turbulent jet.

Another common feature of round turbulent jets is the development of a linear relationship between the jet centerline value and the distance downstream. This comparison for the transition region of the jet is depicted in Figure 5.6. Here, the centerline value of the axial velocity v_0 is inversely linearly proportional to the distance downstream. The decay rate can be characterized by the following relationship [107]:

$$\frac{v_{in}}{v_0} = \frac{1}{B_v} \left[\frac{y}{d} - \frac{y_0}{d} \right], \quad (5.1)$$

where y_0 is the virtual origin of the jet [76] and B_v is the decay rate. For this case, the decay rate is given by $B_v = 3.69$. The decay rate here is smaller than those of comparable low Mach jets in the subcritical regime, as summarized in [35].

The spreading rate of the jet can also be characterized by linear development downstream in a similar fashion [35]:

$$\frac{r_{1/2}}{d} = C_v \left[\frac{y}{d} - \frac{y_0}{d} \right], \quad (5.2)$$

where C_v is the spreading rate of the jet. The spreading rate here is given by $C_v = 0.122$. The spreading rate here is larger than those of comparable low Mach jets in the subcritical regime, as summarized in [35].

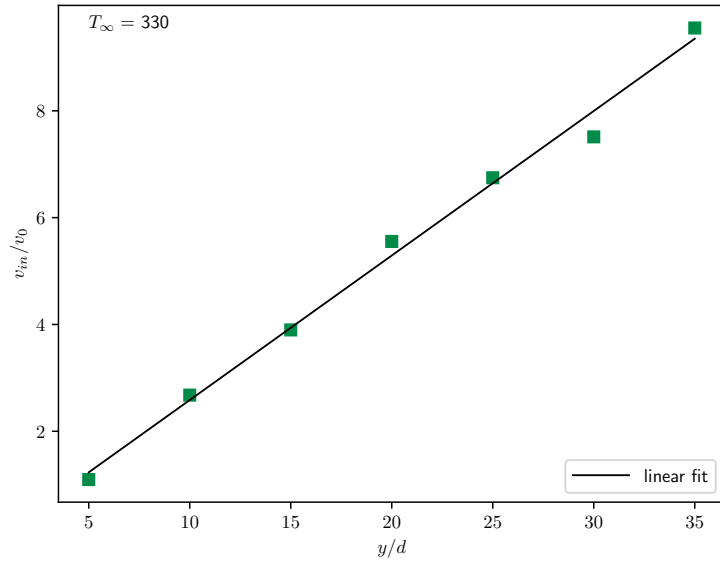


Figure 5.6: Axial inlet velocity scaled by centerline values along the axial direction. When the distance downstream is scaled by the jet diameter, linear decay of the centerline axial velocity is observed.

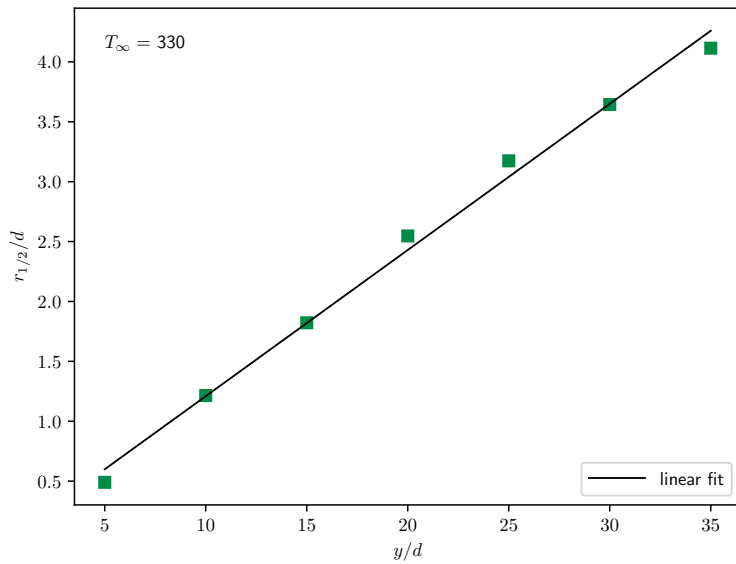


Figure 5.7: HMLW of axial velocity along the axial direction. When the distance downstream is scaled by the jet diameter, linear growth of the axial velocity HMLW is observed.

5.1.3 Turbulence Dynamics

Figure 5.8 shows the time and radially averaged resolved Reynolds stresses at two points downstream from the inlet. Here, velocity components (u, v, w) correspond to the (r, y, θ) directions, respectively. Each Reynolds stress component follows general trends associated with round turbulent jets [76, 35], with the axial component providing the leading contribution, followed by the other two directional components closely with these two being of roughly the same magnitude, and the cross-directional component contributing the least. Centerline values are slightly higher than the typical values seen in other works as is summarized in [35], but are of the same order of magnitude. This discrepancy could be due to error induced by the SGS model accuracy for second order moments as noted in [64]. Note also that self-similarity is not exhibited, as each component exhibits an increase in magnitude at the center of the jet as distance downstream is increased.

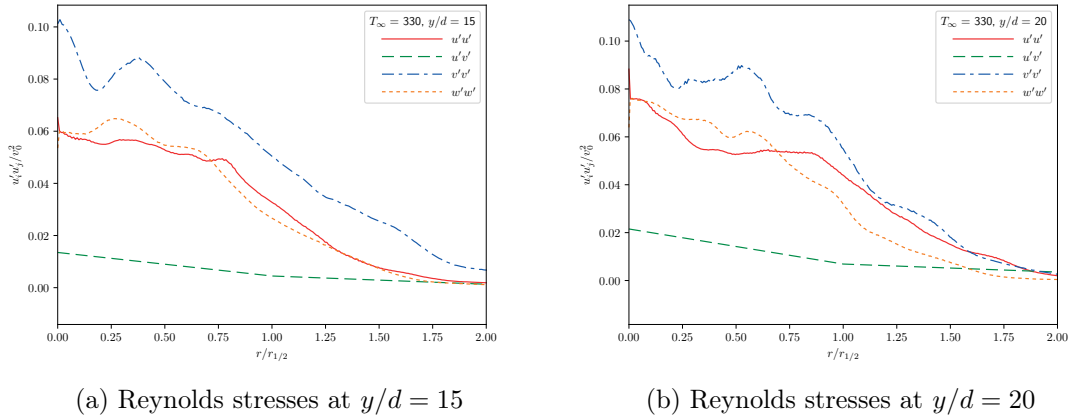


Figure 5.8: Time and radially averaged Reynolds stresses for the isothermal jet at two locations downstream. Both slices follow similar Reynolds stress relations seen in incompressible round jet [76].

Figure 5.9 shows the time average turbulent kinetic energy components along the centerline of the jet. Each component grows through the potential core region of the jet up until all components reach a peak in energy around $y/d = 6$, with the axial component's peak coming slightly before the other two directions. Rapid decay is then observed up until around $y/d = 15$ before a slower decay sets in up until a leveling off is achieved around $y/d = 30$. This rapid decay and then farther progression correspond to the transition and fully developed jet regions, respectively. Compared

to similar TKE analysis regarding compressible turbulent jet flows, this case displays anisotropic separation more akin to higher mach flows [14].

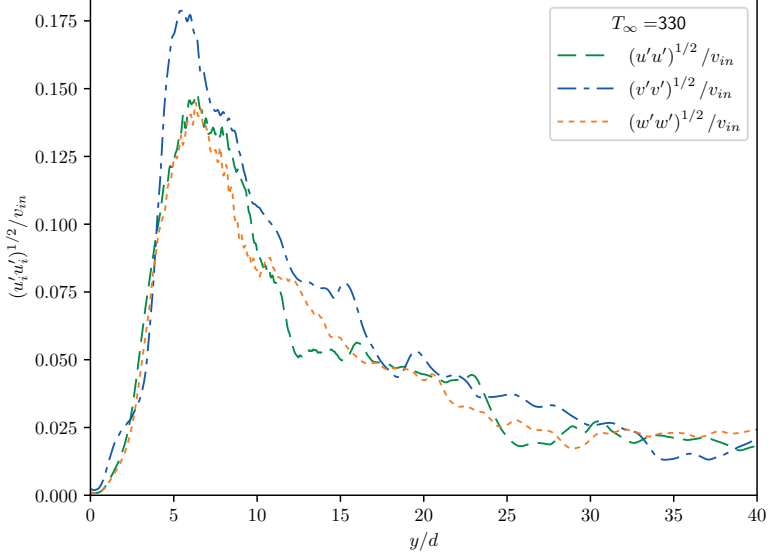


Figure 5.9: Average resolved turbulent kinetic energy components along centerline. Note: averaging as described in Chapter 4 occurs prior to square rooting in the given quantity description.

5.1.4 Discussion

Overall, the isothermal sCO₂ jet appears to behave in a similar fashion to low Mach compressible and incompressible jets within similar parameter regimes [107, 35, 14, 76]. Qualitative features such as discernible regions of development and self-similarity are in agreement with ranges provided in the literature for subcritical jets. Decay rate and spreading rate are slightly below and above the typical ranges seen for similar subcritical cases, respectively. The supercritical isothermal jet appears to persist and spread more than its subcritical comparable counterpart, at least in the transition region. Resolved TKE components also exhibit slight anisotropy between the axial and span-wise components.

5.2 Non-Isothermal Jets

The two non-isothermal jet cases as described in Chapter 4 are presented here. Some features are compared to the isothermal jet case while others are used for direct comparison between the

two non-isothermal cases. Again, the $350K$ ambient case depicts a cooler jet entering a warmer ambient fluid, moving farther away from the supercritical point while the $314K$ ambient case depicts a warmer jet entering a cooler ambient fluid with a transition over the pseudo-boiling point. It is anticipated that the $314K$ ambient case will vary much more prominently from the other two cases across various quantities of interest examined.

5.2.1 Flow Field Features

Figure 5.10 shows various axial velocity field comparisons between the isothermal and non-isothermal jets. The instantaneous axial velocity over the whole domain is depicted in Figure 5.10a. The $350K$ ambient case has a laminar flow region of similar length to the $330K$ ambient case, with the jet core staying laminar up until $y/d = 2$ before fluctuations begin to take effect. The developing region after this within $7 \leq y/d \leq 15$ appears to be slightly more volatile in the $350K$ ambient case compared to the $330K$ ambient case, with the region containing finer-scale fluctuations. The spreading rate of the $350K$ ambient case is smaller than that of the base case while overall intensity levels seem to be comparable in the downstream direction. The $314K$ ambient case has a much shorter laminar region compared to the base case, with fluctuations beginning to become apparent as early as $y/d = 1$. Perturbations after that appear to be more symmetric in structure, with vortices along the jet edge staying in tandem instead of the asymmetric shedding apparent in the other two cases. The $314K$ ambient case also appears to have a spreading rate comparable to the $350K$ ambient case, but with a faster decay in intensity in the downstream direction. Figure 5.10b helps further illuminate the difference in spread of the three jets. Here the $350K$ ambient core intensity is more persistent downstream with a more distinct and thinner outer edge flow present than in the $330K$ ambient case, while the $314K$ case has a lower intensity central flow region but a comparably sized edge flow region compared to the $330K$ ambient case. Finally, Figure 5.10c depicts the potential core and transition regions of the three cases more clearly. Here, the similarity between the potential cores of the $330K$ and $350K$ ambient cases is clear while the $314K$ ambient case has a much shorter core length.

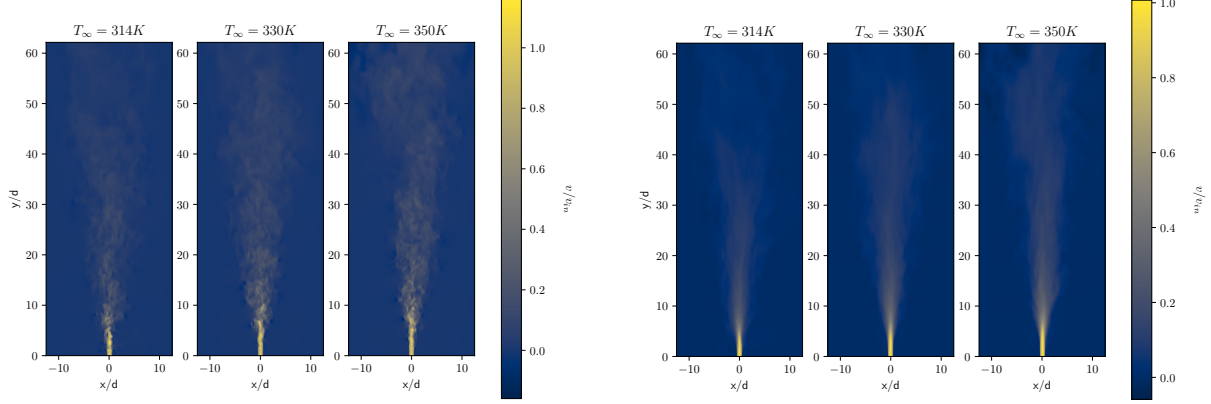


Figure 5.10: Axial velocity field comparison between 314K ambient case (left), 330K ambient case (middle), and 350K ambient case (right).

Figure 5.11 shows pressure fluctuations near the inlet for all three cases. Figure 5.11a contains an instantaneous snapshot of these fluctuations near the inlet. The $350K$ ambient case is comparable to the $330K$ ambient case, with similar large coherent structures forming in the pressure oscillations. However, the initial pressure waves emanating from the inlet are stronger in the $350K$ ambient case, resulting in slightly more intense fluctuations downstream. Minor spurious perturbations are also seen downstream in the $350K$ ambient case. The $314K$ ambient case is qualitatively much different from the other two cases. Larger coherent structures are much less defined, with smaller fluctuations appearing much more prominently throughout. There is also a band of cells slightly before $y/d = 2$ where perturbations are more concentrated. Average pressure fluctuation can be seen in Figure

5.11b. All cases have a slight increase in pressure isolated within the potential core surrounded by and followed with a pressure drop. The difference between these low and high pressure pockets is most prominent in the $314K$ ambient case, followed by the $330K$ ambient case. Numerical artifacts are extremely prominent in the $314K$ ambient case with some similar artifacts present in the $350K$ ambient case as well. These artifacts are most likely a result of issues regarding the AMR and SRK EoS, i.e., slight inconsistencies of states between coarse cells may be exacerbated by the AMR at this point in the domain. For conditions nearer the pseudo-boiling point, where density gradients are steeper, the fluctuations are more pronounced, hence our suspicion that some aspect of the SRK EoS implementation plays a part in the issue. AMR is definitely a component of the problem but further investigation is needed to discern the specifics involved with this issue. Pressure in general is a sensitive field, and since these fluctuations are not apparent in other plots, we do not expect them to impact the conclusions drawn from other features investigated here.

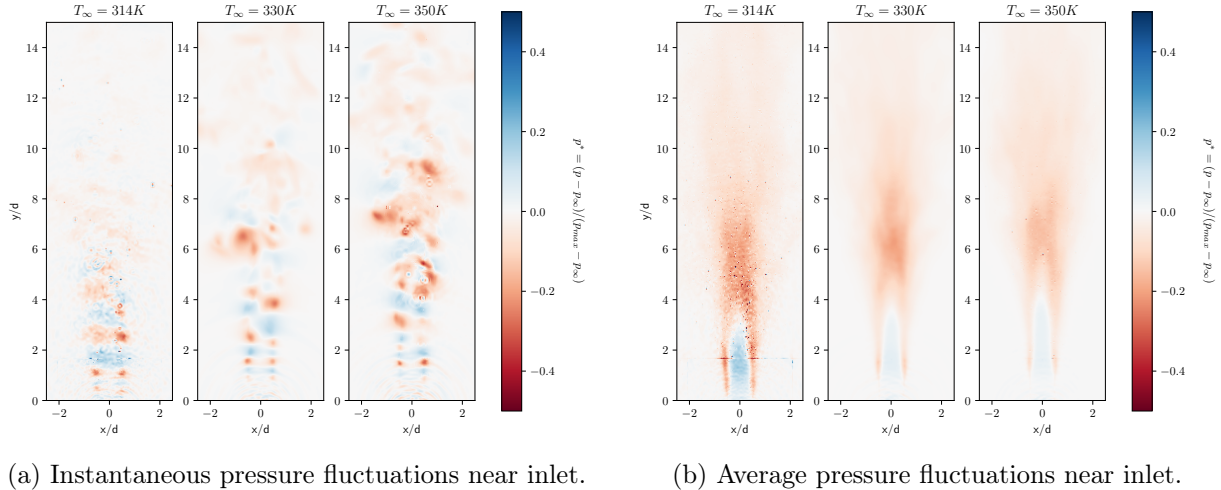


Figure 5.11: Pressure fluctuation field comparison between $314K$ ambient case (left), $330K$ ambient case (middle), and $350K$ ambient case (right).

Figure 5.12 shows both instantaneous and time-averaged flow fields of the vorticity magnitude for the three cases. The vorticity magnitude features seen in Figure 5.12a follow similar trends as the axial velocity. In all three cases, the strongest vorticity occurs along the jet edge at the inflow, leading to vortex formation and subsequent fluctuations. The $314K$ ambient case has a shorter region of steady flow in and also features larger, more distinct vortex formation along the edge of the jet. These vortices roll along the edge in tandem before mixing to lead into the

transition region around approximately $y/d = 3$ for the $314K$ ambient case and $y/d = 5$ for the $350K$. Immediately following this initial vortex formation, jet behavior begins to diverge between the two cases. The $314K$ ambient case maintains coherent large vortex structures farther along downstream compared to the $350K$ case. As these larger structures disintegrate, it appears that positive interference between edge vortices leads to finer, more compact filament structures with higher pockets of vorticity as compared to the $350K$ ambient case. These finer structures then more rapidly decay in the downstream direction. The $350K$ ambient case maintains higher vorticity intensity downstream with more prolonged pockets of higher vorticity seen in the transition region of the jet compared to that of the $330K$ ambient case. Similar to what was seen with the $314K$ ambient pressure field, there are some vorticity artifacts present in the mesh at the edge of the initial high-refinement zone surrounding the jet inlet. Similar to the $350K$ ambient case, the $314K$ ambient case also maintains some pockets of high vorticity, but then decays more rapidly overall compared to the other two cases. The averaged vorticity magnitude fields in Figures 5.12b and 5.12c showcases the different jet regions and jet spreading. From Figure 5.12b one can see that the $350K$ ambient case has more widespread vorticity in the transition region from around $5 \leq y/d \leq 15$ and then maintains the intensity formed here for farther along downstream compared to the $330K$ ambient case. The $314K$ ambient case has a much narrower vorticity range in the same region with intensity decaying much more rapidly downstream. Near the inlet, as depicted in Figure 5.12c, it is easier to see that the $314K$ ambient case begins spreading much earlier than the other two cases and has much less uniform vorticity along the jet edges. This earlier breakup also impacts the way the high-vorticity outer edges of the jet merge around the low-vorticity center at the end of the potential core, where the merging of the two jet edges across the middle meet in an almost concave point as compared to the more convex central region seen in the other two cases. The vorticity fluctuations before the mesh refinement change may contribute to the vorticity artifacts seen here. We believe these artifacts are due to a post-processing issue from a previous iteration of the code that has since been resolved. Again, since the velocity field appears relatively smooth by comparison, we do not expect the artifacts seen here to significantly impact the conclusions discussed later on.

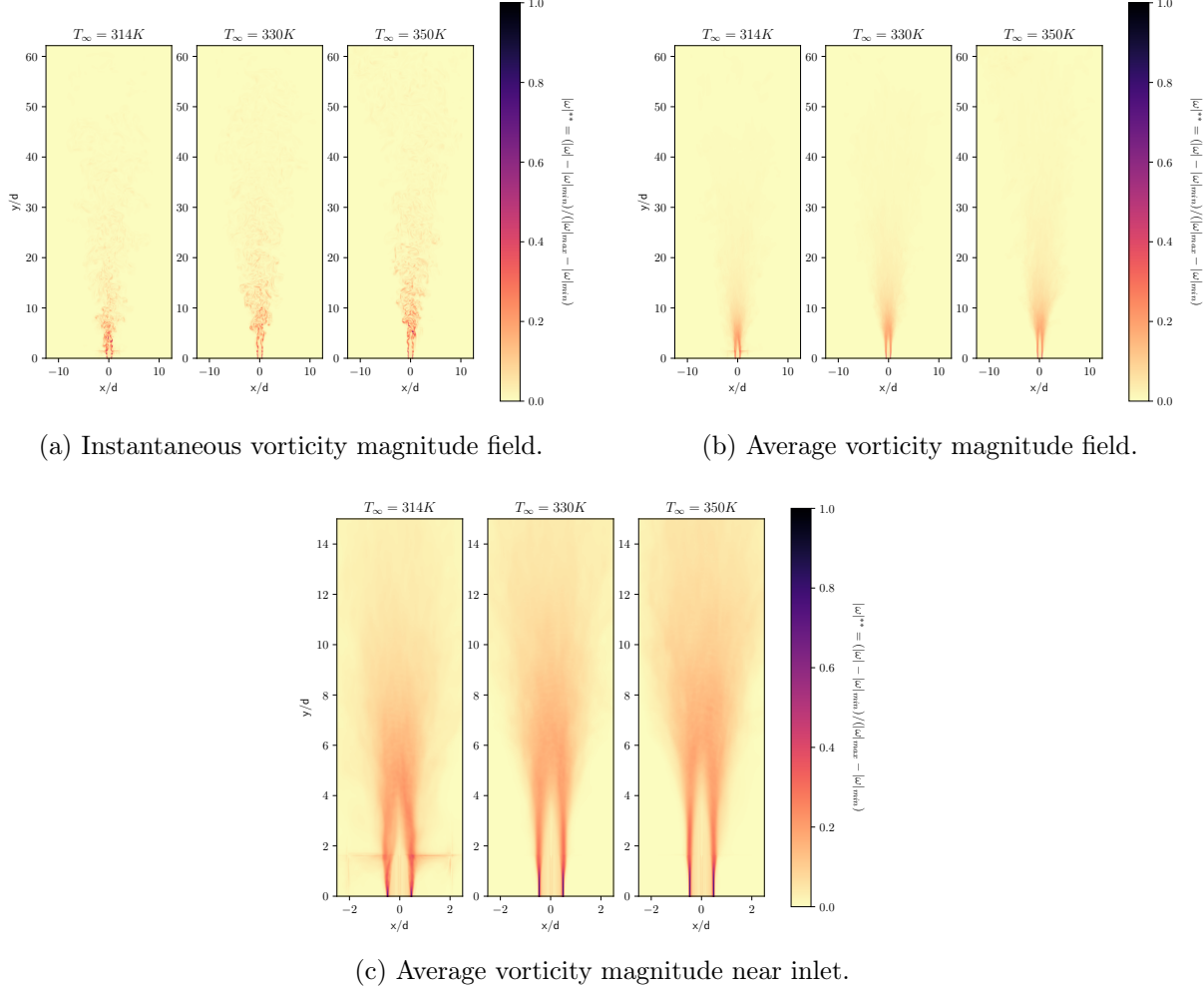
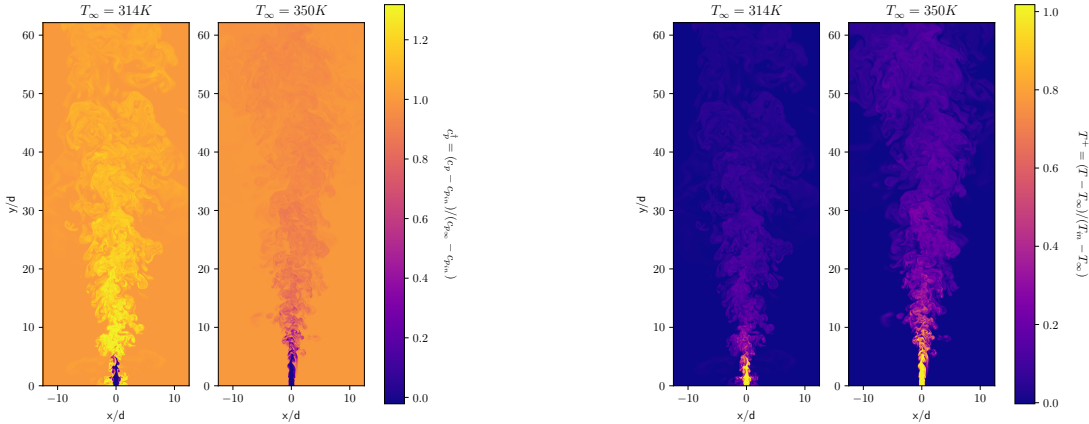


Figure 5.12: Vorticity magnitude field comparison between 314K ambient case (left), 330K ambient case (middle), and 350K ambient case (right).

The final figure in this section, Figure 5.13, contains direct comparisons between the two non-isothermal cases for various quantities of interest. Figure 5.13a shows the constant-pressure specific heat variation between the two cases. The added peak in specific heat can be seen in the 314K ambient case as the fluid transitions through the pseudo-boiling point. This peak occurs at the jet edge in the potential core and is additionally maintained after the transition region, showing a slower transition to the ambient specific heat as compared to the 350K ambient case. This layer of peak specific heat between the jet and ambient fluid creates a thermal shield around the jet, where most energy goes toward expanding the volume of the fluid as opposed to raising the temperature [47]. This effect can be seen in comparing Figures 5.13b and 5.13c. In regions of heightened constant-

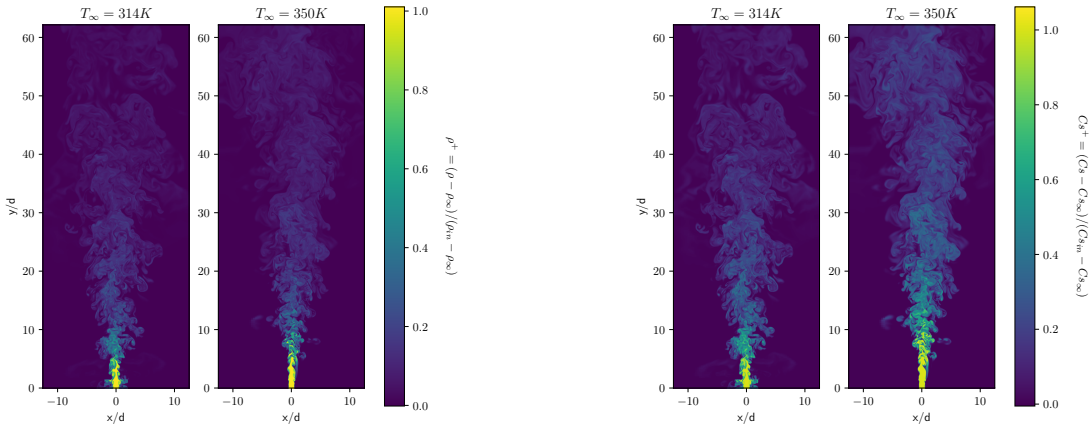
pressure specific heat, density change in the $314K$ ambient case is comparable to the $330K$ ambient case, even though the former involves gas-like injection into a liquid-like background and the latter involves gas-like supercritical fluids for both injection and background flow. In the transition region of the $314K$ ambient jet, temperature drops dramatically in an area of high mixing just past the potential core. Thereafter, temperature decays much more slowly as the specific heat remains at peak levels for the remainder of the jet propagation.

The last group of images, Figures 5.13d, 5.13e, and 5.13f, show the sound speed, enthalpy, and compressibility factor of the fluid, respectively. All three quantities exhibit similar trends, with the $350K$ ambient case showing a more rapid transition to the ambient conditions as compared to the $314K$ ambient case. These follow the same trend as seen in the temperature, but to varying degrees of intensity. For example, enthalpy has an overall faster downstream decay for both cases as compared to the temperature decay, while sound speed and compressibility factor have comparable decay rates.



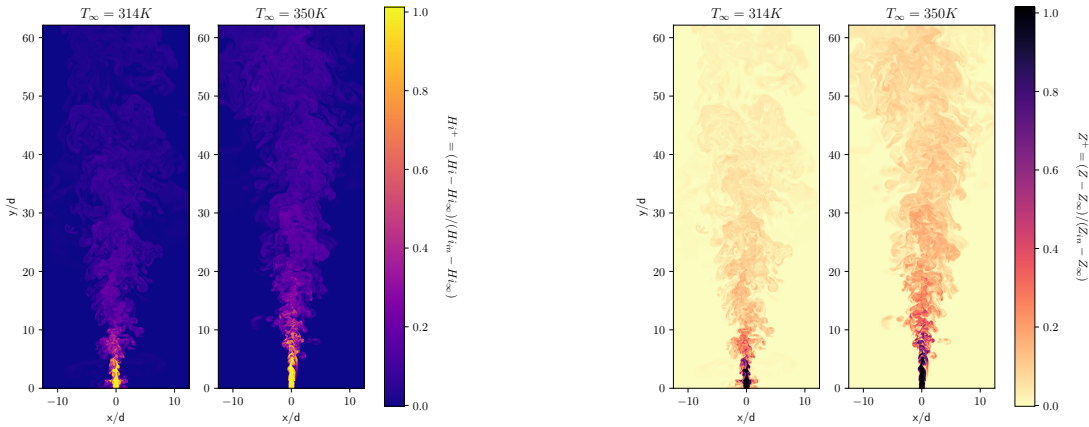
(a) Instantaneous constant pressure specific heat.

(b) Instantaneous temperature field.



(c) Instantaneous density.

(d) Instantaneous sound speed.



(e) Instantaneous enthalpy.

(f) Instantaneous compressibility factor

Figure 5.13: Direct comparison between 314K ambient case (left) and 350K ambient case (right) for various fluid quantities of interest.

5.2.2 Mean Flow Properties

Figure 5.14 depicts the time and radially averaged scaled axial velocity component plotted against radial distance from the centerline at multiple normal slices downstream from the inlet. The velocity is scaled by the average axial velocity value at the inflow while the radial direction is scaled by the jet diameter. In both cases, velocity profiles flatten as they get farther downstream. Compared to the $330K$ ambient case, the $350K$ ambient case has a slower axial velocity decay downstream while the $314K$ ambient case has a much faster decay. This agrees with the trends seen in the vertical slice images.

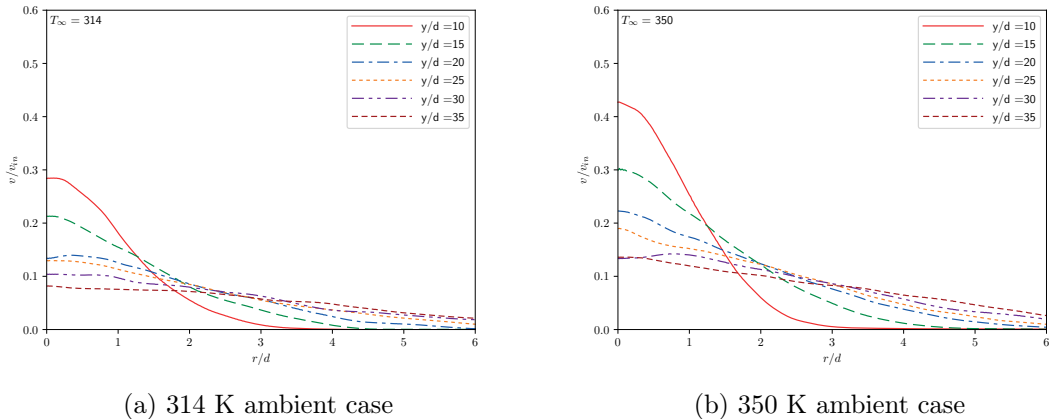


Figure 5.14: Average (both in time and radially) axial velocity scaled by inlet value plotted along radial distance from centerline.

Figure 5.15 shows a different scaling of the axial velocity profiles depicted in the previous figure. Here, the axial velocity is scaled by the centerline value at each normal slice while the radial distance is scaled by the $r_{1/2}$, as was done in Figure 5.5. Figures 5.15a and 5.15b show the near field profiles resulting from this scaling. As was the case with the $330K$ ambient case, self-similarity is seen in the near field for the non-isothermal cases, where fairly agreeable profile collapse occurs at $y/d = 15$. The $350K$ ambient case profiles are slightly more in-line with each other as compared to the $314K$ ambient case, but both demonstrate a general tendency toward self-similarity still. Figures 5.15c and 5.15d however do not show as agreeable a collapse as the $330K$ ambient case. The $314K$ ambient case has better self-similarity structure toward the centerline of the jet as compared to the $350K$ ambient case, though the outer edge of the jet has a wider disparity between profiles.

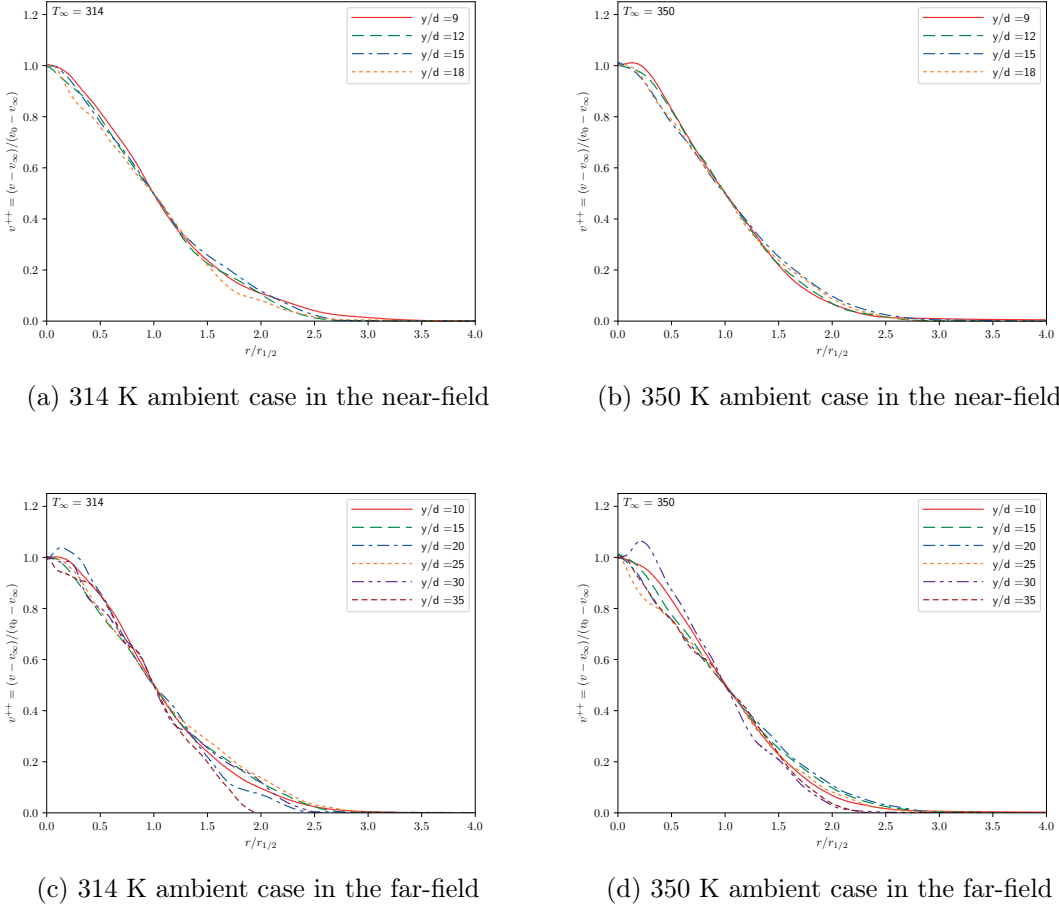


Figure 5.15: Normal slices of scaled near-field and far-field axial velocity profiles, averaged in both time and the radial direction. Plotted against radial direction scaled by $r_{1/2}$.

Density self-similarity is not as evident as is in axial velocity profiles, as can be seen in Figure 5.16. The 350K ambient case profile spread is not nearly as tight as it was with the axial velocity. The 314K case is even worse, with more prominent fluctuations in the curves than any of the previous profile depictions. Far-field density in this case has the widest spread of all previous comparisons. These density fluctuations and lack of self-similarity could be related to the increased Kelvin-Helmholtz instabilities seen in the 314K ambient case and the subsequent density decay as seen in Figure 5.13c. One interesting feature of these plots can be seen on the outer edge of the jet, past the HMHW mark. For the 314K ambient case, profiles exhibit an initial decay as they dip below the $y/d = 10$ profile before increasing to fall above this initial curve at later slices downstream.

This is opposite to what is seen in the $350K$ ambient case, where earlier slices rise above the initial curve at $y/d = 10$ before decaying below it farther downstream. This later decay is consistent with what is seen in the axial velocity self-similarity curves for both cases, while the density profiles for the $314K$ ambient case break from this pattern.

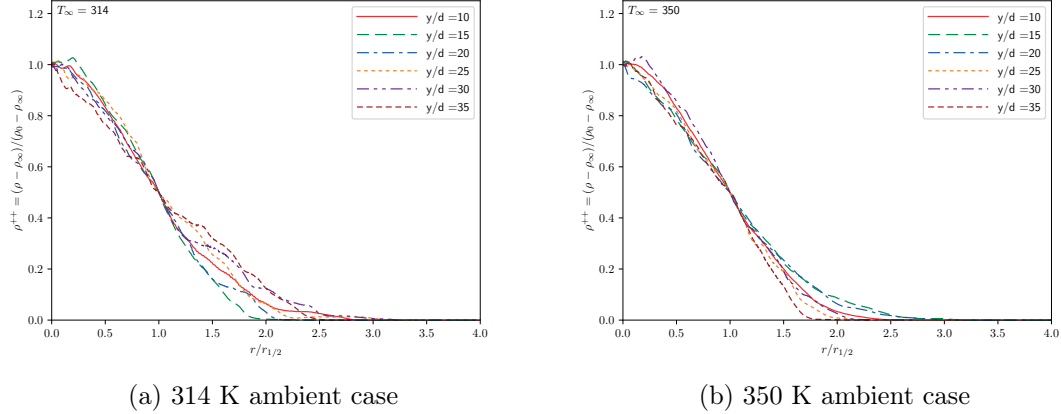


Figure 5.16: Normal slices of scaled far-field density, averaged in both time and the radial direction, plotted in the radial direction scaled by $r_{1/2}$.

Figure 5.17 shows the recovery of linear decay in the axial velocity along the centerline of the jet for each case. The $350K$ ambient case has a less steep slope compared to the $330K$ ambient case seen in Figure 5.6, where the decay rate according to Equation (5.1) is $B_v = 4.48$. This corresponds to slower decay of the axial velocity along the centerline. The $314K$ ambient case has a steeper slope compared to the $330K$ ambient case, with $B_v = 2.92$, corresponding to a faster decay in axial velocity along the centerline. These findings are consistent with the analysis from Figure 5.14.

Similarly, Figure 5.18 shows the recovery of linear spreading rate along the centerline of the jet for each case. The $350K$ ambient case has a steeper slope compared to the $330K$ ambient case seen in Figure 5.6, where the decay rate according to Equation (5.1) is $C_v = 0.115$. This corresponds to slower decay of the axial velocity along the centerline. The $314K$ ambient case has a steeper slope compared to the $330K$ ambient case, with $C_v = 0.122$, corresponding to a faster decay in axial velocity along the centerline. These findings are consistent with the analysis from Figure 5.14. Overall the jet in the $314K$ ambient case decays faster in the axial direction while spreading further in the radial direction compared to that of the $350K$ ambient case.

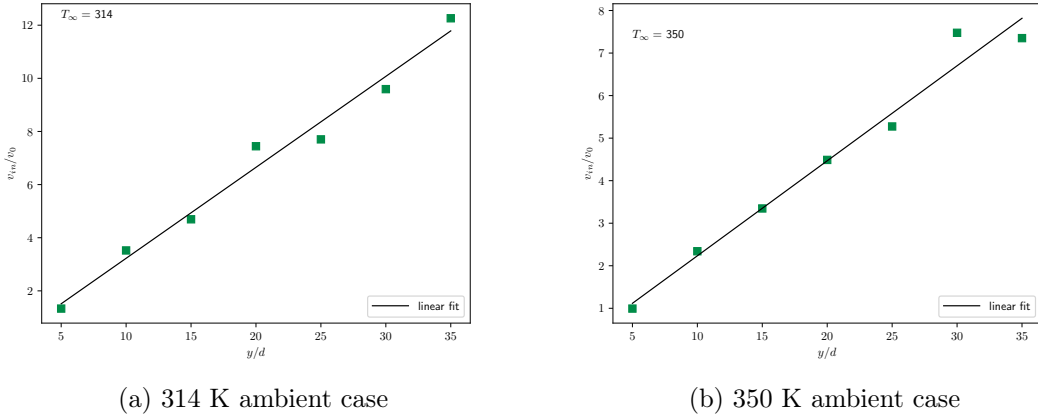


Figure 5.17: Axial inlet velocity scaled by centerline values along the axial direction. When distance downstream is scaled by jet diameter, linear decay of the centerline axial velocity is observed.

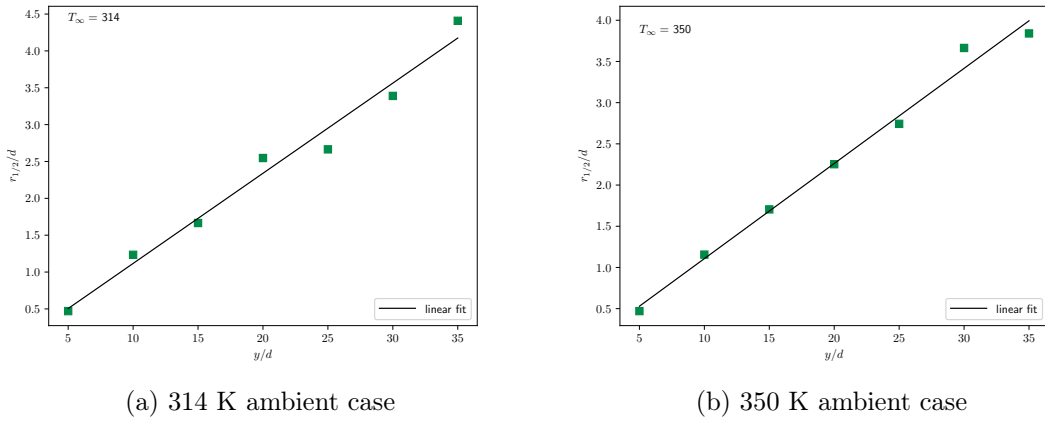


Figure 5.18: HMW values scaled by jet diameter along the axial direction. When distance downstream is scaled by jet diameter, linear growth of the half-widths is observed.

Finally, Figure 5.19 shows various quantities along the centerline for both non-isothermal cases. For all quantities presented here, centerline plots help depict the different regions of the jet. The potential core is maintained until around $y/d = 2.5$ for the $314K$ ambient case and until around $y/d = 5$ for the $350K$ ambient case. Then there is a transition region where quantities experience rapid change. This occurs up until about $y/d = 10$ for the $314K$ ambient case and $y/d = 12$ for the $350K$ ambient case. After that, a gradual leveling out occurs as the quantity of interest continues

to adjust as it mixes with the ambient fluid through the remainder of the domain. Figure 5.19a shows the temperature change for each case along the centerline of the jet. The $314K$ ambient case exhibits a more rapid decay from the inflow temperature as compared to the $350K$ ambient case, as can be seen in the separation between the curves between $4 \leq y/d \leq 16$. Afterwards, they continue their respective transition toward ambient conditions at roughly the same rate. The $350K$ ambient case is never as close to ambient conditions as the $314K$ ambient case due to the slower initial decline, hovering instead around $T^+ = 0.18$ as compared to the $T^+ = 0.14$ that the $314K$ ambient case sits at. Enthalpy and the compressibility factor in Figures 5.19e and 5.19f respectively follow the same trend though with less separation between the two cases as compared to the temperature trajectories. Figure 5.19d shows the sound speed transition along the centerline. Compared to the previously discussed quantities, the sound speed decay appears much more gradual, with little rate difference between the two cases. The initial transition region is less steep and the region thereafter more of a continued gradual decline as opposed to a leveling out like the other quantities. Figure 5.19b shows the constant-pressure specific heat for the two non-isothermal cases. Again, neither fully transitions to the ambient condition as the jet persists through the domain. Here the jump in specific heat over the peak present near the pseudo-boiling point can be seen for the $314K$ ambient case. This case also has a steeper initial transition than the other case does, though both have similar rates of approach toward ambient conditions after this initial shift. Figure 5.19c shows the density of the two cases. This quantity follows a unique trajectory between the two cases compared to those previously discussed. Here, the initial transition rate of the two cases from the potential core to the fully developed region is nearly the same. Toward the end of this transition though, the $314K$ ambient case begins to level out at a faster rate than the $350K$ ambient case, allowing the curves to collapse onto each other. Then both centerline densities continue on past $y/d = 16$ at approximately $\rho^+ = .12$ and steadily decline toward ambient conditions thereafter.

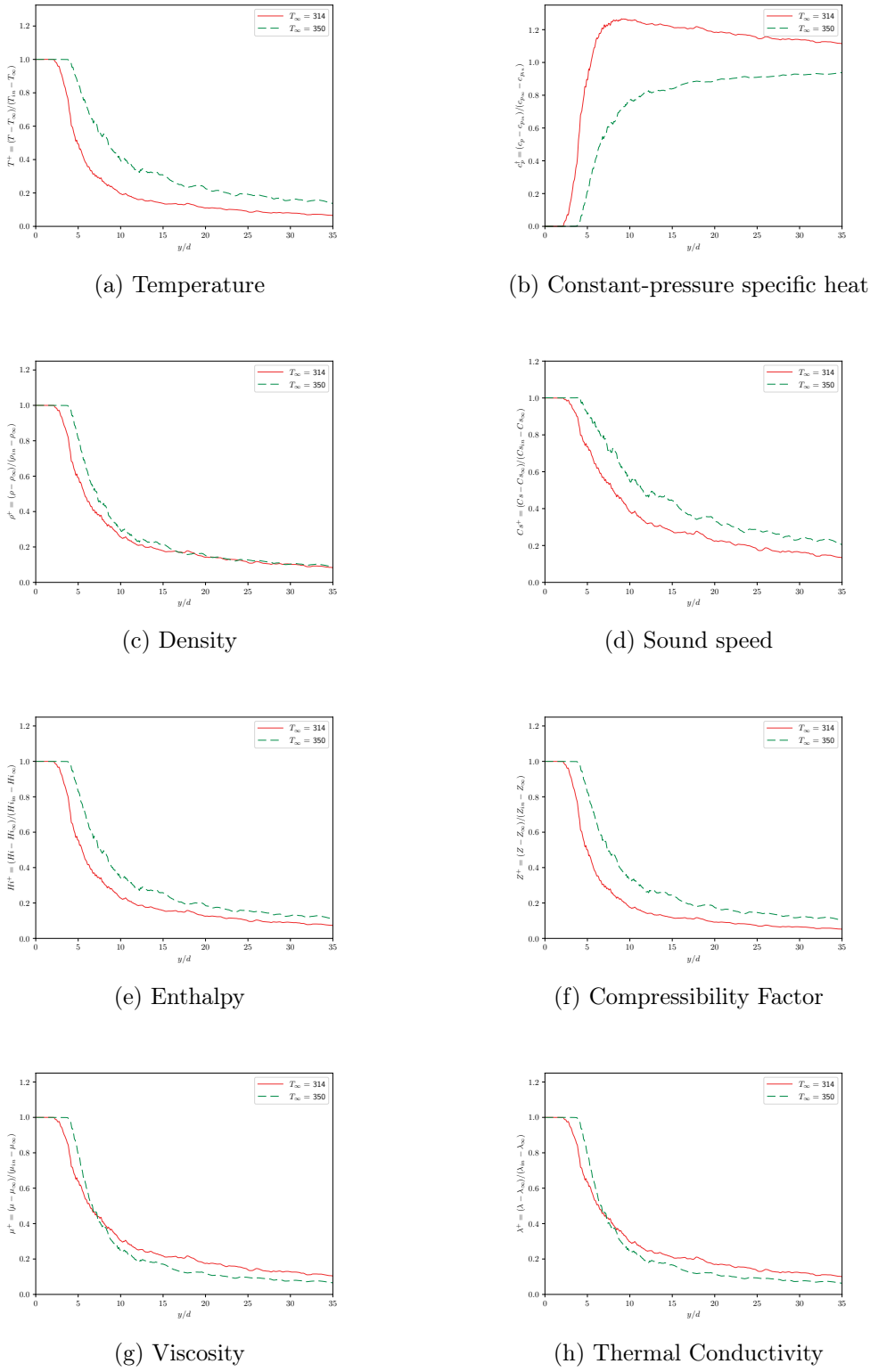


Figure 5.19: Comparison of centerline decay for various fluid quantities.

5.2.3 Turbulence Dynamics

Figure 5.20 shows the resolved Reynolds stresses of each non-isothermal case at two different locations downstream. As was the case with the 330K ambient resolved Reynolds stresses in Figure 5.8, self-similarity in the axial direction is not recovered. The Reynolds stresses for both of the non-isothermal cases are generally smaller than their counterparts in the isothermal case. The stresses in Figure 5.20b generally follow the trends outlined in the isothermal case, but the remaining slices for these two cases do not follow suit, with little to no separation between the axial direction stresses and the other stresses. This could be due the effects of the SGS modeling as mentioned in [64].

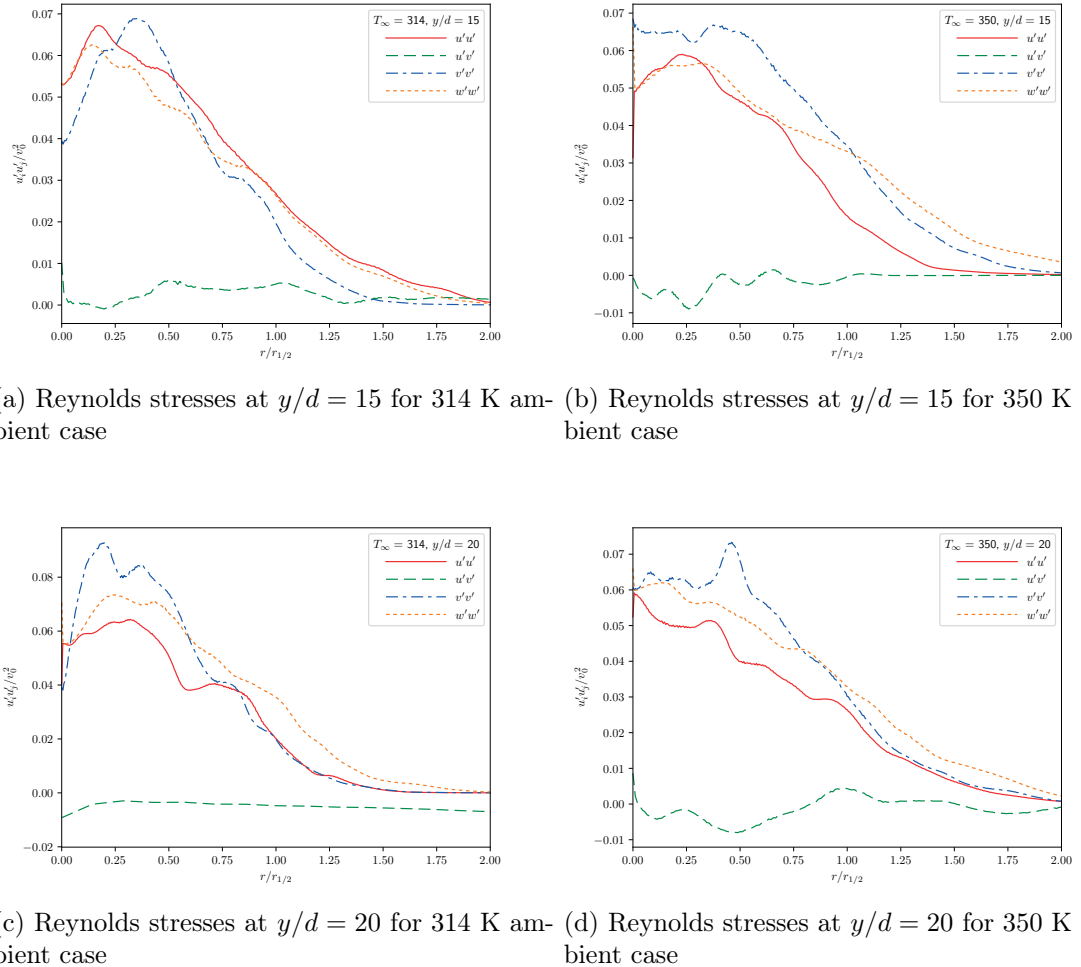


Figure 5.20: Time and radially averaged Reynolds stresses for the non-isothermal jets at two locations downstream.

Figure 5.21 shows the components of the resolved TKE for each non-isothermal case. Both cases follow the same general trends seen in the $330K$ ambient case, with the axial component being the strongest and the other two components being of the same magnitude. The $350K$ ambient case is the most similar to the $330K$ ambient case between the two. For this case, peak TKE occurs at approximately $y/d = 7$, which is slightly later than the isothermal case. Additionally, this peak is aligned with the peak seen in the other components, where for the isothermal case the axial component peak came slightly before the peak of the other two. The magnitude of the peak axial component is larger in the $350K$ ambient case while the magnitudes of the other directional components are similar to their counterparts in the $330K$ ambient case. The decay rate is also slightly higher in the $350K$ ambient case compared to the isothermal case. The TKE components of the $314K$ ambient case reach their peaks slightly earlier than the $330K$ ambient case at about $y/d = 5$. The peak of the axial component is much larger than that of the other two cases. Additionally, the other TKE components of the $314K$ ambient case have a smaller magnitude than their counterparts in the other cases, resulting in a larger disparity between the magnitudes of the components in this case. There is also stronger overall decay in the $314K$ ambient case as compared to the $350K$ ambient case.

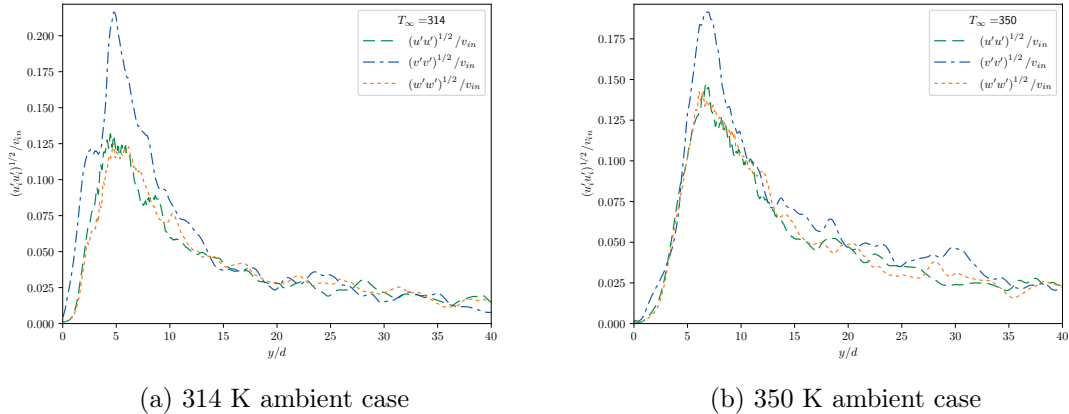


Figure 5.21: Comparison of average turbulent kinetic energy components along centerline for each non-isothermal case.

Figure 5.22 further emphasizes the differences between the TKE components and overall TKE by directly comparing each quantity across all cases. For all quantities, the $314K$ ambient case peaks before the other two cases. For the overall resolved TKE and the axial component, the $330K$ ambient

case is next to the peak, followed by the $350K$ ambient case. For the cross directional components, the peaks of these two cases coincide. The $314K$ ambient cases experiences the strongest decay along the centerline immediately following the peak for each quantity, however, the other two cases eventually decay to the same value so that all cases exhibit a roughly equivalent leveling off as the jet progresses through the remainder of the domain.

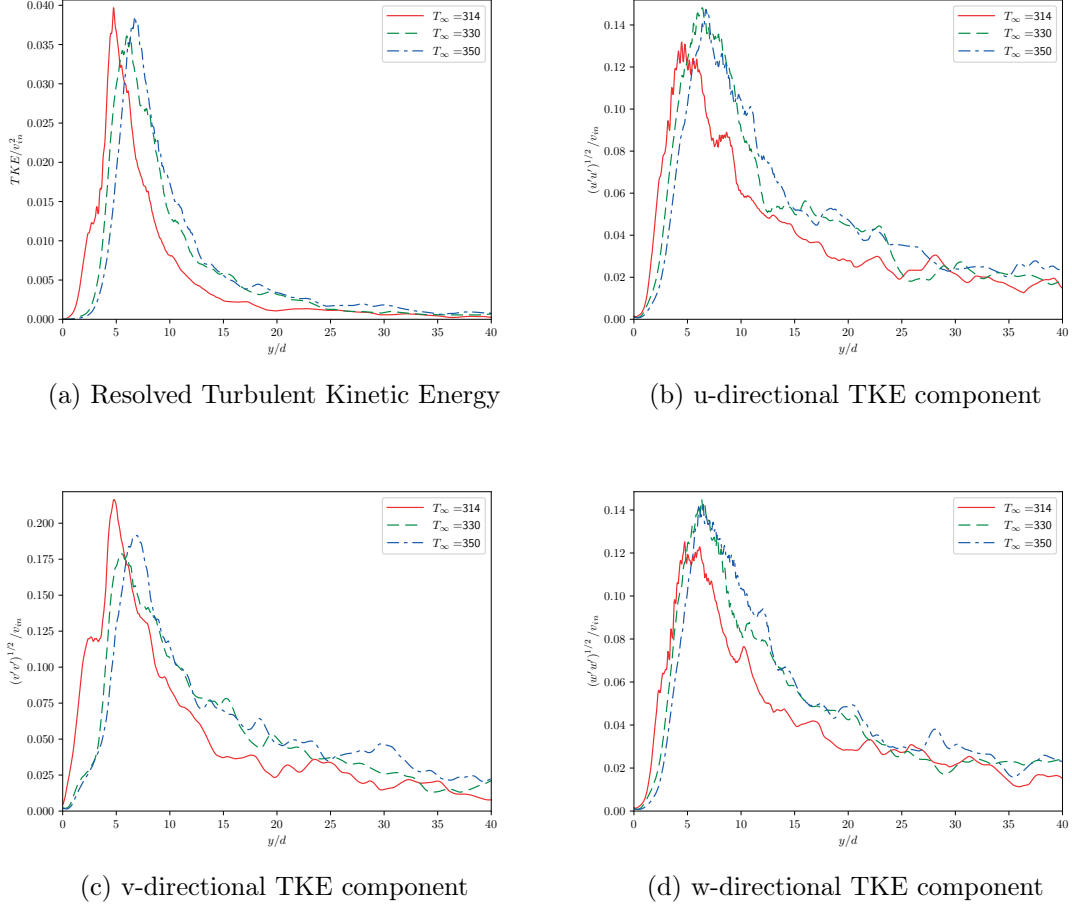


Figure 5.22: Cross-case comparisons of average turbulent kinetic energy components and total resolved TKE along centerline.

5.2.4 Discussion

Key differences in the flow structure between the $350K$ and $314K$ ambient cases of supercritical fluid injection are noted. Vertical slice imaging in Figures 5.10, 5.11, 5.12, 5.13 depicts qualitative differences between the non-isothermal cases. In general, the $350K$ ambient case has a very similar

flow structure compared to the isothermal case. Thus, the introduction of variable density dynamics does not heavily impact jet behavior when moving away from the pseudo-boiling point. This is not the case when moving across the pseudo-boiling point.

One of the main effects of crossing the pseudo-boiling point that can be seen in the vertical slice images and centerline plots is the formation of barrier of high constant-pressure specific heat. The effects of this “thermal-shielding” [47] on a denser jet can be seen in the experimental work of Mayer et al. [60] and Chehroudi et al. [17], and some of the numerical counterparts of these studies [47, 113]. In these studies, the thermal-shield contributes to a sharp density gradient at the jet-ambient interface, which stabilizes the shear layer and allows for further jet penetration before jet breakup [47]. Density gradient stratification in these cases also contributes to finger-like structures formed downstream in the pseudo-boiling case, which are not evident in the case moving away from the pseudo-boiling point [47]. In this study, however, a lighter, warmer jet is propelled into a denser, cooler ambient fluid for the case that crosses the pseudo-boiling point, so the specific heat peak enhances a flipped density gradient. The stabilizing effects of density stratification here may be overcome by the volume dilatation [51], not only enabling but amplifying the vortex formation related to a Kelvin-Helmholtz-like instability.

Spreading rate and decay of the jet is ultimately also enhanced by the pseudo-boiling region, as compared to both the non-isothermal case here and typical values for spreading rate and decay seen in the literature for subcritical jets [35]. As larger vortex pairs deteriorate at the end of the potential core, high levels of mixing occur as denser ambient fluid is entrained in the lighter jet. This entrained fluid with higher thermal conductivity and constant-pressure specific heat allows for better transfer of thermal energy and faster density adjustment. As this mixing occurs, jet penetration is slowed and the lower-density liquid builds and expands spanwise in the denser-ambient surrounding. This enhanced spreading and decay is also found in similar numerical simulations [51] and some recent experiments [99].

A feature not found in the literature that is explored here is the increase in anisotropy regarding turbulent kinetic energy when crossing the pseudo-boiling point. In general, anisotropy of the resolved turbulent kinetic energy in the isothermal and other non-isothermal cases is comparable to that seen in higher Mach or lower Reynolds flow subcritical compressible flows as is explored in [14]. This implies that compressibility may play an important role in the enhanced mixing features seen in not only supercritical fluids in general, but especially in the case where pseudo-boiling is involved.

CHAPTER 6

CONCLUSION

In this work, we studied three cases of a supercritical round turbulent jet injected into a supercritical environment: an isothermal case, a non-isothermal case with ambient temperature farther away from the critical point, and a non-isothermal case with ambient temperature closer to the critical point and specifically crossing a region of intense thermodynamic fluctuation known as the pseudo-boiling point. It was shown that the isothermal case had many similarities with ideal incompressible round jets. Many properties found in classical round turbulent jets were recovered in this case, such as self-similarity, linear decay along the centerline, and general trends associated with Reynolds stresses (although self-similarity in the Reynolds stresses was not recovered; general trends were still agreeable). The non-isothermal case farther away from the critical point behaved similarly to the isothermal case with slight differences being noted in potential core length and spreading rate of the jet. The non-isothermal case that transited the pseudo-boiling point exhibited noticeably different behavior.

The effects of pseudo-boiling density stratification was demonstrated for low-to-high density supercritical jet injection, in contrast to the more common high-to-low density injection scheme found in existing literature. Earlier onset of Kelvin-Helmholtz-like instabilities in the jet-ambient interface ultimately contributes to faster mixing and jet decay as compared to the other non-isothermal case presented here. Of note with this regard, resolved turbulent kinetic energy in this case is redirected from the spanwise direction to the streamwise direction, displaying enhanced isotropy in the pseudo-boiling case. To the author's knowledge, this feature has not been explored in the current literature regarding pseudo-boiling in supercritical jet configurations. Jet decay and spreading rate are both enhanced compared to the other non-isothermal case, but may be even more so due to pseudo-boiling. A further investigation regarding lighter density supercritical injection could be useful in exploring this effect further.

Some limitations of this work are now noted. SGS models do not take into consideration real gas behavior, being limited to assumptions based on the ideal gas equation of state. There is room for improvement in turbulence modeling with the aim of incorporating higher order equations of state to the model formulation. As with any numerical simulation, discretization and resolution inherently

lead to error. Ideally with more power, finer resolution can be achieved to help improve simulations. Finally, minor artifacts were noted in the non-isothermal case closest to the critical point likely due to the presence of steep gradients and issues with post-processing procedures. Though the impact of these are believed to be mild, they are still present and add to cumulative error.

Future work aims to incorporate multiple species to the flow system and to investigate higher Mach flows. The impact of more specific application-oriented configurations with complex geometries on the flow field is also of interest.

APPENDIX A

TRANSPORT COEFFICIENTS

EGLib Low Pressure Approximation Coefficients

Table A.1: Coefficients for EGLib Polynomials [28] used to model transport quantities as described in Equation (2.19)

i	$a_{\mu,i}$	$a_{\lambda,i}$
0	$-2.281\ 103\ 45 \times 10^1$	-8.74831432
1	4.62954710	4.79275291
2	$-5.006\ 890\ 01 \times 10^{-1}$	$-4.186\ 850\ 61 \times 10^{-1}$
3	$2.100\ 129\ 69 \times 10^{-2}$	$1.352\ 102\ 42 \times 10^{-2}$

Chung High Pressure Corrections

Chung et al. [18] details the derivation of these general transport coefficients via their regression analysis of various fluids. The coefficients for the linear approximation are printed here for convenience as they are implemented in *PelePhysics* [6].

Table A.2: Quantities used in part for Chung's High Pressure Corrections. Values gathered from EGLib approximations [28]

Transport Quantity, Symbol (Units)	Value
Molar Mass, M (g/mol)	$4.400\ 995 \times 10^1$
Lennard Jones Potential Well Depth, ϵ_k (K)	$2.440\ 000 \times 10^2$
Lennard Jones Collision Diameter, σ (\AA)	3.763
Reduced Dipole Moment, μ_r (D)	0.0
Association Factor, κ	0.0

Table A.3: Linear Coefficients Used in Calculating High Pressure Viscosity Corrections as found by Chung et al. [18]

i	a_{i0}	a_{i1}	a_{i2}	a_{i3}
1	6.32402	50.41190	-51.68010	1189.02000
2	0.12102×10^{-2}	-0.11536×10^{-2}	-0.62571×10^{-2}	0.37283×10^{-1}
3	5.28346	254.20900	-168.48100	3898.27000
4	6.62263	38.09570	-8.46414	31.41780
5	19.74540	7.63034	-14.35440	31.52670
6	-1.89992	-12.53670	4.98529	-18.15070
7	24.27450	3.44945	-11.29130	69.34660
8	0.79716	1.11764	0.12348×10^{-1}	-4.11661
9	-0.23816	0.67695×10^{-1}	-0.81630	4.02528
10	0.68629×10^{-1}	0.34793	0.59256	-0.72663

Table A.4: Linear Coefficients Used in Calculating High Pressure Thermal Conductivity Corrections as found by Chung et al. [18]

i	b_{i0}	b_{i1}	b_{i2}	b_{i3}
1	2.41657	0.74824	-0.91858	121.72100
2	-0.50924	-1.50936	-49.99120	69.98340
3	6.61069	5.62073	64.75990	27.03890
4	14.54250	-8.91387	-5.63794	74.34350
5	0.79274	0.82019	-0.69369	6.31734
6	-5.86340	12.80050	9.58926	-65.52920
7	81.17100	114.15800	-60.84100	466.77500

APPENDIX B

ADDITIONAL THERMODYNAMIC QUANTITIES

Ideal Gas NASA Polynomial Fits Coefficients

Table B.1: Coefficients for NASA polynomials [61] used in modeling ideal thermodynamic quantities as described in Equation (2.31)

i	$c_{e_I,i}$	$c_{v_I,i}$	$c_{h_I,i}$
0	1.356 773 52	1.356 773 52	2.356 773 52
1	$4.492\ 298\ 39 \times 10^{-3}$	$8.984\ 596\ 77 \times 10^{-3}$	$4.492\ 298\ 39 \times 10^{-3}$
2	$-2.374\ 520\ 90 \times 10^{-6}$	$-7.123\ 562\ 69 \times 10^{-6}$	$-2.374\ 520\ 90 \times 10^{-6}$
3	$6.147\ 975\ 55 \times 10^{-10}$	$2.459\ 190\ 22 \times 10^{-9}$	$6.147\ 975\ 55 \times 10^{-10}$
4	$-2.873\ 990\ 96 \times 10^{-14}$	$-1.436\ 995\ 48 \times 10^{-13}$	$-2.873\ 990\ 96 \times 10^{-14}$

SRK-Related Derivatives

Here are a few additional derivatives involving quantities related to the SRK EoS that are used at various points for the computations within *PelePhysics* [6]:

Constant-Pressure Specific Heat

$$c_p = \left(\frac{\partial h}{\partial T} \right)_p = \frac{\partial h}{\partial T} - \frac{\frac{\partial h}{\partial V_m}}{\frac{\partial p}{\partial V_m}} \frac{\partial p}{\partial T} \quad (\text{B.1})$$

where

$$\frac{\partial p}{\partial T} = \frac{R}{V_m - b} - \frac{\partial a}{\partial T} \frac{1}{V_m(V_m + b)} \quad (\text{B.2})$$

$$\frac{\partial p}{\partial V_m} = -\frac{RT}{(V_m - b)^2} + \frac{a(2V_m + b)}{[V_m(V_m + b)]^2} \quad (\text{B.3})$$

$$\frac{\partial h}{\partial V_m} = -\left(T \frac{\partial a}{\partial T} - a \right) \frac{1}{V_m(V_m + b)} + \frac{a}{(V_m + b)^2} - \frac{RTb}{(V_m - b)^2} \quad (\text{B.4})$$

$$\frac{\partial h}{\partial T} = c_p^{id} + T \frac{\partial^2 a}{\partial T^2} \frac{1}{b} \ln\left(1 + \frac{b}{V_m}\right) - \frac{\partial a}{\partial T} \frac{1}{V_m + b} + \frac{Rb}{V_m - b} \quad (\text{B.5})$$

Sound Speed

$$c_s^2 = -\frac{c_p}{c_v} V_m^2 \frac{\partial p}{\partial V_m} \quad (\text{B.6})$$

Primitive Derivatives Needed for Riemann Solver

$$\left. \frac{\partial p}{\partial \rho} \right|_p = -V_m^2 \left(\frac{\partial p}{\partial V_m} - \frac{\frac{\partial e}{\partial V_m}}{\frac{\partial e}{\partial T}} \frac{\partial p}{\partial T} \right) \quad (\text{B.7})$$

$$\left. \frac{\partial p}{\partial e} \right|_\rho = \frac{1}{c_v} \frac{\partial p}{\partial T} \quad (\text{B.8})$$

$$\frac{\partial e}{\partial V_m} = \frac{1}{V_m(V_m + b)} \left(a - T \frac{\partial a}{\partial T} \right) \quad (\text{B.9})$$

APPENDIX C

PELEC INPUT PARAMETERS FOR SIMULATIONS

Here inputs are provided to aid in reproducibility of the present simulations. Note though that the current version of *PeleC* may have different input structures compared to those displayed here. The following git hashes were used for this work:

PeleC git hash: v0.1-130-gd489031-dirty

AMReX git hash: 19.06-406-ge73f42267

PelePhysics git hash: v0.1-16-g64d0135

Figure C.1: Input parameters for available physics options in PeleC

```
&tagging
  denerr = 1e20
  dengrad = 1e20
  max_denerr_lev = 3
  max_dengrad_lev = 3

  presserr = 1e20
  pressgrad = 1e20
  max_presserr_lev = 3
  max_pressgrad_lev = 3

  velerr = 1e20
  velgrad = 1e20
  max_velerr_lev = 3
  max_velgrad_lev = 3

  temperr = 1e20
  tempgrad = 4.0
  max_temperr_lev = 3
  max_tempgrad_lev = 3

  vorterr = 5000
  max_vorterr_lev = 3

  vfracerr = 1e20
  max_vfracerr_lev = 5
  /
&extern
!
! Specific heat ratio for air
!
! eos_gamma = 1.4
!
/
```

Figure C.2: AMR tagging criteria selected within in PeleC

BIBLIOGRAPHY

- [1] Salonika Aggarwal and Marko Hakovirta. “Supercritical Carbon dioxide: Adequately Sole Solvent.” In: *American Journal of Engineering, Science and Technology* 10 (2021), pp. 46–61. URL: <https://journalsonline.org/american-journal-of-engineering-science-and-technology/pdfs/volume-10/4.pdf>.
- [2] Abdulaziz Alkandari and Alexander S. Rattner. “Characterization of laminar and turbulent supercritical carbon dioxide slot jet impingement heat transfer.” In: *International Journal of Heat and Mass Transfer* 193 (2022), p. 122949. ISSN: 0017-9310. DOI: <https://doi.org/10.1016/j.ijheatmasstransfer.2022.122949>. URL: <https://www.sciencedirect.com/science/article/pii/S0017931022004227>.
- [3] Rodney John Allam, Miles Palmer, Glenn William Brown, et al. *System and method for high efficiency power generation using a carbon dioxide circulating working fluid*. US Patent 8,596,075. Dec. 2013.
- [4] Rodney Allam et al. “Demonstration of the Allam Cycle: An Update on the Development Status of a High Efficiency Supercritical Carbon Dioxide Power Process Employing Full Carbon Capture.” In: *Energy Procedia* 114 (2017). 13th International Conference on Greenhouse Gas Control Technologies, GHGT-13, 14-18 November 2016, Lausanne, Switzerland, pp. 5948–5966. ISSN: 1876-6102. DOI: <https://doi.org/10.1016/j.egypro.2017.03.1731>. URL: <https://www.sciencedirect.com/science/article/pii/S187661021731932X>.
- [5] AMReX-Combustion. *PeleC*. <https://github.com/AMReX-Combustion/PeleC>. 2022.
- [6] AMReX-Combustion. *PelePhysics*. <https://github.com/AMReX-Combustion/PelePhysics>. 2022.
- [7] Ifeanyi Michael Smarte Anekwe et al. “Carbon dioxide capture and sequestration technologies—current perspective, challenges and prospects.” In: *Green Sustainable Process for Chemical and Environmental Engineering and Science* (2023), pp. 481–516.
- [8] André Bakker. *Lectures on Applied Computational Fluid Dynamics*. 2008. URL: <https://www.bakker.org/Lectures-Applied-CFD.pdf>.
- [9] D.T. Banuti. “Crossing the Widom-line - Supercritical pseudo-boiling.” In: *The Journal of Supercritical Fluids* 98 (2015), pp. 12–16. ISSN: 0896-8446. DOI: <https://doi.org/10.1016/j.supflu.2014.12.019>. URL: <https://www.sciencedirect.com/science/article/pii/S0896844614004306>.
- [10] G. K. Batchelor. *An Introduction to Fluid Dynamics*. Cambridge Mathematical Library. Cambridge University Press, 2000. DOI: [10.1017/CBO9780511800955](https://doi.org/10.1017/CBO9780511800955).

- [11] R. Benzi and U. Frisch. “Turbulence.” In: *Scholarpedia* 5.3 (2010). revision #137205, p. 3439. DOI: [10.4249/scholarpedia.3439](https://doi.org/10.4249/scholarpedia.3439).
- [12] Roberto Benzi. “Lewis Fry Richardson.” In: *A Voyage Through Turbulence*. Ed. by Peter A. Davidson et al. Cambridge University Press, 2011, 187?208. DOI: [10.1017/CBO9781139018241.006](https://doi.org/10.1017/CBO9781139018241.006).
- [13] BJ Boersma and SK Lele. “Large eddy simulation of compressible turbulent jets.” In: *Center for Turbulence Research, Annual Research Briefs* 365-377 (1999).
- [14] Francesco Bonelli, Annarita Viggiano, and Vinicio Magi. “High-speed turbulent gas jets: an LES investigation of Mach and Reynolds number effects on the velocity decay and spreading rate.” In: *Flow, Turbulence and Combustion* 107.3 (2021), pp. 519–550. DOI: [10.1007/s10494-021-00242-5](https://doi.org/10.1007/s10494-021-00242-5). URL: <https://doi.org/10.1007/s10494-021-00242-5>.
- [15] Can Cai et al. “The Flow Characteristics of Supercritical Carbon Dioxide (SC-CO₂) Jet Fracturing in Limited Perforation Scenarios.” In: *Energies* 13.10 (2020). ISSN: 1996-1073. DOI: [10.3390/en13102627](https://doi.org/10.3390/en13102627). URL: <https://www.mdpi.com/1996-1073/13/10/2627>.
- [16] Wen Chan et al. “Exergoeconomic analysis and optimization of the Allam cycle with liquefied natural gas cold exergy utilization.” In: *Energy Conversion and Management* 235 (2021), p. 113972. ISSN: 0196-8904. DOI: <https://doi.org/10.1016/j.enconman.2021.113972>. URL: <https://www.sciencedirect.com/science/article/pii/S0196890421001485>.
- [17] Bruce Chehroudi, R Cohn, and D Talley. “Cryogenic shear layers: experiments and phenomenological modeling of the initial growth rate under subcritical and supercritical conditions.” In: *International Journal of Heat and Fluid Flow* 23.5 (2002), pp. 554–563.
- [18] T.H. Chung et al. “Generalized multiparameter correlation for nonpolar and polar fluid transport properties.” In: *Ind. Eng. Chem. Res.* 27 (1988), pp. 671–679.
- [19] P. Colella and Paul R. Woodward. “The Piecewise Parabolic Method (PPM) for Gas-Dynamical Simulations.” In: *Journal of Computational Physics* 54 (Sept. 1984), pp. 174–201. DOI: [10.1016/0021-9991\(84\)90143-8](https://doi.org/10.1016/0021-9991(84)90143-8).
- [20] Phillip Colella and Harland M Glaz. “Efficient solution algorithms for the Riemann problem for real gases.” In: *Journal of Computational Physics* 59.2 (1985), pp. 264–289. ISSN: 0021-9991. DOI: [https://doi.org/10.1016/0021-9991\(85\)90146-9](https://doi.org/10.1016/0021-9991(85)90146-9). URL: <https://www.sciencedirect.com/science/article/pii/0021999185901469>.
- [21] Phillip Colella and Michael D. Sekora. “A limiter for PPM that preserves accuracy at smooth extrema.” In: *Journal of Computational Physics* 227.15 (2008), pp. 7069–7076. ISSN: 0021-9991. DOI: <https://doi.org/10.1016/j.jcp.2008.03.034>. URL: <http://www.sciencedirect.com/science/article/pii/S0021999108001435>.

- [22] Francesco Crespi et al. “Supercritical carbon dioxide cycles for power generation: A review.” In: *Applied Energy* 195 (2017), pp. 152–183. ISSN: 0306-2619. DOI: <https://doi.org/10.1016/j.apenergy.2017.02.048>. URL: <http://www.sciencedirect.com/science/article/pii/S0306261917301915>.
- [23] Abdallah Dindi et al. “Policy-driven potential for deploying carbon capture and sequestration in a fossil-rich power sector.” In: *Environmental Science & Technology* 56.14 (2022), pp. 9872–9881.
- [24] Edward Dodge. *Supercritical Carbon Dioxide Power Cycles Starting to Hit the Market*. <https://breakingenergy.com/2014/11/24/supercritical-carbon-dioxide-power-cycles-starting-to-hit-the-market/>. Accessed: 2019-08-08. 2014.
- [25] Emad Dokhaee et al. “Simulation of the Allam cycle with carbon dioxide working fluid and comparison with Brayton cycle.” In: *International Journal of Energy and Environmental Engineering* 12.3 (2021), pp. 543–550. DOI: 10.1007/s40095-021-00401-4. URL: <https://doi.org/10.1007/s40095-021-00401-4>.
- [26] V. Dostal, M.J. Driscoll, and P. Hejzlar. “A Supercritical Carbon Dioxide Cycle for Next Generation Nuclear Reactors.” PhD thesis. MIT, 2004.
- [27] J. G. M. Eggels et al. “Fully developed turbulent pipe flow: a comparison between direct numerical simulation and experiment.” In: *Journal of Fluid Mechanics* 268 (1994), 175?210. DOI: 10.1017/S002211209400131X.
- [28] Alexandre Ern and Vincent Giovangigli. “Fast and Accurate Multicomponent Transport Property Evaluation.” In: *Journal of Computational Physics* 120.1 (1995), pp. 105–116. ISSN: 0021-9991. DOI: <https://doi.org/10.1006/jcph.1995.1151>. URL: <https://www.sciencedirect.com/science/article/pii/S0021999185711515>.
- [29] *Explore, use, make the most of supercritical fluids.* <http://www.supercriticalfluid.org/Supercritical-fluids.146.0.html>. Accessed: 2019-08-08. 2009.
- [30] Robert Eymard, Thierry Gallouët, and Raphaèle Herbin. “Finite volume methods.” In: *Solution of Equation in Rn (Part 3), Techniques of Scientific Computing (Part 3)*. Vol. 7. Handbook of Numerical Analysis. Elsevier, 2000, pp. 713–1018. DOI: [https://doi.org/10.1016/S1570-8659\(00\)07005-8](https://doi.org/10.1016/S1570-8659(00)07005-8). URL: <https://www.sciencedirect.com/science/article/pii/S1570865900070058>.
- [31] Alexandre Favre. “Turbulence: Space?time statistical properties and behavior in supersonic flows.” In: *The Physics of Fluids* 26.10 (Oct. 1983), pp. 2851–2863. ISSN: 0031-9171. DOI: 10.1063/1.864049. eprint: https://pubs.aip.org/aip/pfl/article-pdf/26/10/2851/12495774/2851_1__online.pdf. URL: <https://doi.org/10.1063/1.864049>.

- [32] Dan Fernandes et al. “Process and Carbon Footprint Analyses of the Allam Cycle Power Plant Integrated with an Air Separation Unit.” In: *Clean Technologies* 1.1 (2019), pp. 325–340. ISSN: 2571-8797. DOI: 10.3390/cleantechol1010022. URL: <https://www.mdpi.com/2571-8797/1/1/22>.
- [33] M. Germano. “Turbulence: the filtering approach.” In: *Journal of Fluid Mechanics* 238 (1992), 325?336. DOI: 10.1017/S0022112092001733.
- [34] Mehdi Ghanbari, Mahdi Ahmadi, and Asghar Lashanizadegan. “A comparison between Peng-Robinson and Soave-Redlich-Kwong cubic equations of state from modification perspective.” In: *Cryogenics* 84 (2017), pp. 13–19. ISSN: 0011-2275. DOI: <https://doi.org/10.1016/j.cryogenics.2017.04.001>. URL: <https://www.sciencedirect.com/science/article/pii/S0011227516303538>.
- [35] Trushar B. Gohil, Arun K. Saha, and K. Muralidhar. “Large Eddy Simulation of a Free Circular Jet.” In: *Journal of Fluids Engineering* 136.5 (Mar. 2014). 051205. ISSN: 0098-2202. DOI: 10.1115/1.4026563. eprint: https://asmedigitalcollection.asme.org/fluidsengineering/article-pdf/136/5/051205/6190780/fe_136_05_051205.pdf. URL: <https://doi.org/10.1115/1.4026563>.
- [36] R. P. Gordon. “A supercritical phase separation: The gas-gas equilibrium.” In: *Journal of Chemical Education* 49.4 (1972), p. 249. DOI: 10.1021/ed049p249. eprint: <https://doi.org/10.1021/ed049p249>. URL: <https://doi.org/10.1021/ed049p249>.
- [37] Marc T Henry de Frahan et al. “PeleC: An adaptive mesh refinement solver for compressible reacting flows.” In: *The International Journal of High Performance Computing Applications* 0.0 (2022), p. 10943420221121151. DOI: 10.1177/10943420221121151. URL: <https://doi.org/10.1177/10943420221121151>.
- [38] Man Huang et al. “Analysis of the flow characteristics of the high-pressure supercritical carbon dioxide jet.” In: *Journal of Hyrdroynamics* 31 (2019), pp. 389–399. DOI: <https://doi.org/10.1007/s42241-018-0165-8>. URL: <https://link.springer.com/article/10.1007/s42241-018-0165-8#citeas>.
- [39] Man Huang et al. “Experimental investigation on the flow and rock breaking characteristics of supercritical carbon dioxide jets.” In: *Journal of Petroleum Science and Engineering* 187 (2020), p. 106735. ISSN: 0920-4105. DOI: <https://doi.org/10.1016/j.petrol.2019.106735>. URL: <https://www.sciencedirect.com/science/article/pii/S0920410519311544>.
- [40] Nikolaos D. Katopodes. “Chapter 1 - Basic Concepts.” In: *Free-Surface Flow*. Ed. by Nikolaos D. Katopodes. Butterworth-Heinemann, 2019, pp. 2–98. ISBN: 978-0-12-815489-2. DOI: <https://doi.org/10.1016/B978-0-12-815489-2.00001-0>. URL: <https://www.sciencedirect.com/science/article/pii/B9780128154892000010>.

- [41] Max P. Katz et al. “Preparing Nuclear Astrophysics for Exascale.” In: *SC20: International Conference for High Performance Computing, Networking, Storage and Analysis*. 2020, pp. 1–12. DOI: [10.1109/SC41405.2020.00095](https://doi.org/10.1109/SC41405.2020.00095).
- [42] Robert J Kee, Fran M Rupley, and James A Miller. *Chemkin-II: A Fortran chemical kinetics package for the analysis of gas-phase chemical kinetics*. Tech. rep. Sandia National Lab.(SNL-CA), Livermore, CA (United States), 1989.
- [43] Imane Ghaleb Khalil. “Free-Jet Expansion of Supercritical CO₂.” PhD thesis. University of California, San Diego, 2003.
- [44] Doyle Knight et al. “Compressible large eddy simulation using unstructured grids.” In: *36th AIAA Aerospace Sciences Meeting and Exhibit*. DOI: [10.2514/6.1998-535](https://doi.org/10.2514/6.1998-535). eprint: <https://arc.aiaa.org/doi/pdf/10.2514/6.1998-535>. URL: <https://arc.aiaa.org/doi/abs/10.2514/6.1998-535>.
- [45] A. Kolmogorov. “The Local Structure of Turbulence in Incompressible Viscous Fluid for Very Large Reynolds’ Numbers.” In: *Akademii Nauk SSSR Doklady* 30 (Jan. 1941), pp. 301–305.
- [46] A. N. Kolmogorov. “The Local Structure of Turbulence in Incompressible Viscous Fluid for Very Large Reynolds Numbers.” In: *Proceedings: Mathematical and Physical Sciences* 434.1890 (1991), pp. 9–13. ISSN: 09628444. URL: <http://www.jstor.org/stable/51980> (visited on 07/15/2023).
- [47] Christian Lagarza-Cortés et al. “Large-eddy simulation of transcritical and supercritical jets immersed in a quiescent environment.” In: *Physics of Fluids* 31.2 (Feb. 2019), p. 025104. ISSN: 1070-6631. DOI: [10.1063/1.5054797](https://doi.org/10.1063/1.5054797). eprint: https://pubs.aip.org/aip/pof/article-pdf/doi/10.1063/1.5054797/14935394/025104_1_online.pdf. URL: <https://doi.org/10.1063/1.5054797>.
- [48] A. V. Lazarev and K. A. Tatarenko. “Gas dynamic model of the expansion of a supercritical carbon dioxide pulse jet: A self-similar solution.” In: *Russian Journal of Physical Chemistry B* 10.8 (2016), pp. 1248–1255. DOI: [10.1134/S1990793116080145](https://doi.org/10.1134/S1990793116080145). URL: <https://doi.org/10.1134/S1990793116080145>.
- [49] Eric W. Lemmon, Mark O. McLinden, and Daniel G. Friend. “NIST Chemistry WebBook, NIST Standard Reference Database Number 69.” In: ed. by P.J. Linstrom and W.G. Mallard. Accessed: 2020-03-10. Gaithersburg MD, 20899: National Institute of Standards and Technology, 2018. Chap. Thermophysical Properties of Fluid Systems. DOI: <https://doi.org/10.18434/T4D303>.
- [50] J E Lennard-Jones. “Cohesion.” In: *Proceedings of the Physical Society* 43.5 (Sept. 1931), p. 461. DOI: [10.1088/0959-5309/43/5/301](https://doi.org/10.1088/0959-5309/43/5/301). URL: <https://dx.doi.org/10.1088/0959-5309/43/5/301>.

- [51] Hua-Guang Li, Xi-Yun Lu, and Vigor Yang. “A numerical study of fluid injection and mixing under near-critical conditions.” In: *Acta Mechanica Sinica* 28.3 (June 2012), pp. 559–571. ISSN: 1614-3116. DOI: 10.1007/s10409-012-0035-5. URL: <https://doi.org/10.1007/s10409-012-0035-5>.
- [52] Mukun Li et al. “Comparative simulation research on the stress characteristics of supercritical carbon dioxide jets, nitrogen jets and water jets.” In: *Engineering Applications of Computational Fluid Mechanics* 11.1 (2017), pp. 357–370. DOI: 10.1080/19942060.2017.1293565. eprint: <https://doi.org/10.1080/19942060.2017.1293565>. URL: <https://doi.org/10.1080/19942060.2017.1293565>.
- [53] Mukun Li et al. “Flow energy transformation and dissipation mechanisms of carbon dioxide, nitrogen, and water jets.” In: *Journal of Natural Gas Science and Engineering* 84 (2020), p. 103650. ISSN: 1875-5100. DOI: <https://doi.org/10.1016/j.jngse.2020.103650>. URL: <https://www.sciencedirect.com/science/article/pii/S1875510020305047>.
- [54] Mukun Li et al. “Influences of Supercritical Carbon Dioxide Jets on Damage Mechanisms of Rock.” In: *Arabian Journal for Science and Engineering* 43.5 (May 2018), pp. 2641–2658. ISSN: 2191-4281. DOI: 10.1007/s13369-017-2984-2. URL: <https://doi.org/10.1007/s13369-017-2984-2>.
- [55] *Experimental Investigation in Turbulent Shear Mixing Layer at Supercritical Condition*. Vol. Volume 2: Multiphase Flow (MFTC); Computational Fluid Dynamics (CFDTC); Micro and Nano Fluid Dynamics (MNFDTC). Fluids Engineering Division Summer Meeting. V002T04A010. Aug. 2022. DOI: 10.1115/FEDSM2022-87029. eprint: <https://asmedigitalcollection.asme.org/FEDSM/proceedings-pdf/FEDSM2022/85840/V002T04A010/6923087/v002t04a010-fedsm2022-87029.pdf>. URL: <https://doi.org/10.1115/FEDSM2022-87029>.
- [56] Rebecca Lindsey. *Climate change: Atmospheric carbon dioxide*. May 2023. URL: <https://www.climate.gov/news-features/understanding-climate/climate-change-atmospheric-carbon-dioxide#:~:text=Without%5C%20carbon%5C%20dioxide%5C%2C%5C%20Earth%5C%27s%5C%20natural,causing%5C%20global%5C%20temperature%5C%20to%5C%20rise..>
- [57] Yong Liu et al. “Application of supercritical carbon dioxide jet: A parametric study using numerical simulation model.” In: *Journal of Petroleum Science and Engineering* 201 (2021), p. 108422. ISSN: 0920-4105. DOI: <https://doi.org/10.1016/j.petrol.2021.108422>. URL: <https://www.sciencedirect.com/science/article/pii/S0920410521000814>.
- [58] Q Lv et al. “Numerical investigation on the expansion of supercritical carbon dioxide jet.” In: *IOP Conference Series: Materials Science and Engineering* 52.7 (Dec. 2013), p. 072011. DOI: 10.1088/1757-899x/52/7/072011. URL: <https://doi.org/10.1088%5C%2F1757-899x%5C%2F52%5C%2F7%5C%2F072011>.
- [59] M. Martín, Ugo Piomelli, and Graham Candler. “Subgrid-Scale Models for Compressible Large-Eddy Simulations.” In: *Theoretical and Computational Fluid Dynamics* 13 (Feb. 2000), pp. 361–376.

- [60] W Mayer et al. “Raman measurements of cryogenic injection at supercritical pressure.” In: *Heat and Mass Transfer* 39.8-9 (2003), pp. 709–719.
- [61] Bonnie McBride, Michael Zehe, and Sanford Gordon. “NASA Glenn coefficients for calculating thermodynamic properties of individual species.” In: (Oct. 2002). URL: <https://ntrs.nasa.gov/api/citations/20020085330/downloads/20020085330.pdf>.
- [62] G.H. Miller and P. Colella. “A Conservative Three-Dimensional Eulerian Method for Coupled Solid-Fluid Shock Capturing.” In: *Journal of Computational Physics* 183.1 (2002), pp. 26–82. ISSN: 0021-9991. DOI: <https://doi.org/10.1006/jcph.2002.7158>. URL: <http://www.sciencedirect.com/science/article/pii/S0021999102971585>.
- [63] Emmanuel Motheau and John Wakefield. “Investigation of finite-volume methods to capture shocks and turbulence spectra in compressible flows.” In: *Communications in Applied Mathematics and Computational Science* 15.1 (2020), pp. 1–36. DOI: [10.2140/camcos.2020.15.1](https://doi.org/10.2140/camcos.2020.15.1). URL: <https://doi.org/10.2140/camcos.2020.15.1>.
- [64] Hagen Müller et al. “Large-eddy simulation of nitrogen injection at trans- and supercritical conditions.” In: *Physics of Fluids* 28.1 (2016), p. 015102. DOI: [10.1063/1.4937948](https://doi.org/10.1063/1.4937948). eprint: <https://doi.org/10.1063/1.4937948>. URL: <https://doi.org/10.1063/1.4937948>.
- [65] Andrew Nonaka, Marcus S. Day, and John B. Bell. “A conservative, thermodynamically consistent numerical approach for low Mach number combustion. Part I: Single-level integration.” In: *Combustion Theory and Modelling* 22.1 (2018), pp. 156–184. DOI: [10.1080/13647830.2017.1390610](https://doi.org/10.1080/13647830.2017.1390610). eprint: <https://doi.org/10.1080/13647830.2017.1390610>. URL: <https://doi.org/10.1080/13647830.2017.1390610>.
- [66] A. Nonaka et al. “A deferred correction coupling strategy for low Mach number flow with complex chemistry.” In: *Combustion Theory and Modelling* 16.6 (2012), pp. 1053–1088. DOI: [10.1080/13647830.2012.701019](https://doi.org/10.1080/13647830.2012.701019). eprint: <https://doi.org/10.1080/13647830.2012.701019>. URL: <https://doi.org/10.1080/13647830.2012.701019>.
- [67] Syed Mohammad Ovais. “Direct Numerical Simulation of supercritical CO₂ mixing and combustion.” PhD thesis. Clemson University, 2022. URL: https://tigerprints.clemson.edu/all_dissertations/3073.
- [68] *Overview of Greenhouse Gases*. Apr. 2023. URL: <https://www.epa.gov/ghgemissions/overview-greenhouse-gases>.
- [69] Robert Paine et al. “1 - Mechanical engineering principles.” In: *Mechanical Engineer’s Reference Book (Twelfth Edition)*. Ed. by Edward H. Smith. Twelfth Edition. Butterworth-Heinemann, 1994, pp. 1-1-1-48. ISBN: 978-0-7506-1195-4. DOI: <https://doi.org/10.1016/B978-0-7506-1195-4.50005-1>. URL: <http://www.sciencedirect.com/science/article/pii/B9780750611954500051>.
- [70] *PeleC - PeleC 0.1 documentation*. <https://amrex-combustion.github.io/PeleC/>.

- [71] Michael Persichilli et al. “Supercritical CO₂ Power Cycle Developments and Commercialization: Why sCO₂ can Displace Steam.” In: *Power-Gen India & Central Asia*. 2012.
- [72] X. Petit et al. “Large-eddy simulation of supercritical fluid injection.” In: *The Journal of Supercritical Fluids* 84 (2013), pp. 61–73. ISSN: 0896-8446. DOI: <https://doi.org/10.1016/j.supflu.2013.09.011>. URL: <http://www.sciencedirect.com/science/article/pii/S0896844613003239>.
- [73] Ugo Piomelli. “Chapter Three - Large-eddy simulations.” In: *Advanced Approaches in Turbulence*. Ed. by Paul Durbin. Elsevier, 2021, pp. 83–131. ISBN: 978-0-12-820774-1. DOI: <https://doi.org/10.1016/B978-0-12-820774-1.00009-4>. URL: <https://www.sciencedirect.com/science/article/pii/B9780128207741000094>.
- [74] T J Poinsot and SK Lele. “Boundary conditions for direct simulations of compressible viscous flows.” In: *Journal of computational physics* 101.1 (1992), pp. 104–129.
- [75] Bruce E Poling, John M Prausnitz, and John P O’Connell. *Properties of gases and liquids*. McGraw-Hill Education, 2001.
- [76] Stephen B. Pope. *Turbulent Flows*. Cambridge: Cambridge University Press, 2000.
- [77] Karsten Pruess. *Enhanced Geothermal Systems (EGS) comparing water with CO₂ as heat transmission fluids*. Tech. rep. Lawrence Berkeley National Laboratory, 2007.
- [78] Karsten Pruess and Mohamed Azaroual. “ON THE FEASIBILITY OF USING SUPERCRITICAL CO₂ AS HEAT TRANSMISSION FLUID IN AN ENGINEERED HOT DRY ROCK GEOTHERMAL SYSTEM.” In: *Thirty-First Workshop on Geothermal Reservoir Engineering*. 2006.
- [79] Senthil Kumar Raman et al. “Flow Characteristics of Confined G-CO₂ and S-CO₂ Jets.” In: *Recent Asian Research on Thermal and Fluid Sciences: Proceedings of AJWTF7 2018*. Ed. by Abhilash Suryan et al. Springer Nature Singapore Pte Ltd., 2020, pp. 281–295. ISBN: 123. DOI: <https://doi.org/10.1007/978-981-15-1892-8\23>. URL: www.sciencedirect.com/science/article/pii/S0896844620303922.
- [80] Elizabeth Rasmussen, Shashank Yellapantula, and Michael James Martin. “How equation of state selection impacts accuracy near the critical point: Forced convection supercritical CO₂ flow over a cylinder.” In: *The Journal of Supercritical Fluids* 171 (2021), p. 105141. ISSN: 0896-8446. DOI: <https://doi.org/10.1016/j.supflu.2020.105141>. URL: <http://www.sciencedirect.com/science/article/pii/S0896844620303922>.
- [81] Florian Ries and Amsini Sadiki. “Supercritical and transcritical turbulent injection processes: Consistency of numerical modeling.” In: *Atomization and Sprays* 31.5 (2021).
- [82] Florian Ries et al. “Numerical analysis of turbulent flow dynamics and heat transport in a round jet at supercritical conditions.” In: *International Journal of Heat and Fluid Flow* 66 (Aug. 2017), pp. 172–184. DOI: [10.1016/j.ijheatfluidflow.2017.06.007](https://doi.org/10.1016/j.ijheatfluidflow.2017.06.007).

- [83] 8 Rivers. *THE ALLAM-FETVEDT CYCLE*. 2023. URL: <https://8rivers.com/portfolio/the-allam-fetvedt-cycle-and-net-power/>.
- [84] Philip JW Roberts and Donald R Webster. *Turbulent diffusion*. 2002.
- [85] Anthony Ruiz et al. “Numerical Benchmark for High-Reynolds-Number Supercritical Flows with Large Density Gradients.” In: *AIAA Journal* 54 (Nov. 2015), pp. 1445–1460. ISSN: 0001-1452.
- [86] P. Sagaut and R. Grohens. “Discrete filters for large eddy simulation.” In: *International Journal for Numerical Methods in Fluids* 31.8 (1999), pp. 1195–1220. DOI: 10.1002/(SICI) 1097-0363(19991230)31:8<1195::AID-FLD914>3.0.CO;2-H.
- [87] Thomas Schmitt et al. “Large-Eddy Simulation of Supercritical-Pressure Round Jets.” In: *AIAA Journal* 48.9 (2010), pp. 2133–2144. DOI: 10.2514/1.J050288. eprint: <https://doi.org/10.2514/1.J050288>. URL: <https://doi.org/10.2514/1.J050288>.
- [88] Uttiya Sengupta. “Fully compressible Direct Numerical Simulations of carbon dioxide close to the vapour- liquid critical point.” PhD thesis. Delft University of Technology, 2019. DOI: 10.4233/uuid:513e5fa7-aef5-47e8-a7f9-d99a06c8981d. URL: <https://pure.tudelft.nl/ws/portalfiles/portal/51831002/Thesis.pdf>.
- [89] Huaizhong Shi et al. “Design of experimental setup for supercritical CO₂ jet under high ambient pressure conditions.” In: *Review of Scientific Instruments* 87.12 (2016), p. 125115. DOI: 10.1063/1.4972885. eprint: <https://doi.org/10.1063/1.4972885>. URL: <https://doi.org/10.1063/1.4972885>.
- [90] Hariswaran Sitaraman et al. “Adaptive mesh based combustion simulations of direct fuel injection effects in a supersonic cavity flame-holder.” In: *Combustion and Flame* 232 (2021), p. 111531. ISSN: 0010-2180. DOI: <https://doi.org/10.1016/j.combustflame.2021.111531>. URL: <https://www.sciencedirect.com/science/article/pii/S0010218021002741>.
- [91] Giorgio Soave. “Equilibrium constants from a modified Redlich-Kwong equation of state.” In: *Chemical Engineering Science* 27.6 (1972), pp. 1197–1203. ISSN: 0009-2509. DOI: [https://doi.org/10.1016/0009-2509\(72\)80096-4](https://doi.org/10.1016/0009-2509(72)80096-4). URL: <http://www.sciencedirect.com/science/article/pii/0009250972800964>.
- [92] “Supercritical fluid.” In: *Chemical Business* 28.6 (2014), pp. 39–44. ISSN: 09703136. URL: <https://login.proxy.lib.fsu.edu/login?url=http://search.ebscohost.com/login.aspx?direct=true&db=f5h&AN=97302089&site=eds-live&scope=site>.
- [93] Robert Tarjan. “Depth-first search and linear graph algorithms.” In: *SIAM journal on computing* 1.2 (1972), pp. 146–160.

- [94] Bram van Leer. “Towards the ultimate conservative difference scheme. V. A second-order sequel to Godunov’s method.” In: *Journal of Computational Physics* 32.1 (1979), pp. 101–136. ISSN: 0021-9991. DOI: [https://doi.org/10.1016/0021-9991\(79\)90145-1](https://doi.org/10.1016/0021-9991(79)90145-1). URL: <https://www.sciencedirect.com/science/article/pii/0021999179901451>.
- [95] J. D. van der Waals. “on the continuity of the gaseous and liquid states.” PhD thesis. University of Leiden, 1873.
- [96] Cailin Wang et al. “Experimental study on dispersion behavior during the leakage of high pressure CO₂ pipelines.” In: *Experimental Thermal and Fluid Science* 105 (2019), pp. 77–84. ISSN: 0894-1777. DOI: <https://doi.org/10.1016/j.expthermflusci.2019.03.014>. URL: <http://www.sciencedirect.com/science/article/pii/S0894177719300974>.
- [97] Hai-zhu WANG et al. “Flow field simulation of supercritical carbon dioxide jet: Comparison and sensitivity analysis.” In: *Journal of Hydrodynamics, Ser. B* 27.2 (2015), pp. 210–215. ISSN: 1001-6058. DOI: [https://doi.org/10.1016/S1001-6058\(15\)60474-7](https://doi.org/10.1016/S1001-6058(15)60474-7). URL: <http://www.sciencedirect.com/science/article/pii/S1001605815604747>.
- [98] Song Wang et al. “New Conceptual Design of an Integrated Allam-Cycle Power Complex Coupling Air Separation Unit and Ammonia Plant.” In: *Industrial & Engineering Chemistry Research* 60.49 (2021), pp. 18007–18017. DOI: 10.1021/acs.iecr.1c02478. eprint: <https://doi.org/10.1021/acs.iecr.1c02478>. URL: <https://doi.org/10.1021/acs.iecr.1c02478>.
- [99] C. Taber Wanstall, Joshua A. Bittle, and Ajay K. Agrawal. “Transient mixing behavior of a supercritical fluid injected into supercritical and subcritical environments.” In: *Physics of Fluids* 34.2 (Feb. 2022), p. 023104. ISSN: 1070-6631. DOI: 10.1063/5.0072291. eprint: https://pubs.aip.org/aip/pof/article-pdf/doi/10.1063/5.0072291/16638858/023104_1_online.pdf. URL: <https://doi.org/10.1063/5.0072291>.
- [100] Wu Wei, Maozhao Xie, and Ming Jia. “Large eddy simulation of fluid injection under trans-critical and supercritical conditions.” In: *Numerical Heat Transfer, Part A: Applications* 70.8 (2016), pp. 870–886. DOI: 10.1080/10407782.2016.1214485. eprint: <https://doi.org/10.1080/10407782.2016.1214485>. URL: <https://doi.org/10.1080/10407782.2016.1214485>.
- [101] Gina L Weibel and Christopher K Ober. “An overview of supercritical CO₂ applications in microelectronics processing.” In: *Microelectronic Engineering* 65.1-2 (2003), pp. 145–152.
- [102] N.T. Weiland et al. “12 - Fossil energy.” In: *Fundamentals and Applications of Supercritical Carbon Dioxide (sCO₂) Based Power Cycles*. Ed. by Klaus Brun, Peter Friedman, and Richard Dennis. Woodhead Publishing, 2017, pp. 293–338. ISBN: 978-0-08-100804-1. DOI: <https://doi.org/10.1016/B978-0-08-100804-1.00012-8>. URL: <https://www.sciencedirect.com/science/article/pii/B9780081008041000128>.

- [103] Martin T. White et al. “Review of supercritical CO₂ technologies and systems for power generation.” In: *Applied Thermal Engineering* 185 (2021), p. 116447. ISSN: 1359-4311. DOI: <https://doi.org/10.1016/j.applthermaleng.2020.116447>. URL: <https://www.sciencedirect.com/science/article/pii/S1359431120339235>.
- [104] Sujeet Yadav and SS Mondal. “A review on the progress and prospects of oxy-fuel carbon capture and sequestration (CCS) technology.” In: *Fuel* 308 (2022), p. 122057.
- [105] Yulong Yang et al. “Study on the Impact Pressure of Swirling-Round Supercritical CO₂ Jet Flow and Its Influencing Factors.” In: *Energies* 14.1 (2021). ISSN: 1996-1073. DOI: 10.3390/en14010106. URL: <https://www.mdpi.com/1996-1073/14/1/106>.
- [106] Jung Yul Yoo. “The Turbulent Flows of Supercritical Fluids with Heat Transfer.” In: *Annual Review of Fluid Mechanics* 45.1 (2013), pp. 495–525. DOI: 10.1146/annurev-fluid-120710-101234. eprint: <https://doi.org/10.1146/annurev-fluid-120710-101234>. URL: <https://doi.org/10.1146/annurev-fluid-120710-101234>.
- [107] Han Zhang et al. “Large eddy simulations of the all-speed turbulent jet flow using 3-D CFD code GASFLOW-MPI.” In: *Nuclear Engineering and Design* 328 (2018), pp. 134–144. ISSN: 0029-5493. DOI: <https://doi.org/10.1016/j.nucengdes.2017.12.032>. URL: <https://www.sciencedirect.com/science/article/pii/S0029549317306234>.
- [108] Hongyuan Zhang, Ping Yi, and Suo Yang. “Multicomponent Effects on the Supercritical CO₂ Systems: Mixture Critical Point and Phase Separation.” In: *Flow, Turbulence and Combustion* 109 (2022), pp. 515–543. DOI: <https://doi.org/10.1007/s10494-022-00335-9>. URL: <https://link.springer.com/article/10.1007/s10494-022-00335-9#citeas>.
- [109] Huidong Zhang et al. “Investigation on the fluctuation characteristics and its influence on impact force of supercritical carbon dioxide jet.” In: *Energy* 253 (2022), p. 124125. ISSN: 0360-5442. DOI: <https://doi.org/10.1016/j.energy.2022.124125>. URL: <https://www.sciencedirect.com/science/article/pii/S0360544222010283>.
- [110] Weiqun Zhang et al. “AMReX: a framework for block-structured adaptive mesh refinement.” In: *Journal of Open Source Software* 4.37 (2019), p. 1370. DOI: 10.21105/joss.01370. URL: <https://doi.org/10.21105/joss.01370>.
- [111] Weiqun Zhang et al. “AMReX: Block-structured adaptive mesh refinement for multiphysics applications.” In: *The International Journal of High Performance Computing Applications* 35.6 (2021), pp. 508–526. DOI: 10.1177/10943420211022811. eprint: <https://doi.org/10.1177/10943420211022811>. URL: <https://doi.org/10.1177/10943420211022811>.
- [112] Nan Zong and Vigor Yang*. “CRYOGENIC FLUID JETS AND MIXING LAYERS IN TRANSCRITICAL AND SUPERCRITICAL ENVIRONMENTS.” In: *Combustion Science and Technology* 178.1-3 (2006), pp. 193–227. DOI: 10.1080/00102200500287613. eprint: <https://doi.org/10.1080/00102200500287613>. URL: <https://doi.org/10.1080/00102200500287613>.

- [113] Nan Zong et al. “A numerical study of cryogenic fluid injection and mixing under supercritical conditions.” In: *Physics of Fluids* 16.12 (2004), pp. 4248–4261. DOI: 10.1063/1.1795011. eprint: <https://doi.org/10.1063/1.1795011>. URL: <https://doi.org/10.1063/1.1795011>.

BIOGRAPHICAL SKETCH

Julia Ream was born and raised in Sarasota, FL. From an early age, Julia found math to be “fun”, but didn’t come to realize how uncommon that sentiment was until much later on in life. She started her undergraduate career at Florida State University in 2013, enrolling as an Exploratory student before committing to the Humanities and later on Theatre. Upon realizing that she missed doing math (weird), she added Applied Mathematics to her roster of majors. Although it took nearly 21 years, Julia eventually realized that she actually really liked math. So, after completing a Bachelor of Arts in Humanities and a Bachelor of Science in Mathematics, she decided to pursue her Doctoral degree in Applied and Computational Mathematics, also at Florida State University.